A Wireless Lab-in-a-Pill Biosensor for Rapid Detection of Gastrointestinal Bleeding

A dissertation presented

by

Alex Nemiroski

to

School of Engineering and Applied Sciences

in partial fulfillment of the requirements
for the degree of
Doctor of Philosophy
in the subject of
Applied Physics

Harvard University
Cambridge, Massachusetts

May 2011

Thesis advisor | Author

Robert M. Westervelt | **Alex Nemiroski**

A Wireless Lab-in-a-Pill Biosensor for Rapid Detection of Gastrointestinal Bleeding

Abstract

We have developed a miniaturized fluoresence sensor integrated into a lab-in-a-pill platform based on the commericial IEEE 802.15.4 Zigbee wireless protocol operating at 2.4 GHz. The device takes the form of a swallowable capsule that can detect the fluorescent tracer dye fluorescein in blood, and is intended to be used in the Gastrointestinal (GI) tract to detect internal bleeding from an ulcer. Low noise detection electronics and on-chip digital filtering allow for sub-micromolar sensitivity despite small sample volume and lack of focusing optics. A power saving algorithm enhances device longevity inside the body. Data is streamed in real-time to a Zigbee enabled external monitoring device. In this thesis we report the construction of this device along with bench-top experiments evaluating the sensitivity of the fluoresence sensor as a method to detect internal bleeding.

Contents

Title Page i
Abstract iii
Table of Contents iv

1 Introduction 2
1.1 Motivation 2
 1.1.1 Medical 2
 1.1.2 Technological 3
1.2 The Detection of GI Bleeding 4
 1.2.1 Quantifying Blood Loss 4
 1.2.2 Prior Work 6
1.3 A New Method to Identify Active GI Bleeding 7
1.4 Design Specifications 9
1.5 Realizing this Goal 10
1.6 Thesis Outline 11

2 Detecting Gastrointestinal Bleeding with a Fluorescent Tracer 12
2.1 Introduction 12
2.2 Pharmacokinetics of an Intravenous Tracer 13
2.3 Blood Tracer Concentration as an Indicator of Acute GI Bleeding . . 14
 2.3.1 Overview 14
 2.3.2 Modeling GI bleeding 15
2.4 Detecting the Concentration of a Tracer 19
 2.4.1 Overview 19
 2.4.2 Fluorometry 19
 2.4.3 Optical Filters and Pinholes 20
 2.4.4 Ultra-Compact Geometry 23
 2.4.5 Fluorometer Model 25
2.5 Relating the Fluorescence to Concentration 27
 2.5.1 Excitation Path 27
 2.5.2 Emission Path 28

- 2.5.3 Full Optical Path . . . 30
- 2.6 Conclusion . . . 31

3 Detection Electronics and Signal Processing 32

- 3.1 Introduction . . . 32
- 3.2 Silicon Photodiodes . . . 33
  - 3.2.1 Overview . . . 33
  - 3.2.2 Photodiode Physics . . . 33
  - 3.2.3 Photodiode Circuit Model . . . 36
- 3.3 Noise . . . 37
  - 3.3.1 Overview . . . 37
  - 3.3.2 General White Noise . . . 38
  - 3.3.3 Sources of White Noise . . . 39
  - 3.3.4 Noise in a circuit with gain . . . 41
  - 3.3.5 Choosing a photodiode operating mode . . . 43
- 3.4 Current-to-Voltage Conversion . . . 45
  - 3.4.1 Overview . . . 45
  - 3.4.2 Methods of I-to-V Conversion . . . 45
  - 3.4.3 Modeling the TIA Transfer Function . . . 47
  - 3.4.4 TIA transfer function . . . 50
  - 3.4.5 TIA noise . . . 53
- 3.5 Data acquisition and digital filtering . . . 54
  - 3.5.1 Overview . . . 54
  - 3.5.2 Noise . . . 55
  - 3.5.3 Filtering 1/f Noise . . . 58
- 3.6 Input Referred Noise: The Detection Limit . . . 59
- 3.7 Conclusion . . . 60

4 The Lab-in-a-Pill Hardware Platform 61

- 4.1 Introduction . . . 61
- 4.2 Body Sensor Networking . . . 62
  - 4.2.1 Overview . . . 62
  - 4.2.2 Wireless Networking . . . 64
  - 4.2.3 IEEE 802.15.4 Overview . . . 67
  - 4.2.4 Wireless Link Budget . . . 69
  - 4.2.5 *In Vivo* Telemetry . . . 72
- 4.3 Software . . . 75
- 4.4 Power Consumption . . . 79
  - 4.4.1 Overview . . . 79
  - 4.4.2 Sources of Current Consumption . . . 80
  - 4.4.3 Total Current Consumption and Battery Lifetime . . . 81
  - 4.4.4 Stages of Charge Consumption . . . 81

4.4.5 Data Transmission . . . 83
4.4.6 Network Poll . . . 84
4.4.7 Total Current Consumption . . . 85
4.5 Conclusion . . . 86

5 Design of a Miniature Fluorometer for Bleeding Detection 87
5.1 Introduction . . . 87
5.2 Choice of Fluorescent Tracer . . . 88
5.3 Detecting Acute GI Bleeding . . . 90
5.3.1 Quantifying the Bleeding Detection Threshold . . . 90
5.3.2 Detecting Blood Volume by Measuring the Concentration of Fluorescein . . . 92
5.4 Fluorometer Design . . . 94
5.4.1 Overview . . . 94
5.4.2 Choice of Optical Components . . . 94
5.4.3 Optical Geometry . . . 98
5.4.4 Detection Optical Intensity . . . 100
5.5 Measurement Electronics . . . 102
5.5.1 Overview . . . 102
5.5.2 Electronic Component Constraints . . . 102
5.5.3 Detector Component Selection . . . 103
5.5.4 Measurement . . . 105
5.6 The Limit of Detection . . . 109
5.7 Conclusion . . . 110

6 Design: Hardware Platform and Packaging of a Capsular Biosensor 111
6.1 Introduction . . . 111
6.1.1 Choice of Microcontroller . . . 112
6.2 Hardware Platform Overview . . . 113
6.3 LED Pulsing Circuit . . . 115
6.4 Radio Frequency Communication . . . 116
6.5 Power . . . 119
6.5.1 Battery . . . 119
6.5.2 Voltage Regulators . . . 121
6.5.3 Current Consumption . . . 123
6.6 Printed Circuit Board Design . . . 128
6.7 Packaging . . . 134
6.8 Conclusion . . . 135

7 Construction of the Lab-in-a-Pill Biosensor 136
7.1 Introduction . . . 136
7.2 Fluorometer: Fabrication and Assembly . . . 137

7.2.1 Optical Filter Fabrication 137
7.2.2 Optical Housing Fabrication 140
7.2.3 Fluorometer Assembly 142
7.3 Electronics Fabrication and Programming 146
7.3.1 Overview 146
7.3.2 Printed Circuit Board Pre-Cut 148
7.3.3 Surface Mount Assembly 149
7.3.4 Device Programming 151
7.3.5 Finish Cut 152
7.4 Final Assembly and Packaging 154
7.4.1 Overview 154
7.4.2 Attaching the Fluorometer and Battery 155
7.4.3 Device Shielding 157
7.4.4 Capsular Packaging 157
7.5 Conclusion 160

8 Experimental: Fluorometer and Capsular Biosensor Performance 161
8.1 Introduction 161
8.2 Characterizing Fluorometer Optics 162
8.2.1 Measurement Set-up 162
8.2.2 Fluorometer Spectral Data 167
8.2.3 Angular Transmission 169
8.3 Characterizing Fluorometer Electronic Noise 171
8.3.1 Measurement Wireless Networking 171
8.3.2 Measurement Set-Up 172
8.3.3 Noise Measurement 173
8.4 Fluorometer Sensitivity and Blood Detection 178
8.4.1 Measurement Set-Up 178
8.4.2 Fluorometer Sensitivity 180
8.4.3 Limit of Detection 181
8.4.4 Detection of Blood 182
8.5 Discussion and Conclusion 184

9 Conclusion 185
9.1 Thesis Summary 185
9.2 Comparison with Initial Specification 186
9.3 Future Outlook 186

Bibliography 188

A Device Bill of Materials 193

Chapter 1

Introduction

1.1 Motivation

1.1.1 Medical

Gastrointestinal (GI) bleeding remains problematic for the 300,000 patients who are hospitalized yearly in the United States with upper GI bleeding (UGIB), for which all-cause mortality ranges from 5% to 19% [1][2] . The most common causes include peptic ulcer disease, esophageal varices, and erosive conditions (gastritis, esophagitis, duodenitis) [3][4][5]. After endoscopic therapy of non-variceal upper GI hemorrhage, the rate of in-hospital re-bleeding has been published to be as high as 32% in a single-center study [2]. However, re-bleeding rates are typically thought to be in the 10%-16% range [5][6][7][8]. After treatment of an acute variceal hemorrhage, re-bleeding within 5 days occurs in up to 15% [9]. Several studies have shown that both variceal and non-variceal re-bleeding, and in particular in-hospital re-bleeding, to be strong predictors of in-hospital mortality and overall mortality[10][11].

Current clinical options for detection of re-bleeding include vital signs monitoring, serial hematocrit/hemoglobin checks, and observation of clinical status (e.g. melena, hematemesis)[12]. However, these methods can be imprecise and often require clinical interpretation[13][14]. Furthermore, these methods usually do not indicate a re-bleeding event in real time and sometimes call attention to a re-bleeding event after significant blood loss has occurred[15]. A new method to detect GI bleeding, in real-time, would radically improve the treatment options for UGIB patients.

We address this medical problem by using the latest developments in electronic miniaturization to design and build a wireless lab-in-a-pill biosensor to detect GI bleeding in real-time.

1.1.2 Technological

In vivo wireless biosensors were first used for wireless pH monitoring in the 1990s although the ultimate impact of these devices on the medical community has only been marginal [16]. Because prior electronics, radio, and energy storage technologies were relatively inefficient, existing wireless biosensors tend to be large devices with simple communications capabilities and are not generally preferred over traditional medical equipment. Advances in microelectronics and telecommunications over the past two decades have ushered in an era of small, self-contained electronic devices with the capability for sensing, computing, and wireless communication [17]. The market-driven need for increased complexity, functionality, and interoperability, as well as the decreased size and cost of wireless devices, has recently led to a series of technological developments aimed at creating entire systems contained in a few, or even a single CMOS chip [18]. This theme of convergence has created miniature devices with the functionality needed to create a new breed of wireless biosensors with the small size, intelligence, and autonomy needed for practical medical applications. Advances in electronics have recently led to wearable, implantable, and ingestible sensor devices that are commercially available [18],[17]. The technology presents one opportunity to begin providing a realistic alternative to traditional medical procedures that can be relatively costly, invasive, uncomfortable, and time-consuming. By simplifying the procedures for monitoring, diagnostics, and testing, while providing continuous access to patient data, these biosensor devices stand to revolutionize the medical industry in the near future.

1.2 The Detection of GI Bleeding

1.2.1 Quantifying Blood Loss

Hemorrhaging - the loss of blood volume from the circulatory system, and colloquially known as bleeding - can lead to to a variety of physical symptoms, and can be fatal in cases of excessive blood loss. The severity of hemorrhaging is commonly divided into four distinct stages according to symptoms [19]:

- Stage I: the loss of $< 15\%$ of total circulating blood volume. No significant symptoms or change in vital signs.
- Stage II-III: the loss of $15-40\%$ of total circulating blood volume. Vital signs such as blood pressure and heart rate are impacted.

- Stage IV: the loss of $> 40\%$ of circulating blood volume. This amount of blood loss is referred to as exsanguination and is usually fatal.

GI bleeding is one of the major types of internal hemorrhaging. In this section we discuss GI bleeding, review the current methods of diagnosis, and motivate a new method for early detection of active GI bleeding.

If the rate of active GI bleeding becomes profuse, a patient can progress from a stage I to a stage IV bleed within a few hours, which is quite a short window of time to both observe symptoms and administer treatment. Therefore, it is advantageous to diagnose GI bleeding as early as possible. Typically, evidence of blood in the vomit or stool can be found in cases of stage I GI bleeding, however these symptoms can have a large latency, manifesting hours after the onset of the bleed[12][13][14]. Waiting for blood to appear in a patient's vomit or stool can take away precious time in cases of profuse bleeding [15]. When GI bleeding reaches stage II-III, there are distinct physiological symptoms such as tachycardia, nausea, blood pressure drop, and skin paleness [19]. However, observation of these symptoms already indicates significant blood loss, which does not constitute early detection. To uniquely diagnose early active GI bleeding, it is typically necessary to employ more sophisticated techniques.

An ideal early detection method would be uniquely sensitive to stage I active GI bleeding, and be able to monitor for future bleeding over the course of many hours or days. This means that the method needs to differentiate between active and past GI bleeding, detect blood loss with minimal latency and high sensitivity, and be able to monitor continuously for the aforementioned period of time.

1.2.2 Prior Work

Currently, there are a number of technologies and methods that can accurately diagnose early stage active GI bleeding such as such as traditional endoscopy [R], capsular endoscopy [20], angiography [21], and radionuclide scanning[1]. Each method has a its strengths and weaknesses, for example:

- Traditional endoscopy can detect minor GI bleeding and can differentiate between past and active GI bleeding, but cannot be used monitor continuously over a long time period.
- Capsular endoscopy can monitor over a long time period, and can detect blood in the stomach. However, this method cannot be used to reliably differentiate past and active GI bleeding since evidence of blood in the stomach is not necessarily an indicator of active GI bleeding.
- Angiography and radio-labeling are extremely accurate[2]. However, monitoring continuously over a period of hours or days would be extremely cost prohibitive.

Furthermore, Schostek et al. [22] have developed an telemetric implantable sensor for the GI tract capable of detecting hemoglobin through a spectroscopic method, however this too suffers from the inability to differentiate between past and active GI bleeding. Looking beyond the field of medicine to forensic criminology, there are

---

[1] Radionuclide scanning to detect GI bleeding involves whole body imaging of red blood cells labeled with technicium-99 [21]. Once the tagged cells are naturally filtered out of the blood stream, CT or MRI is used to detect pooling of the blood in the GI tract.

[2] Angiography and radionuclide scanning can detect blood loss rates > 0.1 mL/min and > 0.01 mL/min respectively [21]. For comparison, a maximal stage I blood loss over 24 hours (15% of total blood volume ≈ 5 liters), is rate of ≈ 0.5 mL/min, and can be easily detected by these two high sensitivity methods.

a range of chemicals that are used to detect traces of blood such as Benzidine and Luminol, which react with the peroxidase enzymes in blood to produce a detectable color change, or enable the blood to fluoresce under UV excitation [23]. These methods, even if somehow modified to operate inside the GI tract, still would lack in their ability to differentiate between past and active GI bleeding.

To our knowledge, there are no technologies currently capable of reliably and accurately identifying an early active GI bleed as uniquely different from a past GI bleed, or monitoring for a future GI bleed over the course of hours to days. This presents a unique opportunity for innovation.

1.3 A New Method to Identify Active GI Bleeding

We solve the problem of differentiating past vs. active GI bleeding by introducing a fluorescent blood tracer as a contrast agent into the cardiovascular system through an intravenous injection. If the patient suffers from an active GI bleed, and only in that case, the tracer dye will enter the GI tract. The tracer is chosen to have a unique fluorescence signature which provides high contrast between blood from the active GI bleed with the tracer and a past GI bleed without the tracer, and hence a high detection specificity for active GI bleeding. This motivates our choice of fluorometery as the sensor modality for the capsular blood detector.

The fluorometer is integrated into a lab-in-a-pill platform based on the commericial IEEE 802.15.4 Zigbee wireless protocol operating at 2.4 GHz [24]. The device takes the form of a swallowable capsule that can detect a fluorescent tracer dye *in vivo* in the GI tract indicating internal bleeding from an ulcer. Low noise detection electronics and on-chip digital filtering allow for sub-micromolar sensitivity despite small sample volume and lack of focusing optics. A power saving algorithm enhances device longevity inside the body.

Once the capsular biosensor has aquired data, it transmits that data out of the body to an external monitoring device that is mounted immediately outside the body. Once the data has been received by the external monitor through this body sensor network, it can be routed through the patients mobile phone to the hospital local area network and received by appropriate medical personnel.

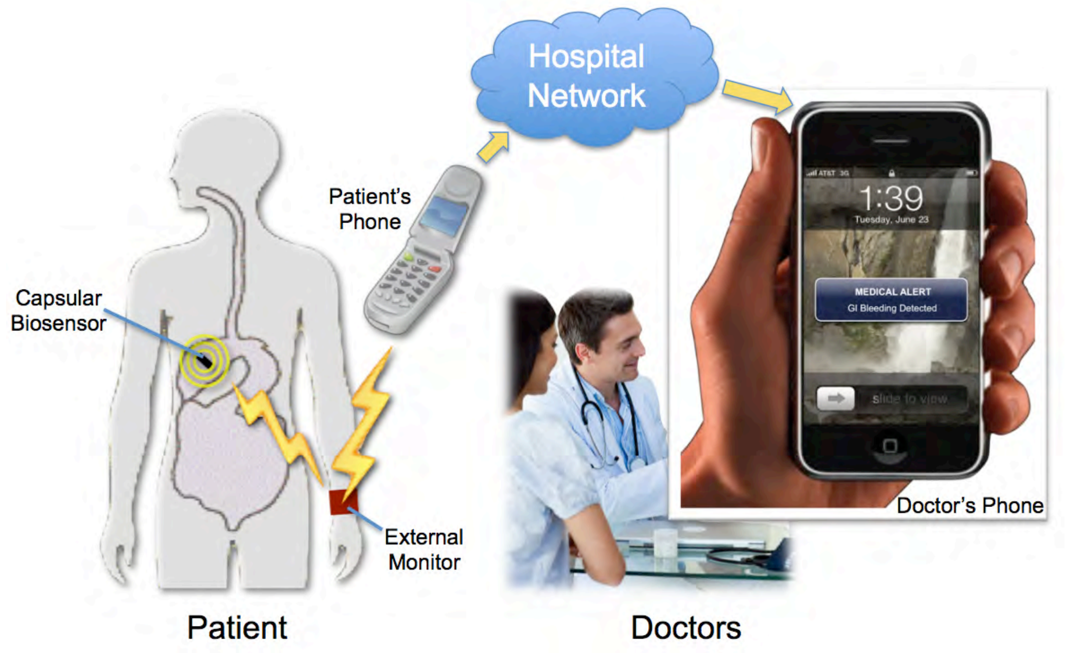

Figure 1.1: Body sensor network (BSN) for a swallowed capsular biosensor. The capsular sensor communicates through RF telemetry with an external monitor device, which forwards relevant information through an internet gateway device (e.g. mobile phone) to the hospital network so that doctors may receive the data or warnings on their device of choice (e.g. mobile phone)

1.4 Design Specifications

We impose the following design specifications on the device in order to be clinically relevant:

1. The device must be able detect Stage I GI bleeding in real-time (defined in Section 1.2.1).
2. The fluorescent dye used as a tracer for bleeding must be FDA approved.
3. Total emptying of the stomach occurs within $\sim$ 4 hours [25] . Therefore, we specify that the device must be able to detect blood for at least a time $T_{LOD}^0 \equiv 4$ hours, where T_{LOD}^0 is the specified minimum time limit of detection of the fluorometer. This is the bare minimum for detecting bleeding in the stomach. Ideally, we would like the device to continue searching for bleeding throughout the entire GI tract, and so we specify that the device time limit of detection should satisfy $T_{LOD} \geq T_{LOD}^0$.
4. The device must be able to wirelessly report its measurements to an external monitoring device.
5. The device must have enough power to continue functioning for a time $t \geq T_{LOD}^0$.
6. The device must be packaged in a capsular form factor, no larger than 27 mm length x 11 mm width to comply with the maximum swallowable capsular size allowable by FDA [R].

1.5 Realizing this Goal

In this thesis we describe the construction of all the fundamental components necessary to make a wireless implantable capsular biosensor according to the specifications in Section 1.4. Specifically, we detail the construction of a wireless lab-in-pill biosensor that detects a fluorescent tracer dye in human blood. We also characterize the fluorometer sensitivity with bench-top experiments evaluating the sensitivity of the fluoresence sensor as a method to detect internal bleeding. We find that the constructed device meets all specifications, significantly outperforming the specifications in a majority of areas.

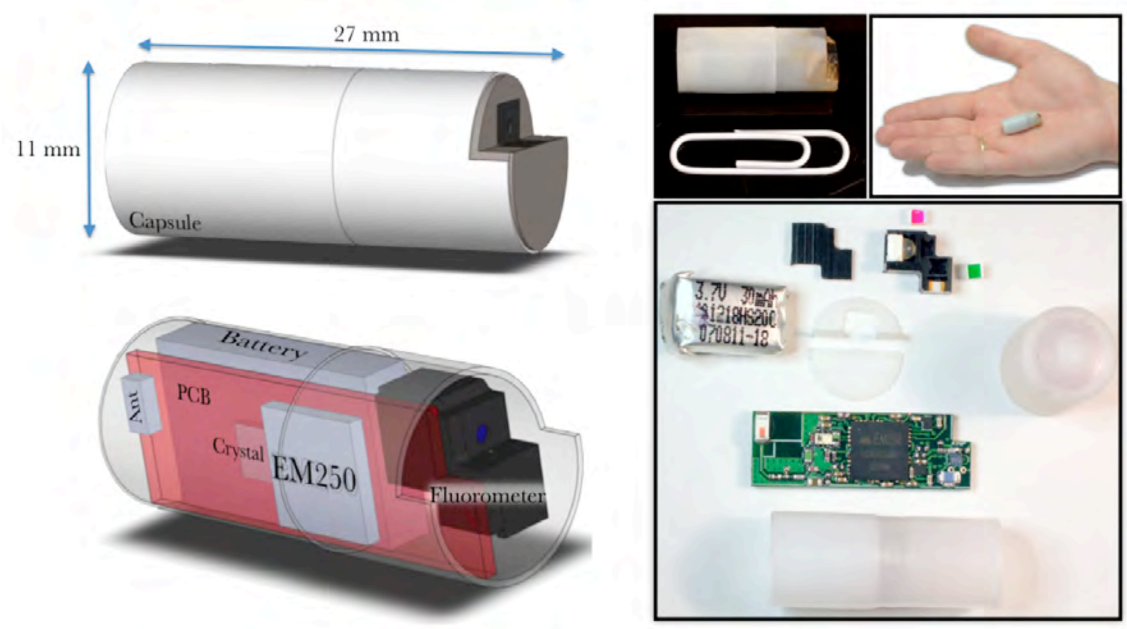

Figure 1.2: Left: Schematic of the lab-in-a-pill device presented in this thesis. Right: Constructed device pictured next to a paper clip, and in a hand, for scale. Also pictured, exploded view of constructed device components, including fluorometer, battery, printed circuit board, and capsule.

1.6 Thesis Outline

We begin this thesis by discussing how to a use a fluorescent tracer dye as an indicator for GI bleeding, and outline the design parameters and background theory for the construction of an appropriate miniature fluorometer (Chapter 2). Next, we present the background theory for the detection electronics and signal processing necessary to detect low level optical signals, and hence, low concentrations of dye (Chapter 3). We complete the device background with a discussion of the requirements of a lab-in-a-pill hardware platform, including software, power requirements, and wireless connectivity performance in the human body (Chapter 4). Next, we delineate the exact design of a miniature fluorophotometer to detect GI bleeding, based on the background presented in Chapters 1 - 2 (Chapter 5), and the design of the entire lab-in-a-pill hardware platform and packaging (Chapter 6). Finally, we detail the construction of the device (Chapter 7), and evaluate its sensitivity to detecting blood with a tracer dye (Chapter 8).

Chapter 2

Detecting Gastrointestinal Bleeding with a Fluorescent Tracer

2.1 Introduction

In this chapter we develop supporting theory for the detection of gastrointestinal bleeding using a fluorescent tracer injected into blood stream. In Sections 2.2 - 2.3 we explain the pharmacokinetics of a fluorescent tracer in the cardiovascular system, and show how to relate a measurement of the concentration to the total volume of blood in the stomach. In Section 2.4 we design a miniature fluorometer that can detect the concentration of a fluorophore in blood as it would be diluted in the stomach, and in Section 2.5 we develop theoretical expressions for total fluorescence intensity from the fluorophore when excited and detected by our fluorometer geometry. This will allow us to connect a measurement of the optical power to the concentration of fluorophore, and hence, blood volume.

2.2 Pharmacokinetics of an Intravenous Tracer

Any foreign substance, such as a blood tracer, introduced into the cardiovascular system will not remain in the blood stream indefinitely. The pharmacokinetic[1] properties of a tracer can be dictated by many complicated pathways. For example, since one of the primary functions of kidneys is to regulate blood chemistry, any foreign substance should eventually be filtered out (metabolized) by the kidneys, including a blood tracer [27]. Furthermore, the tracer can be absorbed by the walls of the blood vessels or diffuse out of the blood vessels [27]. Finally, the tracer can be chemically conjugated into a form of the tracer no longer detectable by the sensor [26].

Fortunately, for most intravenous tracers, these different elimination pathways all combine such that the total concentration of tracer in the blood stream, in its original detectable form, can be modeled as a simple exponential decay [26]. Therefore, we can define a total intravenous elimination half-life $t_{1/2}$ as the time it takes for exactly 50% of the injected fluorophore with initial intravenous concentration C_0 to be eliminated from circulation. For a tracer injection made at time $t = 0$, the total intravenous concentration $C_{iv}(t)$ at any time t after injection will be

$$C_{iv}(t) = C_0\, e^{-\beta t}, \tag{2.1}$$

where $\beta = \ln 2/t_{1/2}$ is the tracer's intravenous decay constant.

---

[1] Pharmacokinetics (definition): the process by which a drug is absorbed, distributed, metabolized, and eliminated by the body [26]

2.3 Blood Tracer Concentration as an Indicator of Acute GI Bleeding

2.3.1 Overview

Acute GI bleeding can be quantified as any amount of leaked blood volume $V_b(t)$ accumulated in the GI tract that has passed a threshold value V_a such that $V_b(t) > V_a$ at time time t. Therefore, we impose that the GI bleeding detector must be able to detect with high confidence at least a volume of a blood V_a in the GI tract. However, our detection method relies on measurement of the concentration of a tracer, and not a direct measurement of volume. Therefore, we need to understand how a measurement of the concentration can be used to classify GI bleeding.

If the intravenous concentration of tracer $C_{iv}(t)$ remains constant in time, then during a GI bleed, the concentration of tracer $C_s(t)$ in the GI tract is in one-to-one correspondence with the accumulated leaked volume $V_b(t)$, assuming nothing enters or exits the stomach on this time scale. However, in Section 2.2 we have seen that $C_{iv}(t)$ is in fact time dependent. This means that GI bleeds of equivalent accumulated volume $V_b(t)$ that occur with different rates can lead to very different tracer GI concentrations $C_s(t)$ at the same point in time t. Fortunately, we can find a minimum bound for $C_s(t)$ that indicates the minimum possible concentration that any blood volume can attain in the GI tract at a time t after injection. Therefore, we can define $C_a(V_a, t_0)$ as the minimum concentration attainable by the threshold bleed V_a within the time window spanned by $t \leq t_0$. Finding this minimum bound is a necessary and sufficient condition for detecting acute GI bleeding.

Finally, if the concentration limit of detection C_{LOD} of our tracer detector is

$$C_{LOD} \leq C_a(V_a, t_0), \tag{2.2}$$

then the detector will be able to detect any bleed that has passed the threshold V_a for all $t \leq t_0$. The time t at which Eq. (2.2) becomes an equality is then defined as the time limit of detection $t = t_{LOD}$. For $t > t_{LOD}$, we can no longer guarantee detection of V_a.

2.3.2 Modeling GI bleeding

While the GI tract has a complicated geometry, what we desire to find is the minimum concentration C_a associated with the threshold volume V_a of acute GI bleeding. As such, we only need to model the part of the GI tract where the lowest concentrations will be reached. Since the stomach is the most capacious segment of the GI tract, and behaves as a collection point for fluids, it is the the region where the lowest concentrations of tracer for equivalent blood losses will be attained. Thus, GI bleeding into the stomach serves as the model we use to derive C_a

A model for the system is shown in Fig. 2.1. We first make the following assumptions and definitions to simplify the analysis:

1. There is a volume V_0 of contents already present in the stomach.
2. The blood tracer detector is submerged in the stomach fluid for all time t, and continuously measures $C_s(t)$.
3. *Instant diffusion assumption*: any tracer that enters the stomach instantly diffuses to equilibrium, attaining a spatially constant concentration in the stomach.

A tracer injection with intravenous concentration C_0 is made at time $t = 0$. The intravenous concentration $C_{iv}(t)$ will exponetially decay according to Eq. (2.1). We parametrize GI bleeding by some instantaneous rate $R_b(t)$, which can be any positive function (such as a continuous, step, or delta function), and thus the only constraint is that $R_b(t) \geq 0$. The total volume of blood $V_b(t)$ accumulated in the stomach at any time t will be

$$V_b(t) = \int_0^t R_b(t')\,dt'. \tag{2.3}$$

We set the initial condition of the system to $V_b(0) = 0$ because there is no tracer before injection. The instantaneous amount of tracer dN that is transported into the stomach between t and $t + dt$ is given by $dN = C_{iv}(t) \cdot dV_b$, and the total amount of

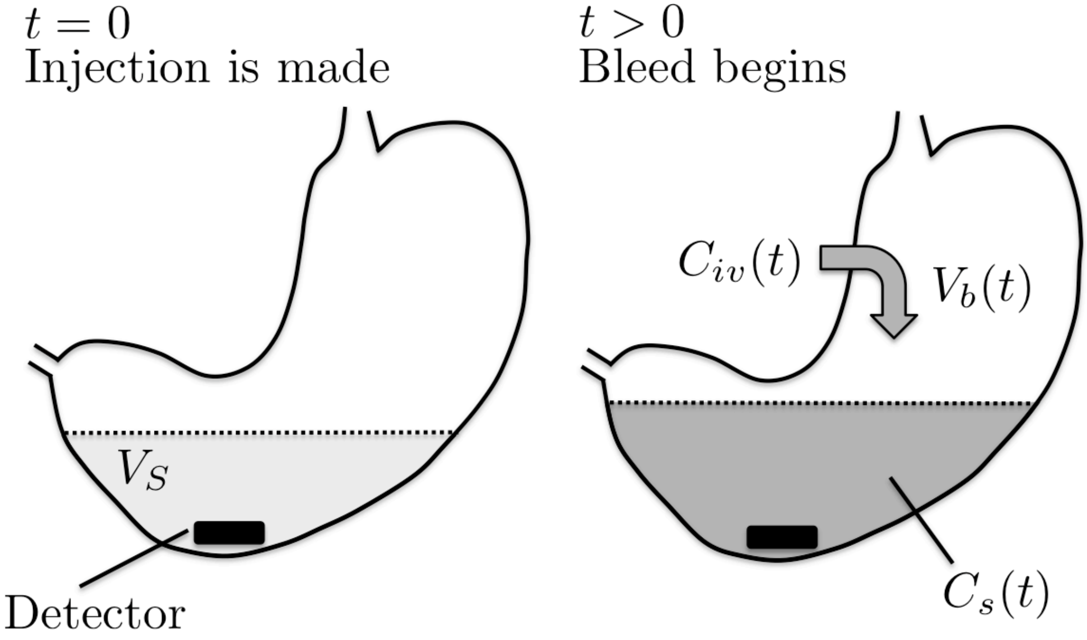

Figure 2.1: (a.) Time $t = 0$: The tracer injection is made. A tracer detector has been submerged in the stomach contents with volume V_s. (b.) A bleed occurs over some time period $t > 0$. The intravenous concentration is $C_{iv}(t)$, accumulated volume of bleed at time t is $V_b(t)$ and concentration of tracer in the stomach $C_s(t)$.

tracer $N(t)$ transported into the stomach is

$$N(t) = \int_0^t C_{iv}(t') \cdot dV_b = \int_0^t C_{iv}(t')\, R_b(t') dt'. \tag{2.4}$$

Although we don't know what the bleeding rate $R_b(t)$ is, for a certain total blood loss $V_b(t)$, the amount of tracer transported into the stomach will be bounded. Since $C_{iv}(t)$ exponentially decays in time, we can perform integration by parts on Eq. (2.4) and use Eq. (2.1) - Eq. (2.3) along with the initial conditions to find that

$$\begin{aligned} N(t) &= C_{iv}(t')V_b(t')\Big|_{t'=0}^{t'=t} - \int_0^t V_b(t')\, \frac{dC_{iv}}{dt'} dt' && (2.5) \\ &= C_{iv}(t)V_b(t) + \beta \int_0^t V_b(t')C_{iv}(t')dt' && (2.6) \\ &\geq C_{iv}(t)V_b(t). && (2.7) \end{aligned}$$

Here we have used the fact that the second term in Eq. (2.6) is always ≥ 0 because $\beta, V_b(t), C_{iv}(t) \geq 0$. We now find that the total concentration $C_s = N/V_{tot}$ of tracer in the stomach with initial stomach contents volume V_0 and total volume $V_{tot}(t) = V_0 + V_b(t)$, following Eq. (2.7) is similarly bounded such that

$$C_s(t) \geq \left(\frac{V_b(t)}{V_0 + V_b(t)} \right) C_{iv}(t). \tag{2.8}$$

Therefore, the minimum concentration C_a that the tracer detector must be able to measure, in order to detect *any* type of bleed that leads to a total blood loss V_a after a time $t = t_0$ is

$$C_a(V_a, t_0) = \left(\frac{V_a}{V_0 + V_a} \right) C_{iv}(t_0) \tag{2.9}$$

Intuitively, this corresponds to the worst case scenario when the volume V_a is instantaneously injected into the stomach at the time $t = t_0$. Since the intravenous concentration $C_{iv}(t)$ is monotonically decreasing, the lowest concentration at any time is the current concentration, and a blood volume V_a injected instantaneously at $t = t_0$ will attain a lower concentration in the stomach than if V_a was injected in any other way when $t < t_0$. Thus, if the fluorometer is sensitive enough to detect $C_a(V_a, t_0)$, we can say with certainty that it can detect *any* type of bleed $V_b(t) \geq V_a$ during the time $t \leq t_0$.

Furthermore if we measure a concentration of $C_S(t_0)$, we can place an upper bound on the total accumulated blood volume. Rearranging Eq. (2.8), we find that the bleeding volume $V_b(t_0)$ is bounded by

$$V_b(t_0) \leq \left(\frac{C_s(t_0)}{C_{iv}(t_0) - C_s(t_0)} \right) V_0, \tag{2.10}$$

where we always choose the detection concentration $C_s(t) < C_{iv}(t)$, such that the current concentration in the stomach is less than the current intravenous concentration. Eq. (2.10) says that for a measured concentration C_s at $t = t_0$, we know for certain that the volume is less than a certain value.

Finally, we define the time limit of detection t_{LOD} as the time when the minimum possible stomach concentration C_a for V_a of blood loss reaches concentration the limit of detection C_{LOD} of the detector, such that $C_{LOD} \ = \ C_a(t_{LOD})$. Using Eq. (2.9), we find that

$$t_{LOD} = \beta^{-1} \ln \left[\left(\frac{V_a}{V_0 + V_a} \right) \frac{C_0}{C_a} \right] \tag{2.11}$$

This is the total time that the tracer detector can operate after initial injection such that any GI bleeding event with volume V_a can still be detected. For time $t > t_{LOD}$, there will exist ways to reach V_a without reaching $C_a = C_{LOD}$, and thus we will no longer be able to reliably detect acute GI bleeding past this point.

2.4 Detecting the Concentration of a Tracer

2.4.1 Overview

We use a fluorescent dye (fluorophore) as a blood tracer, and thus must design a fluorometer that is capable of detecting physiological concentrations of fluorophore. In this section we describe our fluorometer geometry and develop supporting theory that relates how a measurement of fluorescence intensity within our geometry provides a measurement of the fluorophore concentration.

2.4.2 Fluorometry

To measure the amount of fluorescence emanating from a solution of fluorophore, we must first illuminate the sample with light of a wavelength corresponding to the excitation energy of the fluorophore molecules, and detect the light that is emitted. At any wavelength of incident light λ, the fluorophore will have two pertinent properties:

- **Molar Absorptivity** $\alpha(\lambda)$ ($\mathrm{cm}^{-1}\mathrm{M}^{-1}$): a parameter that defines how strongly a substance absorbs light at wavelength λ per molar concentration of the substance and per centimeter of propagation through the substance.
- **Quantum Yield** Q (%): the percentage of absorbed photons that are converted into emitted photons, which have a peak emission wavelength λ_{em}.

Each time an excitation photon is absorbed by a dye molecule it emits a photon of lower energy with a probability given by the quantum yield Q. The basic scheme for fluorescence detection is shown in Fig. 2.2.

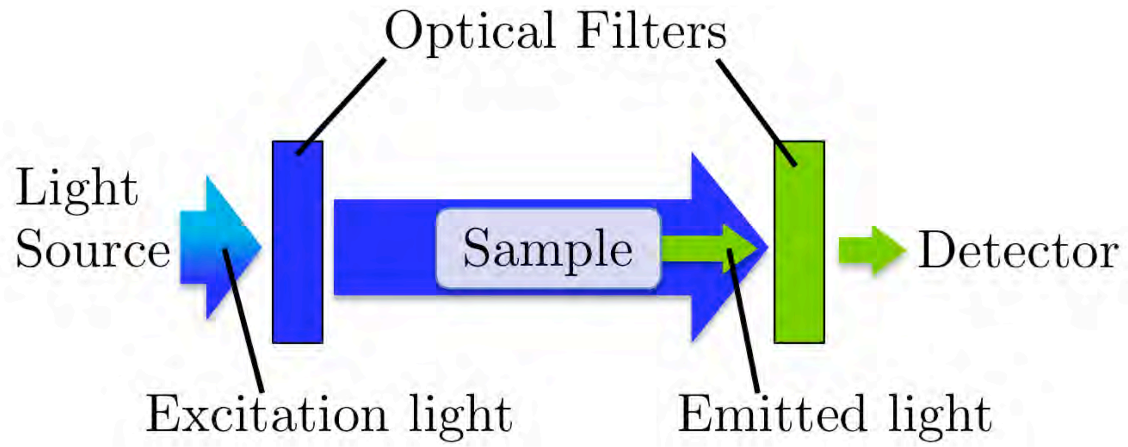

Figure 2.2: Basic geometry for a fluorometer.

A typical setup [28] includes an excitation source and an optical detector. The detector will be sensitive to the excitation light as well as the emitted fluoresence and so a pair of optical filters, after the light source and before the detector, are used to make sure that the excitation light does not reach the detector. The filters are chosen such that their passbands do not overlap, and thus excitation light reaching the sample should not pass through the emission filter.

2.4.3 Optical Filters and Pinholes

To construct a high sensitivity fluorometer it is necessary to use optical filters that provide a very high degree of isolation between excitation and emission light. Since the excitation and emission wavelengths of fluorophores that we consider are typically within 50 nm of each other, this requires that the filters also exhibit sharp cut offs with high attenuation outside the pass band. Interference filters provide the best performance regarding these properties, and for this reason are most commonly used in fluorescence microscopy.

Interference filters use the principle of optical interference to selectively pass light of certain wavelengths while reflecting all others [29]. An stack of alternating dielectrics forms a 1-D periodic array that can be carefully designed create low pass (LP), high pass (HP), and band pass (BP) optical filters. However, the passband properties of the filters are optimized for light at normal incidence. Light that is incident at an angle to the normal will experience a different passband as it will encounter a different layer periodicity. In fluorescence microscopy, this problem is mitigated by using focusing and collimation optics to ensure that the excitation and emission light is always at normal incidence with respect to the optical filters. In designing a miniature integrated fluorometer, we do not have the luxury of space to satisfy this condition. However, we can constrain allowed angles by adding pinholes to the filters. We will use a low-pass filter with a cut-off at λ_L as our excitation filter and a high-pass filter with cut-on at λ_H as our emission filter. The width of the isolation region is thus $\Delta = \lambda_H - \lambda_L$. For a hi-pass dielectric interference filter, light at non-normal incidence will experience a blue-shifted cut-on [30] given by:

$$\lambda'_H(\theta) \approx \lambda_H \sqrt{1 - \frac{\sin^2\theta}{n_f^2}}, \tag{2.12}$$

where θ is the angle of incidence from normal, n_f the dielectric filter's effective index of refraction, and λ'_H the blue-shifted high-pass cut-on wavelength. If the angle of incidence is large enough, the isolation will be completely eliminated, and excitation light will be free to leak through the emission filter. Thus we need to constrain θ such that

$$\Delta = \lambda'_H(\theta) - \lambda_L > 0 \tag{2.13}$$

A pair of pinholes on either side of optical filter will constrain the angles of light that are passed through the filter, Fig. 2.3.

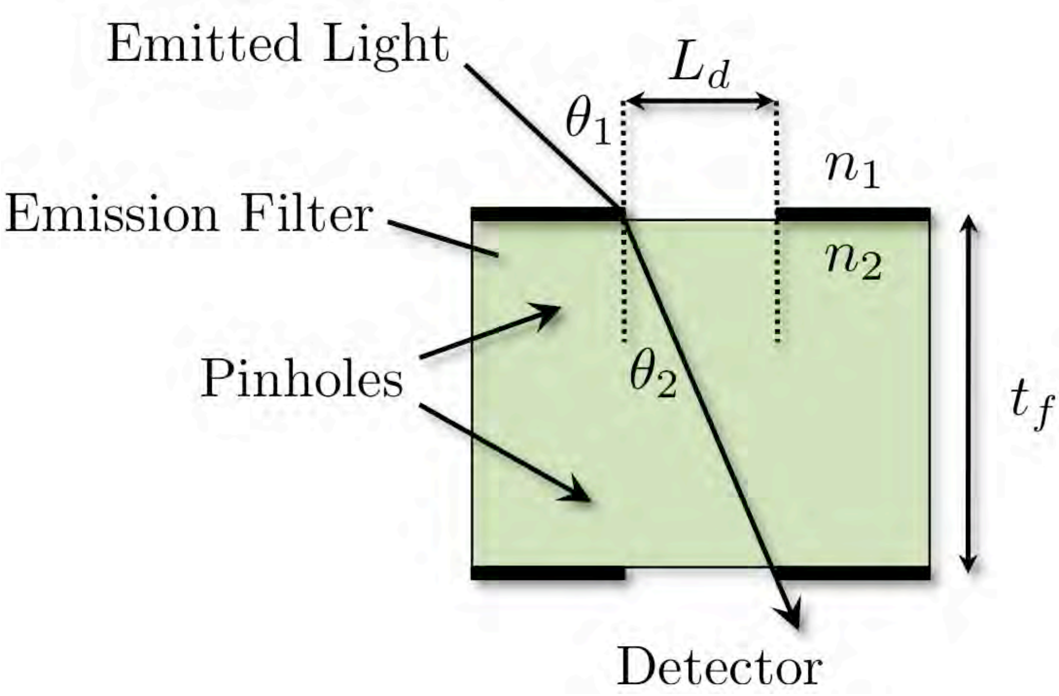

Figure 2.3: Light refraction through a glass optical filter with pinholes. Incident and refracted angles are θ_1 and θ_2 respectively. Incident medium index of refraction is n_1 and filter index is n_2. Filter thickness is t_f and pinholes have diameter L_d.

In an medium with index of refraction $n_1 = n_m$, and a glass filter with effective index $n_2 = n_f$, the incident light will undergo refraction according to Snell's law [31] such that

$$\frac{n_m}{n_f} = \frac{\sin\theta_2}{\sin\theta_1}, \tag{2.14}$$

where θ_1 is the angle of incidence and θ_2 is the refracted angle. Finally, we can constrain θ_2 by using pinholes with diameter L_d such that

$$L_d = t_f \tan\theta_2, \tag{2.15}$$

where t_f is the thickness of the optical filter. Combining Eq. (2.12) - (2.15), we arrive at a constraint for the pinhole diameter:

$$L_d < \sqrt{\frac{n_m^2\, t_f^2 \left(1 - \dfrac{\lambda_L^2}{\lambda_H^2}\right)}{1 - n_m^2 \left(1 - \dfrac{\lambda_L^2}{\lambda_H^2}\right)}}. \tag{2.16}$$

2.4.4 Ultra-Compact Geometry

To fit inside the capsular biosensor, we need an ultra-compact version of the fluorometer geometry. We place the excitation source and detector at right angles (Fig. 2.4) for the following reasons:

1. We desire maximal compactness of our detection system so that it can fit inside the capsular size. The right angle geometry ensures that the optical components can be placed as close as possible while overlapping as much of the sample volume as possible.

2. The optical filters have a finite attenuation for light outside their passband and thus a finite amount of stop-band light leakage. Therefore, it is preferable to reduce the amount of excitation light incident on the emission filters to reduce excitation leakage. The right angle geometry ensures that the excitation source is never pointing at the detector while still optimizing device compactness.

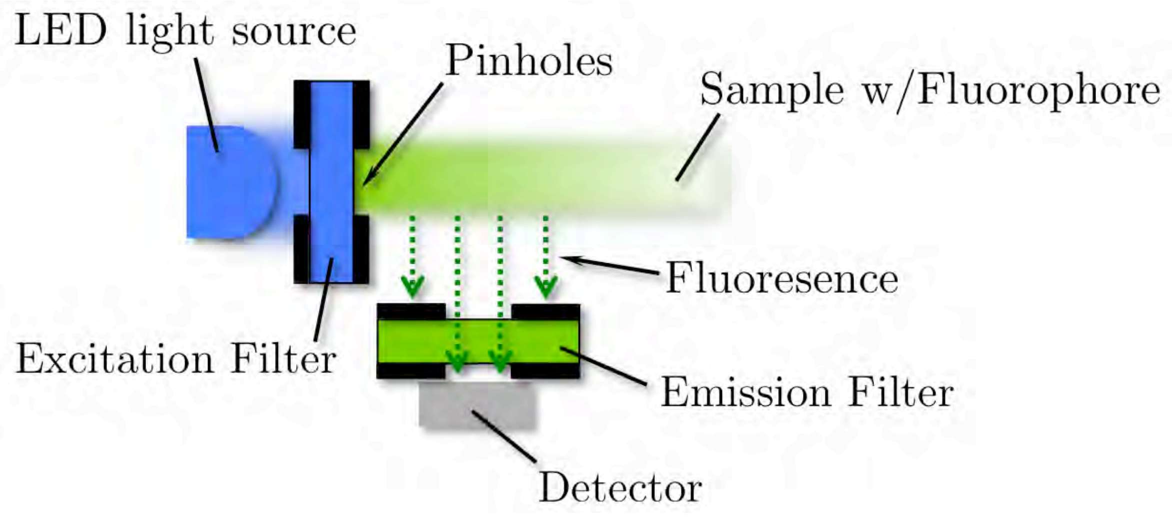

Figure 2.4: Geometry for an integrated miniature fluorometer.

The LED light source, which has an integrated lens, emits excitation light in the direction of the sample volume. An excitation filter prevents any light at the emission wavelength from entering the detection volume. A pair of coaxial pinholes on either side of the excitiation filter ensure that any light scattered from distant interfaces is blocked and creates a well-defined volume of excitation light in the detection region. This light is then absorbed by the fluid in the detection region and partially converted to fluorescent emission. The fluorescence is emitted isotropically, and a fraction of this light is emitted in the direction of the detector. The emitted light then passes through an emission filter which blocks any excitation light and strikes the detector surface. A pair of coaxial pinholes on either side of the emission filter geometrically constrain the angle of incidence of light on the emission filter to $\theta < \theta_c$.

2.4.5 Fluorometer Model

We first parametrize the model with the following assumptions and definitions (Fig. 2.5):

1. Each point in the sample volume $dV = dx \cdot dy \cdot dz$ is treated as a point absorber/point source emitter parametrized by its distance to the excitation filter x, from the detector y, and from the xz-plane which bisects the pinholes.

2. The excitation path pinhole is circular with diameter L_i, and height from the detector surface y_0. This is also the closest distance between an excited fluorophore and the detector

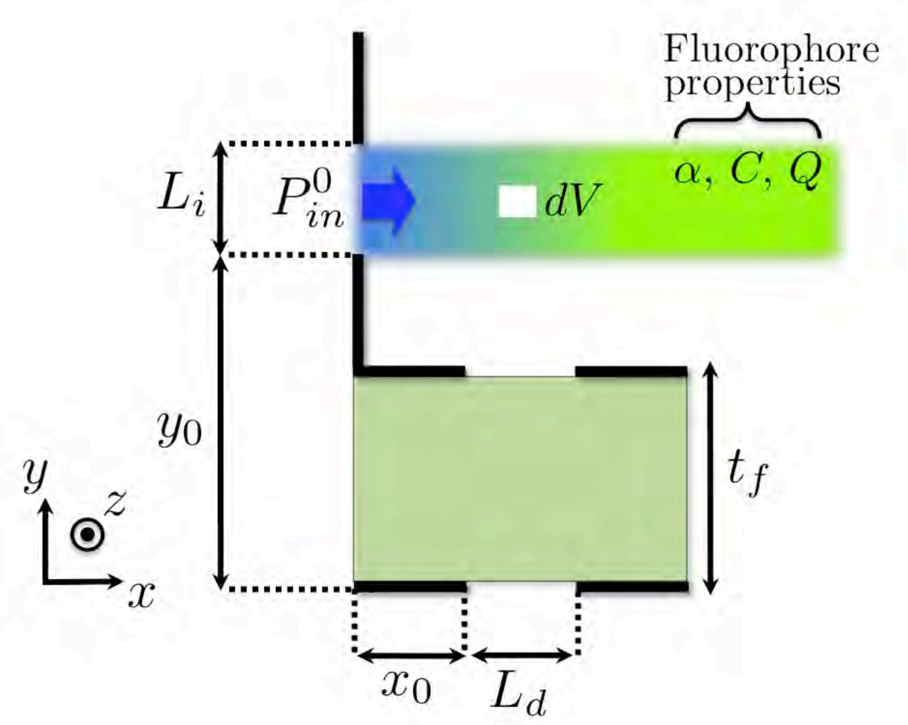

Figure 2.5: Model for parametrizing the integrated fluorometer.

3. Input light is monochromatic with wavelength λ_{ex} and is a perfectly collimated plane wave with an input power $P_{in}^0(y,z)$ at $x = 0$. The input pinhole bounds the excitation light in y and z such that the excitation light is constant in the cylindrical volume defined by the excitation pinhole

$$P_{in}^0(y,z) = \begin{cases} P_0 & \sqrt{(y - y_0 - L_i/2)^2 + z^2} \leq L_i/2 \\ 0 & elsewhere \end{cases} . \tag{2.17}$$

4. The fluorophore being detected is an isotropic aqueous mixture with concentration C_s, molar absorptivity $\alpha(\lambda)$, and quantum yield Q. The fluorophore absorption coefficient μ_f is thus defined as

$$\mu_f(\lambda) = \alpha(\lambda)\, C_s \tag{2.18}$$

5. The medium has a total absorption coefficient

$$\mu_(\lambda) = \mu_0(\lambda) + \mu_f(\lambda), \tag{2.19}$$

   where $\mu_0(\lambda)$ is the background absorption coefficient of the medium without fluorophore (due to blood or other stomach contents) at wavelength λ. Furthermore, we define $\mu_1 = \mu(\lambda_{ex})$ and $\mu_2 = \mu(\lambda_{em})$ and similarly $\mu_{f1} = \mu_f(\lambda_{ex})$, and $\mu_{f2} = \mu_f(\lambda_{em})$.

6. The detector pinholes are circular with diameter L_d.

7. The area of the detector surface is $A_d = \pi L_d^2/4$. The the detector is located at x_0.

8. The distance between the detector surface and medium is the thickness of the emission filter t_f.

2.5 Relating the Fluorescence to Concentration

2.5.1 Excitation Path

Since the excitation light only propagates in the x-direction, and the input power is constant in the xz-plane for points inside the beam volume, the optical absorption can be treated as a one dimensional problem. The amount of excitation intensity absorbed between x and dx (I_{abs}) is related to the light intensity reaching that point $I_{in}(x)$ by

$$I_{abs} = I_{in}(x)\, \mu_1\, dx. \tag{2.20}$$

Since these photons are absorbed, the intensity decreases by this amount and so the change is $dI_{in} = I_{abs}$. This results in the well known Beer-Lambert [31] law for incident light power as a function of depth:

$$I_{in}(x) = I_0\, e^{-\mu_1 x}, \tag{2.21}$$

where I_0 gives the incident intensity at $x = 0$, and I_{in} is now the amount of light intensity at each point x that is left in the incident beam and available for absorption. The intensity absorbed by the fluorophore within each differential element dx can be found by substituting Eq.(2.21) into Eq.(2.20) to find that

$$dI_{in} = \left(I_0\, e^{-\mu_1 x}\right)(\mu_{f1}\, dx)\,. \tag{2.22}$$

Since the incident intensity is $I_0 = \frac{P_0}{\pi (L_i/2)^2}$, then the total power absorbed by each differential volume element dV is

$$\mathrm{d}P_{in} = \left(\frac{4P_0}{\pi\, L_i^2}\, dy\, dy\right) e^{-\mu_1 x}\, (\,\mu_{f1}\, dx)\,. \tag{2.23}$$

Here we can intuitively understand that the first term is the initial incident light power in the area $dy\,dz$, the second term the amount of light remaining in the beam after propagating a distance x through the fluorophore solution, and the third term the amount of light absorbed by the fluorophore in the region $x + dx$.

2.5.2 Emission Path

We now define a cylindrical coordinate system where $r = \sqrt{(x - x_0)^2 + z^2}$ and the detector radius is $r_d = L_d/2$, for the emission path Fig. 2.6. We will treat each volume element in the medium as a point-source emitter of fluorescence with radiated fluorescence power dP_f, which is emitted isotropically. For light emitted isotropically, the fraction of light reaching a surface at a distance is

$$f = \frac{\Omega}{4\pi}, \tag{2.24}$$

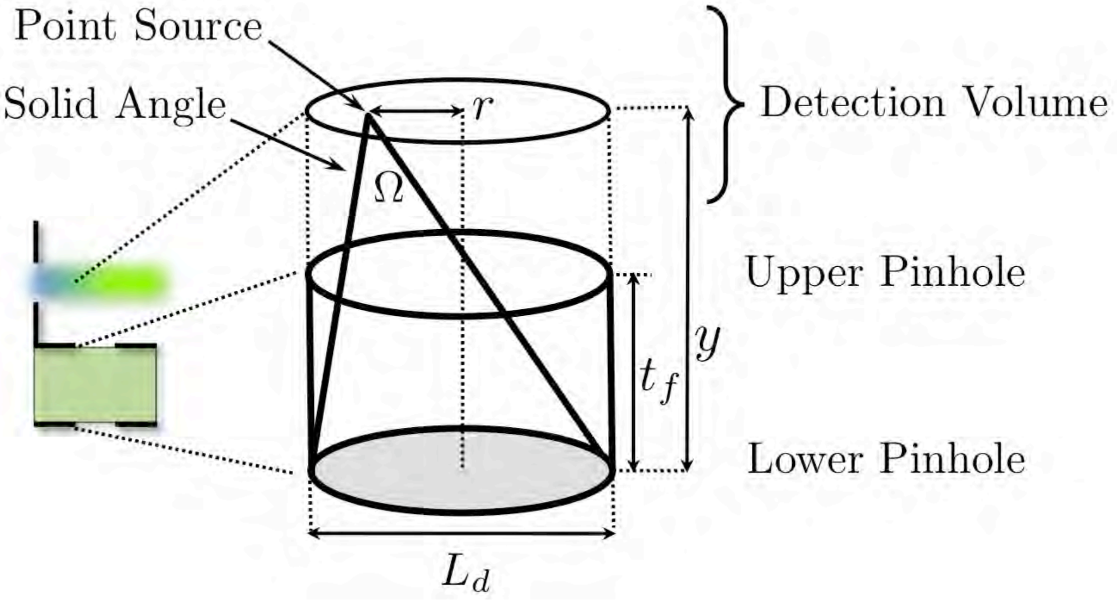

Figure 2.6: Model for emitted light. Each point emits light into the solid angle Ω which subtends the detector area described by $A_d = \pi\, L_d^2/4$

where Ω is the solid angle the surface subtends. In the present case the detector surface is a planar circle which will define a conical solid angle that has a planar half angle θ defined by $\Omega = 2\pi\left(1 - \cos\theta\right)$. Thus, the fraction of detected light is

$$f = \frac{1}{2}\left(1 - \cos\theta\right), \tag{2.25}$$

where in the present coordinate system, θ is related to emitter position by

$$\theta = \frac{1}{2}\tan^{-1}\left(\frac{r_d - r}{y}\right) + \frac{1}{2}\tan^{-1}\left(\frac{r_d + r}{y}\right). \tag{2.26}$$

We define the detection volume as all points $r \leq r_d$. We assume that light originating from points $r > r_d$ will be partially or fully occluded from the detector, and we disregard this contribution.

High Aspect Ratio

For cases where the emission filter is thick and pinhole is narrow, we will have a high aspect ratio, and $r_d, r \ll y$, and thus both arguments in the inverse tangents are also $\ll 1$. Taylor expanding to lowest order in those arguments gives

$$\cos\theta \approx 1 - \frac{1}{8}\left(\frac{2r_d}{y}\right)^2, \tag{2.27}$$

such that the distance from the center r drops out in the $r \leq r_d$ region. The fraction of emitted light that reaches the detector is thus

$$f(y) = \left(\frac{L_d}{4y}\right)^2. \tag{2.28}$$

Intuitively, this says that the area subtended by the solid angle Ω at a distance y can be approximated by the circular detector area $A_d = \pi r_d^2$ for this high aspect ratio and small deviations from center. Thus the contribution to the detected power of each point is only dependent on its height y; the x position is relevant for the absorbed power, but not emitted power.

In this high aspect ratio geometry, we can also include optical absorption due to the medium. The emitted light will be absorbed as it propagates between y and t_f with an absorption coefficient μ_2 such that

$$f(y) = \left(\frac{L_d}{4y}\right)^2 e^{-\mu_2\left(y-t_f\right)}. \tag{2.29}$$

2.5.3 Full Optical Path

Each volume element will absorb light $dP_{in}(x)$, convert it to emitted light with quantum yield Q, and then a fraction $f(y)$ of that light will reach the detector surface. Thus the power incident on the detector surface due to each volume element is

$$dP_{det}(x, y) = dP_{in}(x) \cdot Q \cdot f(y), \tag{2.30}$$

The cylindrical sample volume can be described in our rectangular coordinates such that the integral is

$$P_{det} = Q \int_{-r_d}^{r_d} \int_{x_0+L_d/2-\sqrt{r_d^2-z^2}}^{x_0+L_d/2+\sqrt{r_d^2-z^2}} \left(\frac{4P_0}{\pi\, L_i^2}\right) e^{-\mu_1 x}\, \mu_{f1}\, dx\, dz \int_{y_0}^{y_0+L_i} \left(\frac{L_d}{4y}\right)^2 e^{-\mu_2\left(y-t_f\right)} dy. \tag{2.31}$$

This expression implicitly relates the fluorophore concentration C_s through μ_1, μ_2, and μ_{f1} to the detected power. We have used the high-aspect ratio geometry for the emission term using Eq. (2.29).

Low Concentrations

For high levels of dilution with water and short pathlengths characteristic of our fluorometer, we can assume that $\mu_1\, x \ll 1$ and $\mu_2\, y \ll 1$. Expanding to lowest order in these arguments and using Eq. (2.19), the integral reduces to

$$P_{det}(C_s) \approx C_s \cdot \left[\frac{P_0\, Q\, L_d^4\, \alpha(\lambda_{ex})}{16\, L_i^2} \left(\frac{1}{y_0} - \frac{1}{y_0 + L_i} \right) \right]. \tag{2.32}$$

Thus for low concentrations where light attenuation is negligible, the total power incident on the detector surface P_{det} depends linearly on the fluorophore concentration in the stomach C_s.

2.6 Conclusion

In this chapter we have shown how to use a measured concentration of tracer in the stomach to extrapolate a lower bound on the stomach fluorophore concentration given a specific leaked bleed volume, an upper bound on the leaked blood volume given a specific measured concentration, and the time limit of detection of the fluormeter. We have also developed supporting theory for a integrated fluorometer that can measure the optical power of emitted fluorescence from a fluorescent tracer and shown how a measurement of this signal can be used to extrapolate the tracer's concentration.

Chapter 3

Detection Electronics and Signal Processing

3.1 Introduction

In order to measure radiated fluorescence, incident photons must be transduced into an electrical signal that can be amplified and sampled by an analog digital converter (ADC). This chapter details the design of a circuit to perform this task with a particular emphasis on minimizing noise through a combination of analog and digital filters. We first present an overview of photodiode physics (Section 5.4) along with a way to model the photodiode as a circuit element. Next, we discuss the different sources of noise (Section 3.3) and develop the framework with which to calculate noise in our circuitry. Subsequently, we present the circuitry used to amplify the transduced signal (Section 3.4) and compute the total noise of the circuitry. Finally we show how the analog signal is digitized and filtered in software (Section 3.5), and calculate the overall input referred noise of the final signal (Section 3.6).

3.2 Silicon Photodiodes

3.2.1 Overview

There are various discrete components that can be used to transduce an optical signal. For a signal in the visible spectrum, the most common is the silicon photodiode, which offers the best combination of optical bandwidth, responsivity, sensitivity, and accuracy [32]. A silicon photodiode generates a current proportional to the incident optical power and is capable of detecting a large range of optical intensities, which in context of fluorometry, corresponds to a range of fluorophore concentrations spanning many orders of magnitude. Thus, the photodiode is our transducer of choice and is the starting point of this chapter.

3.2.2 Photodiode Physics

Silicon has a bandgap of of 1.12 eV, and thus light with wavelengths below 1100nm can be absorbed [33]. In bulk silicon, the generated electron/hole pairs will quickly recombine and cannot be used to create a sustained current or voltage. However, if a silicon p/n junction (diode) is used instead, the electron/hole pairs photo-generated in the depletion region are separated by the diode's built-in voltage quicker than they can recombine, and the generated carriers can contribute to a measurable current or voltage. Thus, a photodiode is simply a semiconductor p/n junction that has been configured to have its depletion region exposed to light. With no incident light it behaves as a typical diode with I-V characteristics governed by the Shockley ideal diode equation: [34]

$$I_{diode} = I_d \left(e^{V_D/V_T} - 1 \right), \tag{3.1}$$

where I_d is the photodiode dark current, V_D the voltage bias placed across the photodiode, $V_T = k_B T/e$ the thermally generated built-in reverse bias voltage.

When the depletion region is exposed to light by photons close in energy to the band-gap of the semiconductor, they are absorbed by the semiconductor. This is a linear process in which each photon has some probability $Q \leq 1$ (diode quantum efficiency) to generate a single electron/hole pair. The rate of photo-assisted generation is directly proportional to the incident power such that

$$I_{photo} = R(\lambda) P_{in}(\lambda), \tag{3.2}$$

where I_{photo} is the generated photocurrent, $R(\lambda)$ the wavelength dependent responsivity measured in Amps/Watt (which implicitly accounts for Q), and $P_{in}(\lambda)$ the incident optical power. A typical absorption spectrum [35] of a silicon photodiode is shown in Figure Fig. 3.1.

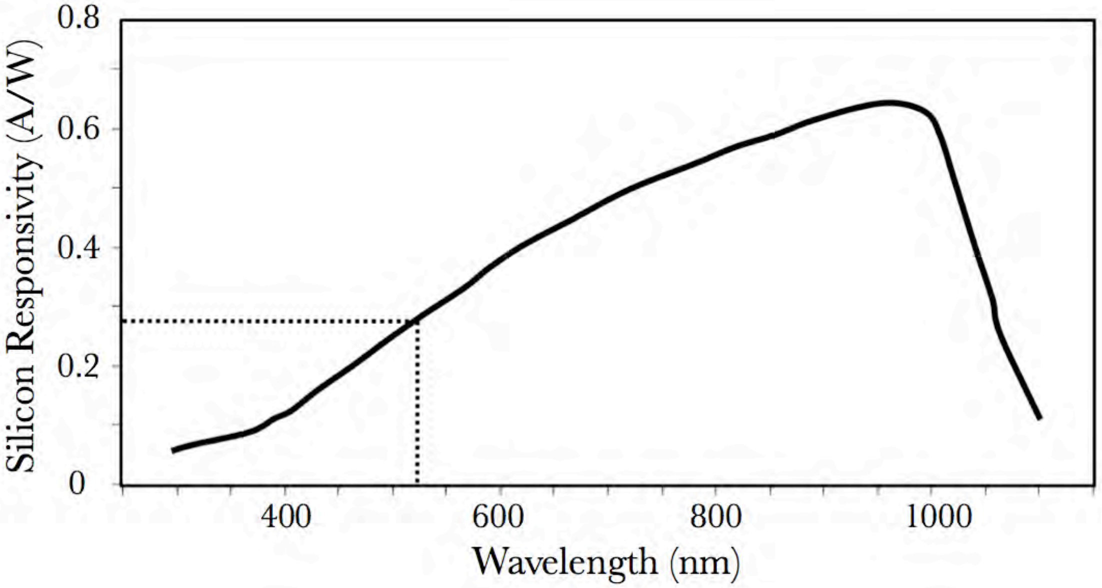

Figure 3.1: Silicon PIN photodiode responsivity. The responsivity at 520nm is marked as it is the peak emission wavelength for the fluorescence of fluorescein [35].

The photogenerated electrons and holes are separated out of the active region by the p/n junction built-in voltage V_T, with electrons swept to the anode and holes to the cathode. Thus the generated photocurrent is in the direction of reverse bias, and the total current

$$I_{PD} = I_{diode} - I_{photo} = I_d \left(e^{V_D/(k_B T)} - 1\right) - I_{photo}. \tag{3.3}$$

3.2.3 Photodiode Circuit Model

To explore the behavior of a photodiode it is useful to use a simplified photodiode model in which an incident power dependent current source and regular diode are placed in parallel (Fig. 3.2). First we examine the photodiode as a generator of voltage. In an open circuit configuration ($Z_{load} = \infty$), the photodiode will generate a current I_{photo} that will cause accumulating charge to build up opposing the reverse bias and eventually causing a forward bias voltage which activates the diode leading to a diode current. Equilibrium is reached when $I_{photo} = I_{diode}$ and occurs when the forward bias voltage reaches

$$V_D(I_{photo}) = V_T \ln\left(\frac{I_{photo}}{I_d} + 1\right). \tag{3.4}$$

Using this voltage as a measurement of the incident light power is highly nonlinear and is not preferred.

However, if we instead provide an external load to dissipate the photocurrent the charge cannot build up in the photodiode, I_{photo} can be directly measured. If V_D is

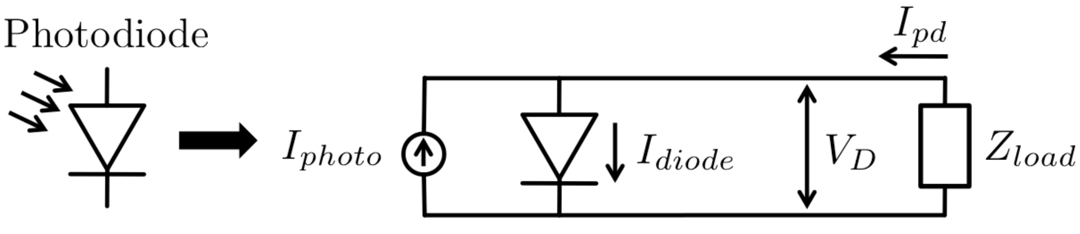

Figure 3.2: Photodiode circuit model. A photocurrent source is placed in parallel with an ideal diode and dissipated through a load resistor.

held fixed (to be discussed later), then Eq. (3.2) and Eq. (3.3) give

$$I_{PD} = -R \cdot P_{in} + I_{diode} \begin{cases} I_{diode} = 0, & V_D = 0, \quad \text{Photovoltaic} \\ I_{diode} = -I_d, & V_D < 0, \quad \text{Photoconductive.} \end{cases} \tag{3.5}$$

Now the measured current is linear with respect to the incident light power with potentially a DC offset value equal to the junction dark current. The two operating modes are the zero bias *photovoltaic* mode, and the reverse biased *photoconductive* mode. In order to choose which mode to operate in, it is necessary to analyze the noise characteristics of the photodiode.

3.3 Noise

3.3.1 Overview

The detection of current generated by a photodiode is limited by fundamental electronic noise. The two most common types of broadband electronic noise in circuits are 1/f noise and white noise. 1/f noise results from a variety of effects whose origin is not well known and typically manifests itself as a long term random drift of the measured signal with a noise power spectral density $P \propto 1/f^{\alpha}$ where $1 \leq \alpha \leq 2$ [36]. By definition, this noise will exist primarily at lower frequencies (Fig. 3.3).

At higher frequencies, the noise is dominated by broadband white noise which is constant at all frequencies. The frequency at which the white noise begins dominate 1/f noise is the corner frequency f_C. Since the fundamental noise power density floor of a circuit is the white noise, sensitive measurements are always made above the corner frequency, and for this purpose it is important to design a circuit with a low white noise content.

3.3.2 General White Noise

White noise manifests itself in time as a stationary random processes: the amplitude of a noise in time will have a well defined mean and variance, both of which are time invariant [37]. Furthermore, since the mean value is zero for a white noise signal $n(t)$, the noise variance in time is

$$\sigma_n^2 = \mathrm{Var}(n) = \left\langle n^2 \right\rangle - \left\langle n \right\rangle^2 = \left\langle n^2 \right\rangle , \tag{3.6}$$

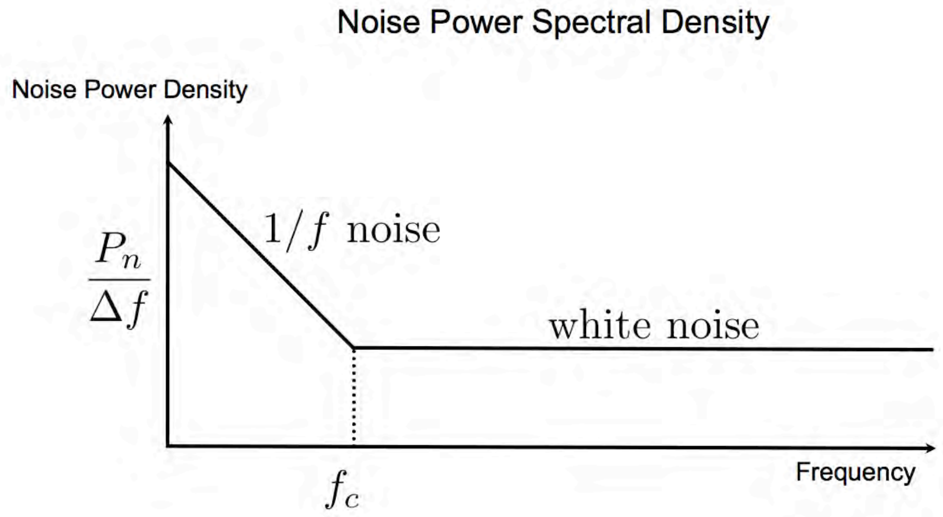

Figure 3.3: Typical noise power spectral density. For $f < f_c$ noise with a characteristic 1/f power spectrum dominates. For $f > f_c$ the noise is white: its power spectrum is equal at all frequencies

and is related to autocorrelation function $\langle n(t)n(0)\rangle$ and thus noise power spectral density $s(f)$ through the Wiener-Khinchin theorem [37]:

$$\sigma_n^2 = \langle n(t)n(0)\rangle \Big|_{t=0} = \int_{-\infty}^{\infty} s(f)e^{i2\pi ft}df\Big|_{t=0} \tag{3.7}$$

This holds true for both white noise, and filtered white noise. The variance of the measured noise signal in time due to a noise power in a finite measurement bandwidth $\Delta f = f_2 - f_1$ is thus

$$\sigma_n^2 = \int_{-f_2}^{-f_1} s(f)df + \int_{f_1}^{f_2} s(f)df = \int_{f_1}^{f_2} S(f)df, \tag{3.8}$$

where we have used the fact that the noise power spectrum is a symmetric function of frequency, and defined the single sided power spectrum $S(f) = 2\,s(f)$. If the noise power is white, then $S(f) = S_0$ and

$$\sigma_n^2 = S_0\,\Delta f. \tag{3.9}$$

3.3.3 Sources of White Noise

Shot Noise

The first fundamental broadband white noise source arrises directly from the discrete nature of the charge carriers in a drift current. Whenever a drift current is generated by a source of completely uncorrelated sequence of discrete events, such as photons being converted to electronics in a photodiode, the current will have random fluctuations about a mean value characteristic of a process with Poisson statistics. Any measurement of a current with mean value $\langle I\rangle$ will be accompanied by intrinsic noise due to the random uncorrelated arrival times of the electrons that make up the current. This “shot noise” [37] has a power spectral density S_i given by

$$S_i(f) = 2q \langle I \rangle , \tag{3.10}$$

where the current power spectral density is expressed in units of A^2/Hz, and current amplitude spectral density in units of $A/\sqrt{Hz}$. Here the flat nature of the spectral density is a consequence of the current being composed of an uncorrelated sequence of delta functions whose Fourier transform is just a sum of constants from each delta function, totaling to the mean current . Thus according to Eq.(3.9), the current noise variance due to shot noise is

$$\sigma_i^2 = 2\, q \, \langle I \rangle \, \Delta f. \tag{3.11}$$

This gives the familiar result that the arrival times of electrons obey Poisson statistics: specifically that $\mathrm{Var}(I) \propto \langle I \rangle$.

Johnson-Nyquist Noise

The second fundamental broadband white noise source is Johnson-Nyquist noise, which arrises from the thermal diffusion of charge carriers in conductors. All resistive elements of the circuitry will exhibit this form of white noise. Instantaneous charge imbalances manfiest as random voltage fluctuations with a power spectral density given by Nyquist’s theorem [38]:

$$S_v(f) = 4\, k_B \, T \, R, \tag{3.12}$$

where T is the equilibrium temperature, R the resistance, and voltage power spectral density expressed in units of V^2/Hz, and voltage amplitude spectral density in units of $V/\sqrt{Hz}$. Here the flat nature of the noise spectrum is a consequence of treating the intrinsic electromagnetic oscillations in a resistor as black body radiation in which distributes an equal energy content of $\epsilon(f) = k_B T$ for each frequency degree of freedom in the limit where $f \ll k_B T/h$, valid for any sub-THz electronics . Thus according to Eq. (3.9), the voltage noise variance due to thermal noise is

$$\sigma_v^2 = 4k_B T R \Delta f. \tag{3.13}$$

3.3.4 Noise in a circuit with gain

A typical amplification stage of a circuit can be divided into an input and an output (Fig. 3.4), such that all noise sources at the input have a noise power spectral density $S_{in}^k(f)$. The circuit will transfer the input noise to the output via a transfer function $H_k(f)$, which may differ for each source k, such that the output noise power $S_{out}^k(f)$ is

$$S_{out}^k = H_k \cdot S_{in}^k, \tag{3.14}$$

where it is understood that each variable is a function of frequency f. Given an input signal and an amplification stage with signal transfer function H_s, it is extremely important to be able to compare the signal to the noise to determine the signal to noise ratio, and thus the limit of detection of the circuit. By defining an effective noise power spectral density referred to the signal input S'_{in} we can directly compare

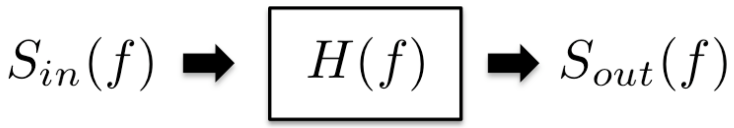

Figure 3.4: Input noise $S_{in}(f)$ is transferred to the output by a transfer function $H(f)$ to give an output noise power spectral density $S_{out}(f)$

the two. To do this, first each noise source is transfered to the output via Eq. (3.14), and then transfered back to the input by H_s such that

$$S_{in}^{k\,\prime}(f) = S_{in}^{k}\frac{H_k}{H_s}. \tag{3.15}$$

This noise spectrum is called the *input referred noise*, and is the noise power spectrum that would have to be present at the signal input such that a noiseless version of the amplifier would exhibit an equivalent output noise spectrum as the noise source k.

The total input referred noise power spectrum is a sum over all the noise sources such that

$$S_{in}' = \sum_k S_{in}^{k\,\prime}. \tag{3.16}$$

Since each source of noise can also be represented by its noise amplitude spectral density $s_k = \sqrt{S_k}$, the total input referred noise amplitude spectral density s_{in}' is

$$s_{in}' = \sqrt{S_{in}'} = \sqrt{\sum_k \left(s_{in}^{k\,\prime}\right)^2}. \tag{3.17}$$

Thus, amplitude noise is always added in quadrature. Finally, using (3.8) we find the total input referred noise variance in time, within a measurement bandwidth $\Delta f = f2 - f1$, is

$$\sigma_{in}^2 = \int_{f_1}^{f_2} S_{in}'(f)df = \sum_k \int_{f_1}^{f_2} S_{in}^{k}\frac{H_k}{H_s}df \tag{3.18}$$

$$= \sum_k (\sigma_{in}^{k\,\prime})^2, \tag{3.19}$$

where the input referred variance $(\sigma_{in}^{k\,\prime})^2$ due to each noise source is

$$(\sigma_{in}^{k\,\prime})^2 = \int_{f_1}^{f_2} S_{in}^{k}\frac{H_k}{H_s}df. \tag{3.20}$$

Thus it is seen that all noise powers densities and time variances are always added linearly, and noise amplitude densities and standard deviations added in quadrature.

Finally, the signal to noise ratio (SNR) for an input signal with amplitude s_0 is then defined as

$$SNR = \frac{s_0}{\sigma_{in}}. \tag{3.21}$$

Since the noise is white, the noise amplitude will have a gaussian distribution of values in time. The limit of detection (LOD) of a system is thus typically defined by SNR = 3, because 99% of the noise amplitude values will lie within three standard deviations of the mean noise level [28] . For a circuit where the input signal is a current, the input current limit of detection (I_{LOD}) is thus

$$I_{LOD} \equiv 3\,\sigma_{in}. \tag{3.22}$$

3.3.5 Choosing a photodiode operating mode

Both the photoconductive and photovoltaic operating modes of the photodiode offer linear current measurements with high sensitivity. To choose the appropriate mode it is necessary to understand the noise contributions in a photodiode. The full photodiode noise model is shown in Fig. 3.5. The full model includes the finite shunt resistance R_{sh} of the diode junction, as well as the finite capacitance of the junction's depletion region C_j. This model captures a photodiode's two fundamental noise sources: Johnson noise associated with the shunt resistance of the diode junction, and shot noise associated from both the dark current and photogenerated current. To compare with signal current, the johnson noise $v_{sh} = \sqrt{4k_BTR_{sh}\Delta f}$ of the shunt resistance can be modeled as a norton equivalent current source with $i_{sh} = v_{sh}/R_{sh}$

such that

$$i_{sh} = \sqrt{\frac{4k_B T \Delta f}{R_{sh}}}, \tag{3.23}$$

and the shot noise of the photogenerated and dark currents by $i_p = 2q \langle I_p \rangle \Delta f$ and $i_d = 2q \langle I_d \rangle \Delta f$. The shot noise from the photogenerated current is fundamentally unavoidable, however the other two noise sources can be controlled. Thus it becomes clear that for maximum sensitivity it is preferable to have a very high shunt resistance to decrease the Johnson current noise while minimizing the non-signal shot noise arising from dark current. By eliminated any reverse bias, we remove the dark current contribution to the noise. This suggests that staying in the photovoltaic mode where $I_d = 0$ is optimal and is the right choice for our transducer.

The downside of the photovoltaic mode however, is its slower speed: reverse biasing a diode increases its depletion region and reduces junction capacitance which increases the speed at which the diode can respond to external stimulation, such as a photogenerated current. However, this is only necessary to achieve signal rise-times $\tau \ll 1$ μs, and since we aim to operate at frequencies lower than 1 kHz, the speed advantage of the photoconductive mode is unnecessary.

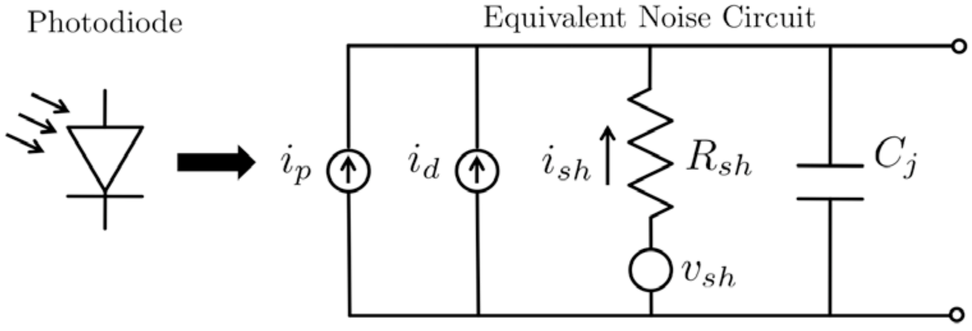

Figure 3.5: caption

While it is is possible to achieve both high speed and high sensitivity by using a specially designed avalanche photodiode, the necessary reverse bias voltages of $\approx$ 100 V are prohibitive in a miniature battery powered device.

3.4 Current-to-Voltage Conversion

3.4.1 Overview

The size and untethered nature of the capsular biosensor platform presents a trade off with circuit complexity and signal quality. While we can easily optimize signal to noise ratio using complex active circuitry, the size and power constraints of the device limit the circuit design to the simplest possible current-to-voltage conversion using the least amount of components. In this section we design a current-to-voltage converter, analyze its performance, and compute its noise behavior.

3.4.2 Methods of I-to-V Conversion

We have seen previously that a photodiode can be modelled as a parallel combination of an incident light power controlled current source and a diode. The photodiode signal is in the form of a current, however the signal sampling by the ADC can only read a voltage, thus we need a current-to-voltage converter. The simplest way to convert current into voltage is to dissipate the current directly through a load resistor and measure the voltage developed across the resistor (Fig. 3.6a).

(a) Nonlinear Output

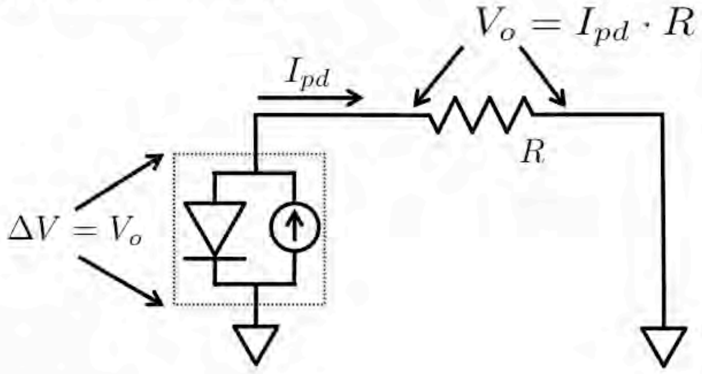

(b) Linear Output

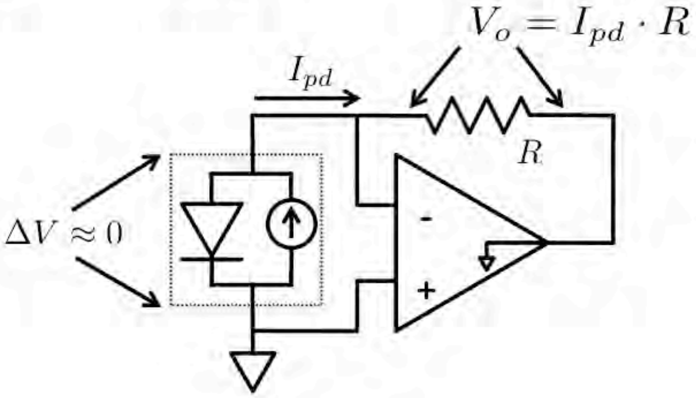

Figure 3.6: (a) Direct conversion: Output voltage forward biases the diode resulting in nonlinear behavior. (b) Active negative feedback: diode voltage is removed with op-amp leading allowing a linear measurement

This voltage in turn will forward bias the diode and Eq. (3.3) shows that the measured voltage will be a nonlinear function of the photogenerated current. Since we wish to make a linear transducer, we can solve this problem by using negative feedback to remove this voltage from the photodiode, effectively buffering the diode voltage from the output voltage. Adding an op-amp to the circuit as shown in Fig. 3.6b, we see that the op-amp fixes the diode voltage drop at a very small value $\Delta V = V_0/G_{OL} \approx 0$

where $G_{OL} \gg 1$ is the open loop gain of the op-amp. The photocurrent is then free to pass through the feedback resistor to generate an output voltage that does not effect the photodiode's operation such that

$$V_o = I_{pd}R = I_{photo}R. \tag{3.24}$$

The photodiode here is being used in its photovoltaic mode where there is no dark current, thus eliminating a noise source. This method of current-to-voltage conversion is called a transimpedance amplifier (TIA).

3.4.3 Modeling the TIA Transfer Function

Since the voltage across the photodiode has been eliminated, we can also remove the diode from the small signal model. The transfer function of an ideal TIA is given by Eq. (3.24), however, a real op-amp has finite input capacitances, the feedback resistance will invariably experience some parasitic capacitance, and our simplified photodiode model did not account for the diode's intrinsic shunt resistance R_{sh} and junction capacitance C_j [32]. Furthermore, a real op-amp has a finite bandwidth with open loop gain $G_{OL}(f)$. The frequency dependance of the op-amp gain, as well as input and feedback impedances will significantly effect the behavior of the circuit transfer function and a model (Fig. 3.7) including all these elements is needed to accurately characterize the TIA.

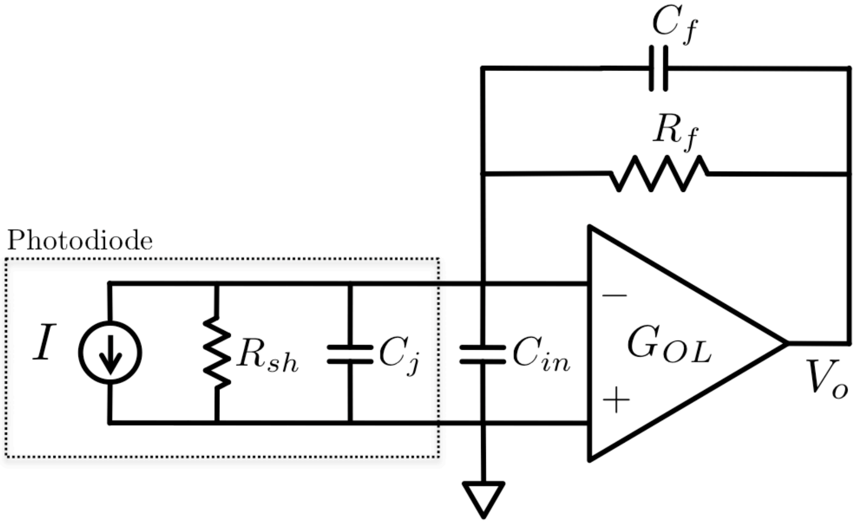

Figure 3.7: Full TIA small signal model. The photodiode is modeled as a current source with a shunt resistance and junction capacitance. The op-amp has finite input and feedback capacitance

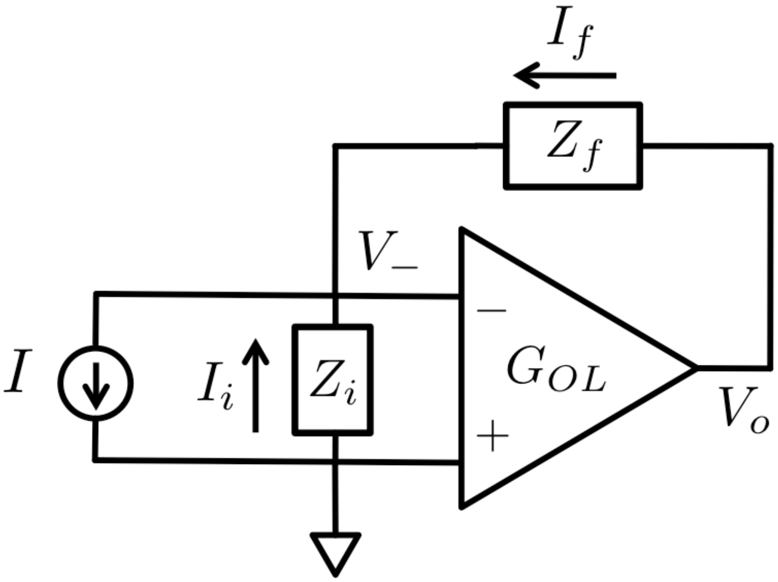

Figure 3.8: TIA lumped circuit model

For simplicity, we can lump (Fig. 3.8) all the input impedances together in $Z_i = R_{sh}||(i2\pi f C_i)^{-1}$, where $C_i = C_j + C_{in}$, and feedback impedances to $Z_f = R_f||(i2\pi f C_f)^{-1}$. Now we can find the circuit closed loop gain. First we note that conservation of charge dictates that the input current must be split into two currents I_f and I_i such that

$$I = I_f + I_i. \tag{3.25}$$

From inspection, the currents in each arm of the circuit are

$$\begin{aligned} I_f &= \frac{V_- - V_o}{Z_f} & (3.26) \\ I_i &= \frac{V_-}{Z_f}. & (3.27) \end{aligned}$$

Finally, by definition, the output voltage of the op-amp is the open loop gain of the voltage difference between the op-amps inputs

$$V_o = G_{OL}\left(V_+ - V_-\right) = -G_{OL} V_-. \tag{3.28}$$

Thus the closed loop current gain of the system or current transfer function $H_i(f)$ can be shown to be

$$H_i = \frac{V_0}{I} = -\gamma\, Z_f, \tag{3.29}$$

where

$$\gamma = \left(1 + \frac{1}{\beta\, G_{OL}}\right)^{-1}, \tag{3.30}$$

and

$$\beta = \frac{Z_i}{Z_i + Z_f}, \tag{3.31}$$

and $\gamma = \gamma(f)$, $\beta = \beta(f)$, and $G_{OL} = G_{OL}(f)$, are each a function of frequency. Inspection of Eq. (3.30) shows that for the lower input frequencies at which $G_{OL} \gg 1$

we will have $\gamma = 1$, and the transfer function reduces to the ideal case of $V_o = -IZ_f$. For higher frequencies, the gain may be reduced, and therefore, we can interpret γ as the impact of the opamp's finite bandwidth on the gain. The factor β is reffered to as the circuit *feedback factor* [32] and corresponds to the fraction of the output voltage V_-^{fb} that is fed back to the op-amp negative input such that

$$V_-^{fb} = \beta V_0. \tag{3.32}$$

If there is an extra voltage source v_s at that inverting input, then the total voltage at the inverting input will be

$$V_- = v_s + V_-^{fb}, \tag{3.33}$$

and using Eq. (3.28) and Eq. (3.32) we find that the input voltage source v_s is transferred to the output by

$$H_v = -\frac{\gamma}{\beta}, \tag{3.34}$$

where $H_v = H_v(f)$ is the voltage transfer function of the TIA. Inspection of Eq. (3.34) shows that for the lower input frequencies at which $G_{OL} \gg 1$ the voltage transfer function $H_v \approx -1/\beta$.

3.4.4 TIA transfer function

To understand the dynamics of the TIA we first assume that $Z_f = R_f$ and that the open loop gain of an op-amp with a unity gain bandwidth f_g has a open loop gain spectrum with a single pole roleoff $G_{OL}(f) = -if_g/f$. Now we examine a Bode plot Fig. 3.9 of the current transfer function, voltage transfer function, and open loop gain.

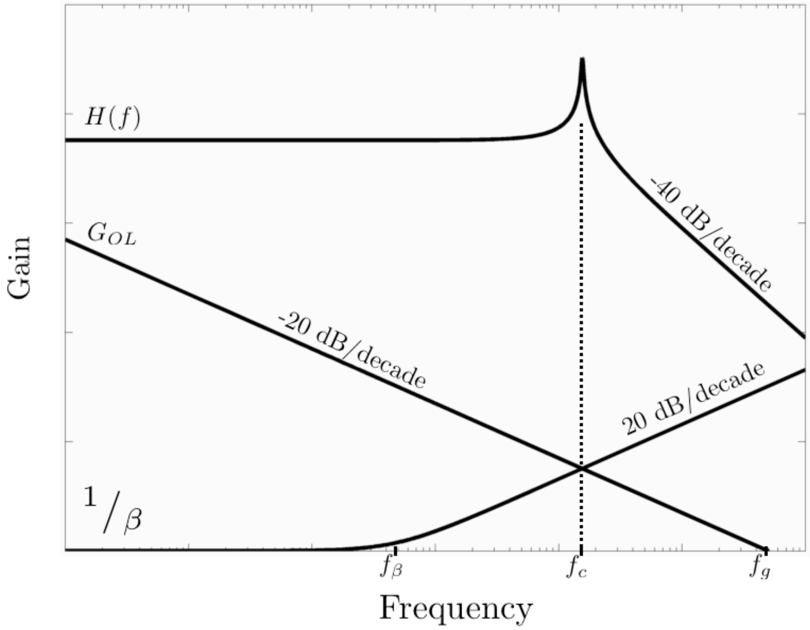

Figure 3.9: TIA frequency analysis. Shown in figure: log-log plot of current transfer function H_i, voltage transfer function H_v, and op-amp open loop gain G_{OL}. Circuit resonance occurs at f_c.

The plot shows that for low frequencies the current gain is constant and corresponds to the limit were $G_{OL} \gg 1$ and thus $|H| \approx Z_f$. The input capacitance looks like an infinite impedance and thus the voltage divider that defines β gives unity voltage gain. However, as the frequency of a voltage signal at the input increases beyond the pole frequency given by $f_\beta = (2\pi R_f C_i)^{-1}$, the voltage divider begins to transfer voltage noise with an increasing gain. This puts increasing demand on G_{OL} to compensate, however G_{OL} is also rolling off with increasing frequency. The point at which the gain can no longer support the voltage feedback occurs at f_c where $1/\beta = G_{OL}$. At this point, a pair of complex conjugate poles create a resonance in the transfer function. For frequencies above f_c the lack of available gain rolls off the current transfer function.

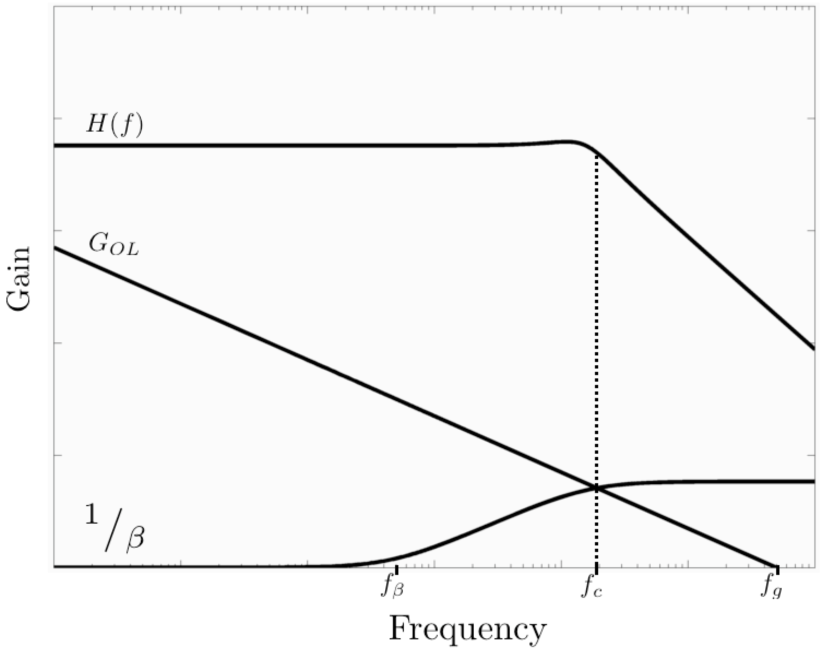

Figure 3.10: TIA frequency analysis with feedback capacitor. A feedback capacitor introduces a zero near the circuit resonance, effectively eliminating it.

The occurance of a circuit resonance is highly undesirable as it will often overwhelm signals. Thus we include a feedback capacitance (Fig. 3.10) to add a zero to to the transfer function. This zero levels off the voltage gain at or before f_c, and eliminates the resonance.

3.4.5 TIA noise

First we present the full noise model of the TIA (Fig. 3.11), which includes the photodiode's shot noise spectral density i_{pd}, op-amp input current noise i_{op}, op-amp input voltage noise v_{op}, and feedback resistor voltage noise v_f spectral densities. All noise sources here are functions of frequency f. The current noise will be transferred to the ouput via the TIA current transfer function H_i from Eq. (3.29), while the input voltage noise from the op-amp will be transfered via the voltage transfer function H_v from Eq. (3.34). The feedback resistor's noise adds directly to the output. Following

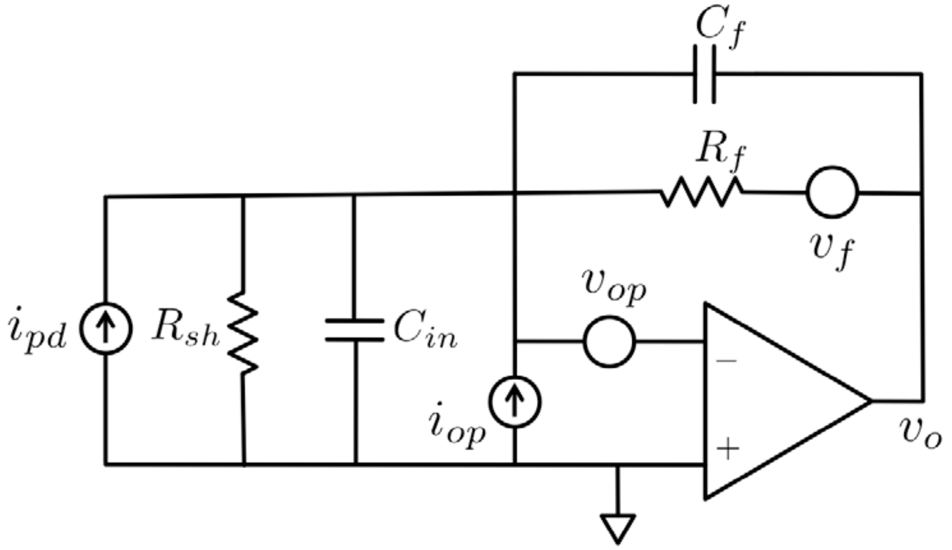

Figure 3.11: Full noise model of the TIA. Included sources: photodiode current noise i_{pd}, op-amp input current noise i_{op} and voltage noise v_{op}, and feedback resistor voltage noise v_f.

Eq. (3.15), the input referred current noise spectral density from each source is

$$\begin{aligned} i'_{pd} &= i_{pd} && (3.35) \\ i'_{op,i} &= i_{op} && (3.36) \\ i'_{op,v} &= v_{op}\left(\frac{H_v}{H_i}\right) = v_{op}\left(\beta\, Z_f\right)^{-1} && (3.37) \\ &= v_{op}\left(Z_i || Z_f\right)^{-1} && (3.38) \\ i'_f &= v_f\left(\frac{1}{H_i}\right) = v_f\left(\gamma\, Z_f\right)^{-1}, && (3.39) \\ & && (3.40) \end{aligned}$$

and total input referred current noise spectral density is

$$i_N = \sqrt{(i_{pd})^2 + (i_{op,i})^2 + \left(i'_{op,v}\right)^2 + \left(v'_f\right)^2}. \quad (3.41)$$

3.5 Data acquisition and digital filtering

3.5.1 Overview

Once the optical signal is transduced and amplified, it will be sampled by an ADC to be digitized. The ADC will have a fixed sampling rate f_s and Nyquist frequency $f_n = f_s/2$. All input frequencies must be below the Nyquist frequency f_n to prevent aliasing. Assuming that the sampling quantization is much smaller than the input noise standard deviation, the digitized signal will also contain the ADC input noise spectrum. In this section we first show how to reduce the noise variance due to white noise by reducing the noise bandwidth through a moving average filter. Next we show a digital "lock-in" type technique to filter out any 1/f noise while narrowing the white noise bandwidth.

3.5.2 Noise

At this point, we wish to take a our measured data and convert it to a single number that reflects the amplitude of the measured signal. However, we also have 1/f and white noise that will distort this measurment. If we filter out the 1/f noise, we will also remove a DC signal, however for an AC signal we can implement a filter to narrow the measurement bandwidth to just around the signal, removing the 1/f noise for frequencies below the signal frequency, and removing the white noise for frequencies above the signal frequency.

Filtering White Noise

We first combat the high frequency white noise with a computationally simple low pass filter: signal averaging. A moving average filter smooths out data by suppressing changes in the signal on a time scale shorter than the averaging window. This is a basic finite impulse response (FIR) digital filter [39] and can be represented by its impulse response

$$a_N[n] = \frac{1}{N} \sum_{k=0}^{N-1} \delta[n-i]. \tag{3.42}$$

The amplitude transfer function can be found with a z-transform using $z = e^{i\omega}$, where $\omega = \pi f / f_n$ with frequency f and Nyquist frequency f_n:

$$|A_N(\omega)| = \left| \frac{1}{N} \sum_{k=0}^{N-1} e^{i\omega k} \right| = \frac{1}{N} \frac{\sin(N\omega/2)}{\sin(\omega/2)}. \tag{3.43}$$

This transfer function is shown in Fig. 3.12. In this formalism, the Nyquist frequency is now represented by $\omega_n = \pi$

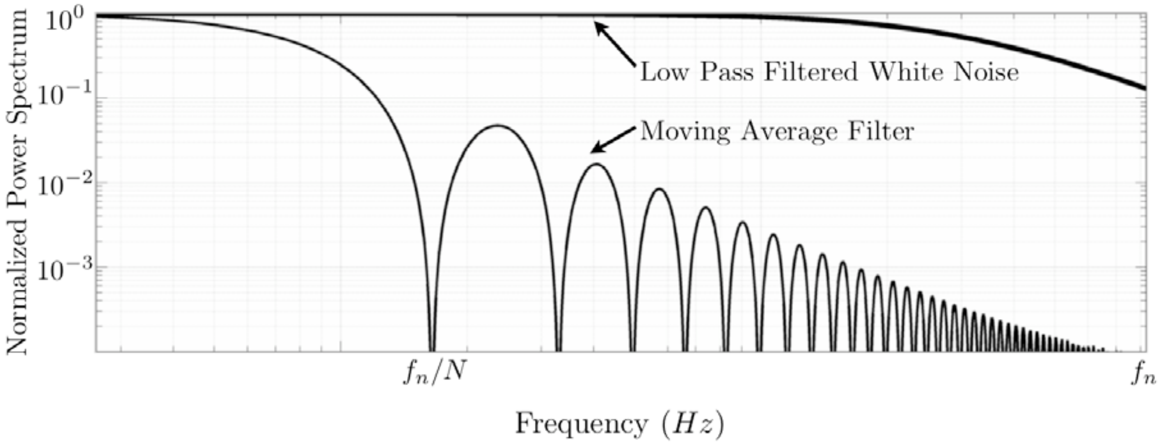

Figure 3.12: Transfer function for an N=50 point moving average filter. Also shown is white noise input into the moving average filter, which has been low pass filtered prior to averaging.

We will consider two cases, the first for white noise input (1), and the second for low pass filtered white noise (2).

1. If the input to the moving average filter is a noise spectrum that is white over the Nyquist band $\Delta\omega = \omega_n$, such that the noise power density is $S(\omega) = S_0$, then using Eq. (3.9), the input noise variance is

$$\left\langle v_1^2 \right\rangle_{in} = S_0\, \omega_n. \tag{3.44}$$

The effect of the filter when applied to this noise is then

$$\begin{aligned} \left\langle v_1^2 \right\rangle_{out} &= \int_0^{\pi} \left| A_N(\omega) \right|^2 \, S_0 \, d\omega = S_0 \int_0^{\pi} \left| \frac{1}{N} \frac{\sin\left(N\omega/2\right)}{\sin\left(\omega/2\right)} \right|^2 d\omega & (3.45) \\ &= S_0 \frac{\omega_n}{N}. & (3.46) \end{aligned}$$

The moving average filter has reduced the bandwidth to $\Delta\omega = \omega_n/N$ and thus reduced the noise variance by an equivalent factor:

$$\frac{\langle v_1^2 \rangle_{out}}{\langle v_1^2 \rangle_{in}} = \frac{1}{N}. \tag{3.47}$$

2. If original input noise with power density $S(\omega) = S_0$ is first low pass filtered by a filter with transfer function $H_{LP}(\omega)$ before the moving average filter, this result will slightly differ. We assume that the low pass filter has an effective bandwidth ω_e defined by

$$\omega_e = \frac{1}{S(\omega)} \int_0^\infty H_{LP}(\omega)\, S(\omega) d\omega, \tag{3.48}$$

such that the filtered noise variance is

$$\left\langle v_2^2 \right\rangle_{in} = S_0\, \omega_e, \tag{3.49}$$

which is the new input to the moving average filter. Furthermore, we assume that $\omega_n/N \ll \omega_e < \omega_n$ (Fig. 3.12), which means that while the low pass filter keeps noise in the Nyquist band $\Delta\omega = \omega_n$, the noise power density in the moving average filter bandwidth $\Delta\omega = \omega_n/N$ is not effected by the first low pass filter and is still S_0. Thus, the output noise variance remains $\langle v_2^2 \rangle_{out} = S_0\, \omega_n/N$. The change in the noise variance due to the moving average filter is now

$$\frac{\langle v_2^2 \rangle_{out}}{\langle v_2^2 \rangle_{in}} = \frac{\omega_n/\omega_e}{N}. \tag{3.50}$$

This result is useful when comparing noise variances before and after the application of a moving average filter. The moving average filter always serves to reduce the measurement bandwidth by a factor N, but only reduces noise variance by a factor given by Eq. (3.50) for white noise that has been low pass filtered before signal averaging.

3.5.3 Filtering 1/f Noise

The simplest way of gauging the amount of fluoresence detected is to turn the LED on, take a single voltage reading from the ADC and shut the LED off. However, this DC measurement is highly susceptible to drift or 1/f frequency noise. To get rid of 1/f noise while passing the signal we use a digital filter technique shown in Fig. 3.13.

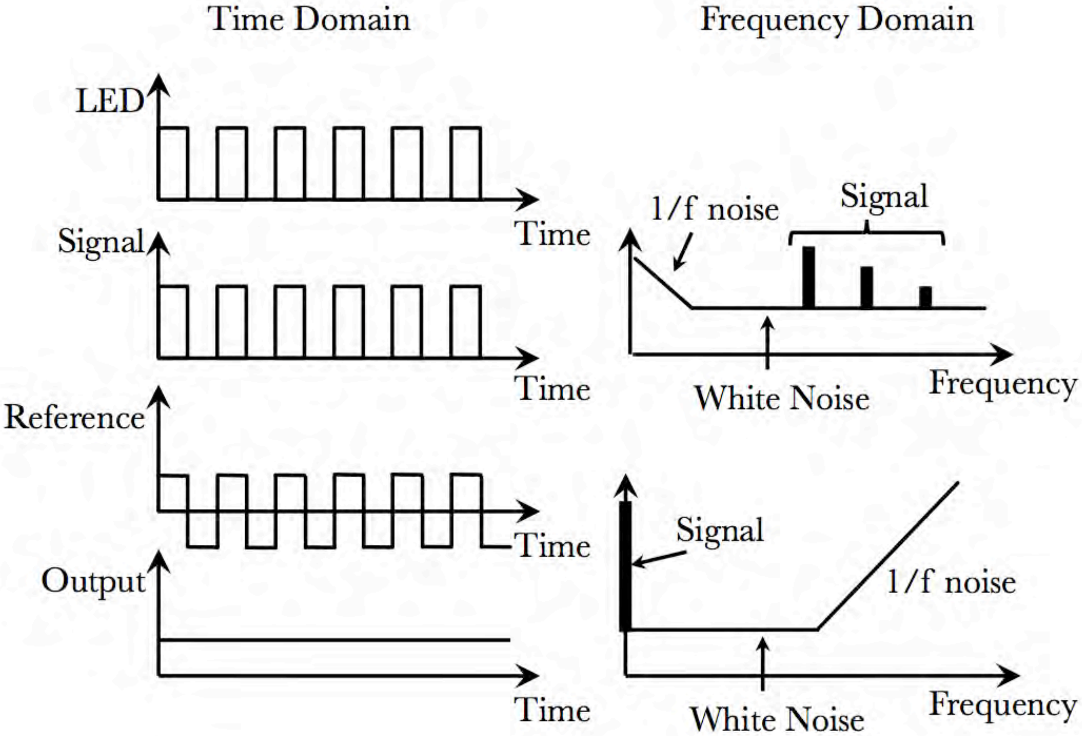

Figure 3.13: caption

We have shown that the moving average filter is excellent at filtering out AC white noise while passing a DC signal, and so we can employ a trick used in the "Lock-in Amplifier" technique to shift the signal frequency to DC for simple measurement, while simultaneously moving the 1/f content of the noise to higher frequencies so they along with the white noise will be successfully filtered by the low pass filter moving average filter. In Fig. 3.13 we show a pulsed LED signal in the time domain, and its corresponding measured pulsed signal. A reference unit square wave is with the same periodicity and phase as the measured signal (we can do this since the source of the signal is the same microcontroller) all the signal harmonics will shift to DC, thus being passed with unity gain through the moving average filter. Since multiplication by the reference does not effect the white noise spectral density, we can expect that the output noise of the digital filter will depend only on the input white noise at the signal frequency. Simultaneously, the 1/f noise is removed by the act of multiplying by the reference and then applying the moving average filter. The signal is passed with unity gain.

3.6 Input Referred Noise: The Detection Limit

The DSP technique presented in the previous section will effectively narrow the white noise bandwidth by a factor of N, while eliminating 1/f noise. Using Eq. (3.50), the reduced RMS noise fluctuation σ_{in}^N of the input referred current will be

$$\sigma_{in}^N = \sigma_{in}\sqrt{\frac{f_n/f_e}{N}}, \tag{3.51}$$

where σ_{in} is the initial input referred RMS noise fluctuation, and f_e is the effective bandwidth of the input referred current noise. Thus the input referred LOD is defined as

$$I_{LOD} \equiv 3\,\sigma_{in}^N. \tag{3.52}$$

3.7 Conclusion

In this chapter, we have described the photodiode as a transducer of an optical signal and modeled it as a circuit element. We have shown how to calculate the signal and noise transfer functions for a transimpedance amplifier and how to further decrease signal variance by using signal averaging after digital sampling. In Chapter Chapter 5 we will use this information to predict the behavior of the circuit designed to detect gastrointestinal bleeding.

Chapter 4

The Lab-in-a-Pill Hardware Platform

4.1 Introduction

The capsular biosensor can be divided into four discrete subsystems: sense, process, communicate, and power. The hardware related to each subsystem must be highly integrated to comply with the small size required of the capsular form factor, and the cost of the device needs to remain low to be of practical use. In the previous chapters we discussed the sensing portion of the biosensor. In this chapter we analyze the three remaining subsystems. We begin by discussing the protocol for wireless communication and develop the link budget requirements for transmission through the human body. Next we develop the software workflow necessary to process and communicate the data. Finally we conclude with a discussion of the power requirements of the device and derive expressions for the current consumption and total lifetime of a battery powering the device.

4.2 Body Sensor Networking

4.2.1 Overview

The burgeoning field of body sensor networks (BSN) concerns the formation of low power sensor networks that operate both locally inside and outside a patient's body to measure and communicate medical information. Furthermore, the BSN should have the capability to communicate via traditional wireless wide area network (WAN) and local area network (LAN) technologies such as Ethernet, WiFi, Bluetooth, or mobile phone networks (GPRS, CDMA, 3G, 4G, WiMax, *etc.*) to transmit collected medical data through the internet [17]. The most popular form of wireless communication with a device located inside the body is radio frequency (RF) telemetry [17]. Due to the remote environment of the body, it is difficult to supply power to an implanted device. Therefore, whatever the means of power supply, it is important to minimize power consumption in order to maximize the lifetime of the device. In RF telemetry, one of the primary forms of power consumption is the generation of the RF signal itself, and so a BSN typically uses an ultra-low power RF protocol for communicating to a local network node (monitor) located external to the body. These ultra-low power RF protocols may be specially designed for sensor networks and are not directly compatible with the more power hungry WAN technology used to communicate information over the internet. Thus an external monitor is necessary to function as a router between the BSN and the WAN. A proposed BSN for the endoscopic capsular biosensor is shown in Fig. 4.1. Once the capsular biosensor has aquired data, it transmits that data out of the body to an external monitoring device that is mounted immediately outside the body. The body functions as a lossy medium for RF signals (Section 4.2.5), and so to minimize the necessary power expenditure by the sensor, it is desirable that the external monitor be locally mounted with a wrist or arm band, pendant hanging from the neck, or belt clip, to remain physically close the capsular biosensor at all times. Once the data has been received by the external monitor through the BSN wireless protocol, it can be routed through a WAN connection through the hospital network and received by appropriate medical

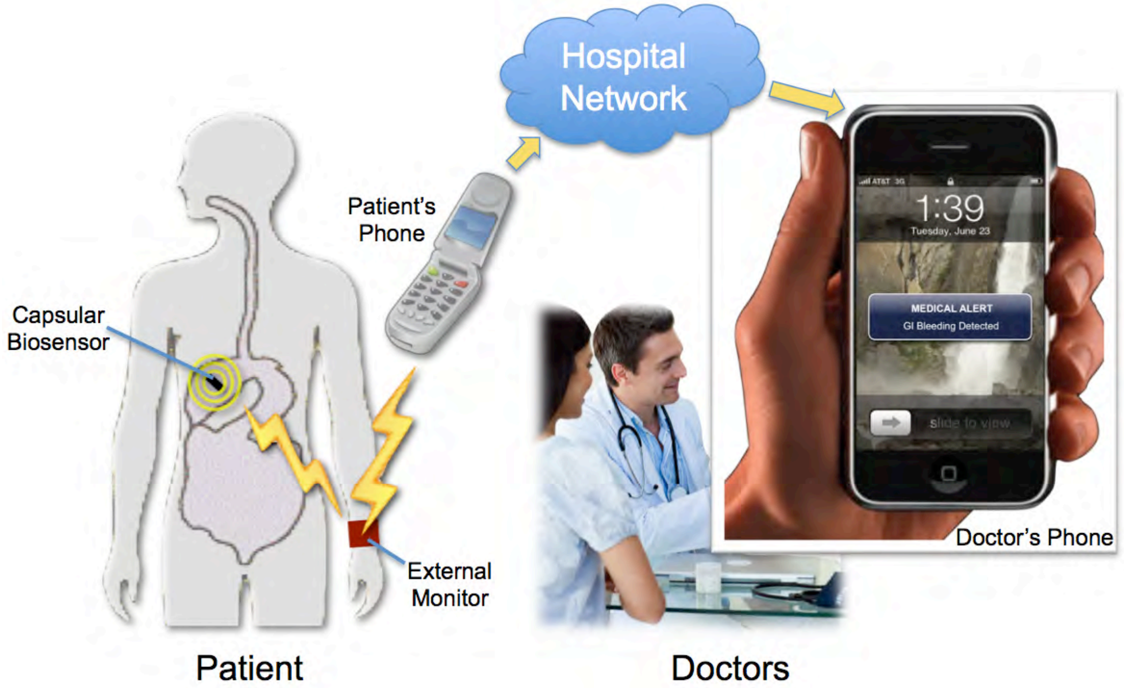

Figure 4.1: Body sensor network (BSN) for a swallowed capsular biosensor. The capsular sensor communicates through RF telemetry with an external monitor device, which forwards relevant information through an internet gateway device (e.g. mobile phone) to the hospital network so that doctors may receive the data or warnings on their device of choice (e.g. mobile phone).

personnel. Since the external monitor is not as constrained in size as the capsular biosensor, it can easily be supplied enough power to generate the appropriate signal strength to communicate with a WAN.

4.2.2 Wireless Networking

Currently, there many different RF standards that are potentially suitable for low power sensor networks, with most falling in the industrial, scientific and medical (ISM) band of frequencies which spans 6 MHz - 245 GHz [24]. To promote immediate clinical relevance of our capsular biosensor device, it is important the RF telemetry protocol is standardized to operate within existing hospital networks. Therefore, instead of developing a proprietary protocol for our device, we instead rely on a recognized IEEE standard for wireless networking so that our capsular biosensor can be easily integrated into an existing hospital sensor network.

The IEEE 802 working group is a family of standards that define hardware and software requirements for both wired and wireless local area networks (LAN and WLAN), wireless personal area networks (WPAN), and wireless metropolitan area networks (WMAN). The IEEE 802 standard is divided into the different groups each of which addresses a different kind of network [17]. The current groups and their subgroups are shown in Table 4.1.

Group	Description	Purpose	Implementation
802.3	LAN	Computer Networking	Ethernet
802.11	WLAN	Computer Networking	WiFi
802.15	WPAN	Low Power Networking	
802.15.1	Low Power PAN	Wire Replacement	Bluetooth
802.15.4	Low Power/Data-Rate PAN	Wireless Sensors	Zigbee
802.15.6	Body Area Network (BAN)	Medical Sensors	n/a
802.16	Broadband WMAN	Large scale WLAN	WiMax

Table 4.1: caption

The ideal network standard would combine low power wireless connectivity with the ability to easily function inside and outside the body. The 802.15.6 BAN standard is precisely designed for this, however it has not been finalized, and to our knowledge, no commercial devices exist that take advantage of this standard. The next best alternative is the 802.15.4 PAN standard. This is the most commonly used standard for wireless sensor networks. The emphasis of 802.15.4 is low cost, low power, and low data rate wireless sensor networks. The most popular implementation of the 802.15.4 standard is called Zigbee, which is a sophisticated networking and application layer build on top of the lower level 802.15.4 standard [17]. Traditionally, Zigbee has been implemented in industrial settings for automation and control, and wireless networks of remote sensors. It has also been used for “smart home” type applications wherein devices such as light switches, garage openers, temperature sensors, and remote controls are networked together to both collect information and automatically control a house environment [24]. Finally, this standard has also found use in medical sensor networks wherein body worn devices form a BSN to collect and transmit useful information. For example, the Harvard CodeBlue project [40] investigated the use of the Zigbee implementation of the 802.15.4 standard to create devices for "pre-hospital and in-hospital emergency care, disaster response, and stroke patient rehabilitation ... consisting of small, battery-powered 'motes' with limited computation and radio communication capabilities."[41]

Recently, the BSN community has begun exploring the use of the Zigbee communication standard to transmit data from implanted sensors [42]. It was been found that despite the large power losses an RF signal experiences while propagating through the body, the Zigbee standard is sufficient for communication between a device implanted deep in the gastrointestinal tract, and an external device worn up to two meters away [42].

The ubiquitous use of the Zigbee in industrial, medical, and home settings suggests that this is a robust and mature technology. Along with its proven ability to transmit information out of the body from an implanted sensor, this standard requires minimal development to be adapted to our application, making it an excellent choice for our BSN communication protocol.

4.2.3 IEEE 802.15.4 Overview

The IEEE 802.15.4 standard [17] is divided into two frequency bands with the U.S.: 902-928 MHz and 2400-2483.5 MHz. It supports 10-16 channels within its bandwidth of operation, and up to 250 kb/s date rates. The standard uses a direct-sequence spread spectrum modulation (DSSS) in which it pseudorandomly modulates the phase of encoded data much faster than the data rate to spread the power spectral density of the transmission into a wide bandwidth, effectively reducing the overall impact of interference, noise, or narrowband attenuation that may occur in narrower bands. On the receiver end, the inverse of the pseudorandom sequence is used to "de-spread" and extract the data from the received signal. This allows the Zigbee, bluetooth, and WiFi devices to coexist with the same 2.4-2.5 GHz band, as they all employ different modulation techniques.

Furthermore, the standard specifically calls for low power consumption by allowing the sensor device to spend most of the time in a low power sleep mode, only infrequently waking up to perform a measurement or communication. The radiated RF power is specified not to exceed 10 mW and the minimum received power by a 802.15.4 radio is -100 dBm (100 fW) in order to have a sufficiently bit error rate $\leq 1\%$. The instantaneous power consumption of a Zigbee radio is specified to be below 100 mW [17]. The required hardware to enable Zigbee networking in a device is an integrated circuit which implements the Zigbee protocol, a radio to encode the signal, and an antenna to transmit the signal.

The 802.15.4 standard emphases simple and quick network formation between devices, and its signal error correction is optimized for handling errors typically incurred

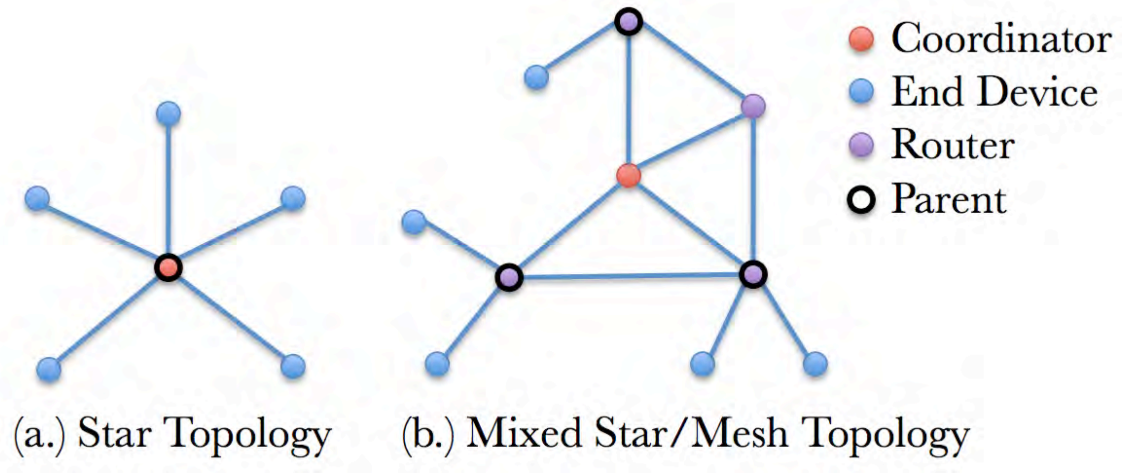

Figure 4.2: caption

by propagating through environments with large losses and multiple reflections. Furthermore, the network topology is optimized for the networking of many devices (Fig. 4.2). Zigbee nodes can be divided into the four (overlapping) groups according to the chosen function of the device, which is hardcoded into the device firmware.

- **Coordinator**: Each network requires a single node to function as a coordinator of the entire network.
- **Router**: Any node that does not sleep, but assists in transmitting information from one node to another.
- **End Device**: This device has all networking disabled except for direct communication with its parent node (which can be a router or coordinator). This allows for extremely low power consumption for devices that require it.
- **Parent**: Any node (router or coordinator) that is responsible for coordinating communication with an end device.

With these behaviors, the Zigbee network can arrange itself into arbitrary network topologies. The star topology is primarily used when a single network node coordinates many end devices. When end-devices are out of range of the coordinator, routers may be used to transmit the information down the network chain to make sure the data reaches the appropriate node. This degree of sophistication is beyond the needs of our BSN, and we exclusively use the star topology formed between a single implanted end-device (capsular biosensor), and a single parent coordinator (external monitor). However, we envision future device implementations to incorporate multiple capsular biosensors and external monitors in a single patient, and so the Zigbee protocol offers a practical solution to both our current and future BSN requirements.

4.2.4 Wireless Link Budget

To determine the strength of a wireless connection, it is important to determine the *link budget* between two nodes of a network. The link budget is one of the most important concepts in RF signal propagation: it is a way to mathematically connect the RF power output of one transceiver to the corresponding RF power reaching another radio tranceiver. The calculation begins with the electrical power used to drive the antenna, factors in all losses between the transmitting and receiving antenna, and determines the total theoretically possible received power. The transmitting and receiving antennas and supporting RF circuits must then be designed have enough transmission power and receiving sensitivity to reliably communicate RF data despite the the losses and attenuation.

The link budget in free space is calculated as follows: A transmitting device and a receiving device are separated by a distance R. The RF power P_t is input into the RF electronics, which have a fractional power loss L_e^T. The antenna will then radiate the signal into free space with an average fractional gain G_a^T relative to a hypothetical lossless isotropic antenna[1]. The total power radiated by the antenna is thus

$$S_a = \frac{P_t\, G_a}{L_e}. \tag{4.1}$$

The resulting radiated signal will propagate a distance R and be attenuated by $L_{FS} = (4\,\pi\, R^2)^{-1}$ by the time it reaches the receiver, due to the inverse square spreading of the electromagnetic energy. Finally, an ideal isotropic receiving antenna will present itself to the incident RF signal as an antenna effective area (aperture size) $A_e = {}^{\lambda^2}\!/_{4\,\pi}$ [17], where λ is the free space signal wavelength. Factoring in the receiving antenna gain G_a^R and the electronic power loss L_e^R, the total power reaching the receiver's radio is

$$P_r = P_t \left[\left(\frac{G_a^T}{L_e^T}\right) \left(\frac{G_a^R}{L_e^R}\right) \left(\frac{\lambda}{4\,\pi\, R}\right)^2 \right]. \tag{4.2}$$

This is the *Friss power transmission equation* [17]. When calculating gains and losses, it is typically easier to add small logarithmic values rather than multiply very large or small numbers, and so taking the base-10 logarithm of Eq. (4.2), we arrive at the link budget equation:

$$P_R = P_T + G_T + G_R - L_{FS} - L_E^T - L_E^T, \tag{4.3}$$

where $P_R = 10\,\log P_r/P_0$ (dBm) is the received power, $P_T = 10\,\log P_t/P_0$ (dBm) is the transmitted electrical power, $G_T = 10\,\log G_a^T$ (dBi) and $G_R = 10\,\log G_a^R$

---

[1] The antenna gain is the fraction of power radiated relative to the an ideal isotropically radiating antenna. For example, a half-wave dipole antenna has a fractional gain of $G_a = 1.5$ and a monopole antenna has a fractional gain $G_a = 3.18$ [17]

(dBi) are the transmitting antenna and receiving antenna gains relative to isotropic, $L_{FS} = 20 \log\left(\frac{\lambda}{4\pi R}\right)$ (dB) is the free space loss due to spherical spreading of the RF signal and receiving antenna aperture size, and $L_E^T = 10 \log L_e^T$ (dB) and $L_E^R = 10 \log L_e^R$ (dB) the RF circuit electrical loss. Also, $P_0 = 1$ mW, so that powers are measured in dBm, and all other terms in dB. With this formalism, it is very straightforward to add additional gains or losses to the link budget.

Return and Insertion Loss

The loss incurred in the RF circuitry L_E can be primarily attributed to signal absorption and reflection by components in the circuit path between the radio output and the antenna (insertion loss), as well as signal reflection at the antenna/air interface due to impedance mismatch (return loss).

The insertion loss L_I is defined as the amount of signal that remains after transmission through an inserted element in the electrical network [43]. We assume that L_I accounts for all components in the RF circuitry and is typically provided by the specifications of the individual electrical components.

The power of the reflected signal at the antenna air interface is given by the return loss R_L (dB), such that the total percentage of signal transmitted $T_{\%}$ after return loss is $T_{\%} = 1 - 10^{R_L/10}$. The logarithmic signal loss L_R (dB) due to antenna return loss is thus

$$L_R = 10 \log\left(T_{\%}\right) = 10 \log\left(1 - 10^{R_L/10}\right), \tag{4.4}$$

and the total loss due to RF electronics is

$$L_E = L_R + L_I. \tag{4.5}$$

4.2.5 *In Vivo* Telemetry

For IEEE 802.15.4 telemetry near or in the human body, the there will be an additional source of loss L_B subtracted from Eq. (4.8) due to absorbtion of the RF signal by the body. The 2.4 GHz band is strongly absorbed by human tissue, muscle, and fat content due to microwave heating, and multiply reflected at tissue boundaries, which adversely effects the RF signal propagation [17]. While the 802.15.4 protocol is optimized for free space telemetry and is not officially specified for use in BSN, the high receive sensitivity and robust error correction algorithms of Zigbee radios are capable of working in the human body despite the signal degradation. The geometry of the telemetry link is shown in Fig. 4.3.

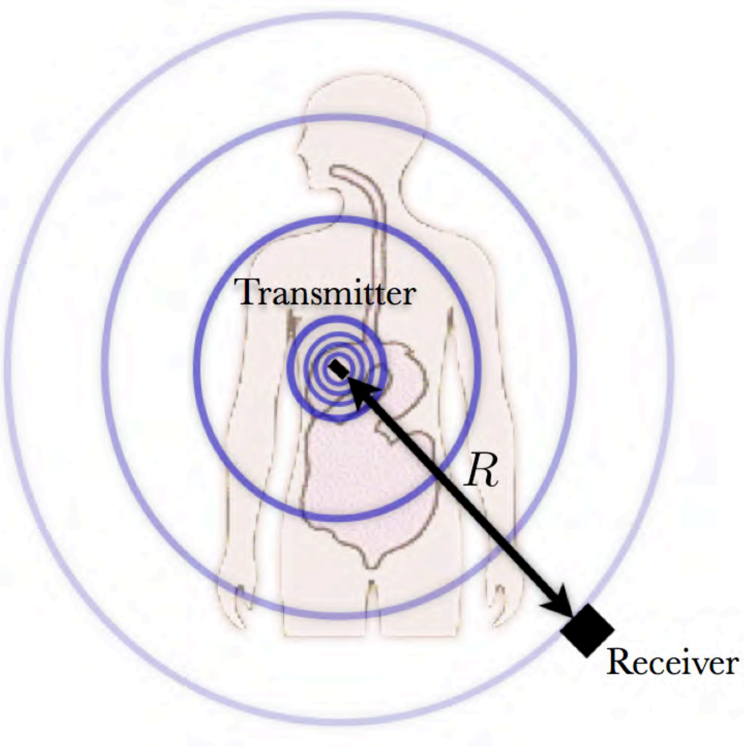

Figure 4.3: Transmission of an RF signal in the human body. Sensor device (transmitter) in the stomach is a distance R away from an external monitor (receiver)

Due to the human bodys heterogeneity, it is difficult to make accurate predictions of the RF propagation from an implanted sensor to an external monitor. The dielectric constant has a large variation, from $\epsilon = 12$ for fat, to $\epsilon = 62$ for the stomach walls, and the conductivity varies from $\sigma = 0.82\ \Omega^{-1}\, m^{-1}$ for fat, to $\sigma = 2.56\ \Omega^{-1}\, m^{-1}$ for muscle. Furthermore, due to impedance mismatch between different tissues, the signal loss due to reflection at a single interface can be as large as - 1.8 dB (muscle/fat interface) inside the body, and - 5.7 dB at the skin/air interface [17]. Despite these large variations, it has been found that the overall RF penetration depth in the body for tissues surrounding the stomach (stomach wall, muscle, fat, skin) can be estimated to be $l_s \approx 0.75$ cm at 2.4 GHz for a typical adult male [17]. If we assume a typical distance $d_s = 7$ cm from the inside of the stomach to the skin surface, the attenuation due will be

$$L_B = 10 \log_{10} \left(e^{-d_s/l_s} \right) \approx 40 \text{ dB}. \tag{4.6}$$

The body induced propagation loss L_B is a consequence of both the absorption of the signal by tissue, muscle, and fat, as well as signal reflections from impedance mismatches at the boundaries [17].

Free Space Loss and Total Link Budget

For a receiver placed at a distance R = 30 cm away from the transmitter, and for $\lambda = c \cdot (2.4 \text{ GHz})^{-1} = 12.5$ cm in free space, the total free space loss is

$$L_{FS}\,(30 \text{ cm}) = 30 \text{ dB}. \tag{4.7}$$

If we assume that the transmitter and receiver contain identical RF hardware, then the total link budget equation including loss due to body absorption is

$$P_R = P_T + 2\,G_A - L_E - 70 \text{ dB}, \tag{4.8}$$

In Chapter 6 we will use this relationship to calculate the link budget for our capsular biosensor and an external monitor with identical RF hardware.

4.3 Software

To connect the sensing portion of the device with wireless data transmission via Zigbee, a microcontroller (μC) is needed. A low power μC with an onboard ADC is used to fill this role. The μC needs custom software in order to direct the flow of information from the sensor to the external monitor device. We show the software workflow in Fig. 4.4 for the capsular biosensor. The software workflow is compatible with any μC that has an ADC and the capability to control a Zigbee radio.

First, the device is powered on and runs subroutines that initialize the hardware and the Zigbee protocol stack. Then, the device sends a sequence of messages to find a parent node and continues doing this until it finds a parent device. Once it has successfully joined the network, the device begins an internal timer that dictates how often to take a measurement. If it is not time to take a measurement, the device goes into a low power sleep mode. According to the Zigbee protocol, in order for a sleeping device to remain on the network, it must periodically wake up and send a brief message to confirm that it is still operational, referred to as *polling*. This serves as the device's heartbeat and allows for the external monitor device to always know if the capsular biosensor is functional, regardless of if it has taken a measurement or not. Once it confirms this, it checks whether it is time to take a measurement again. If so, it aquires and processes data as shown in Fig. 4.5

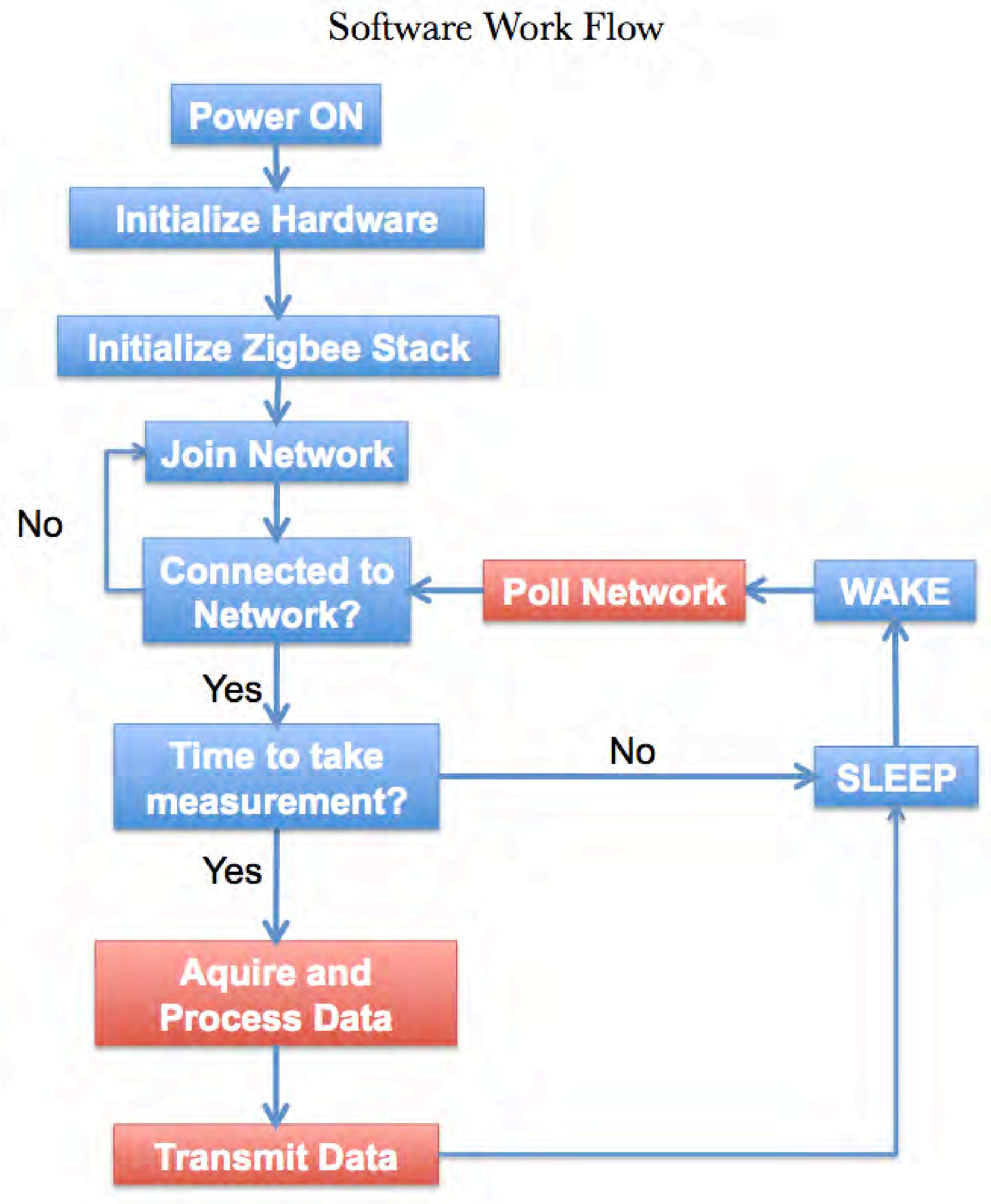

Figure 4.4: caption

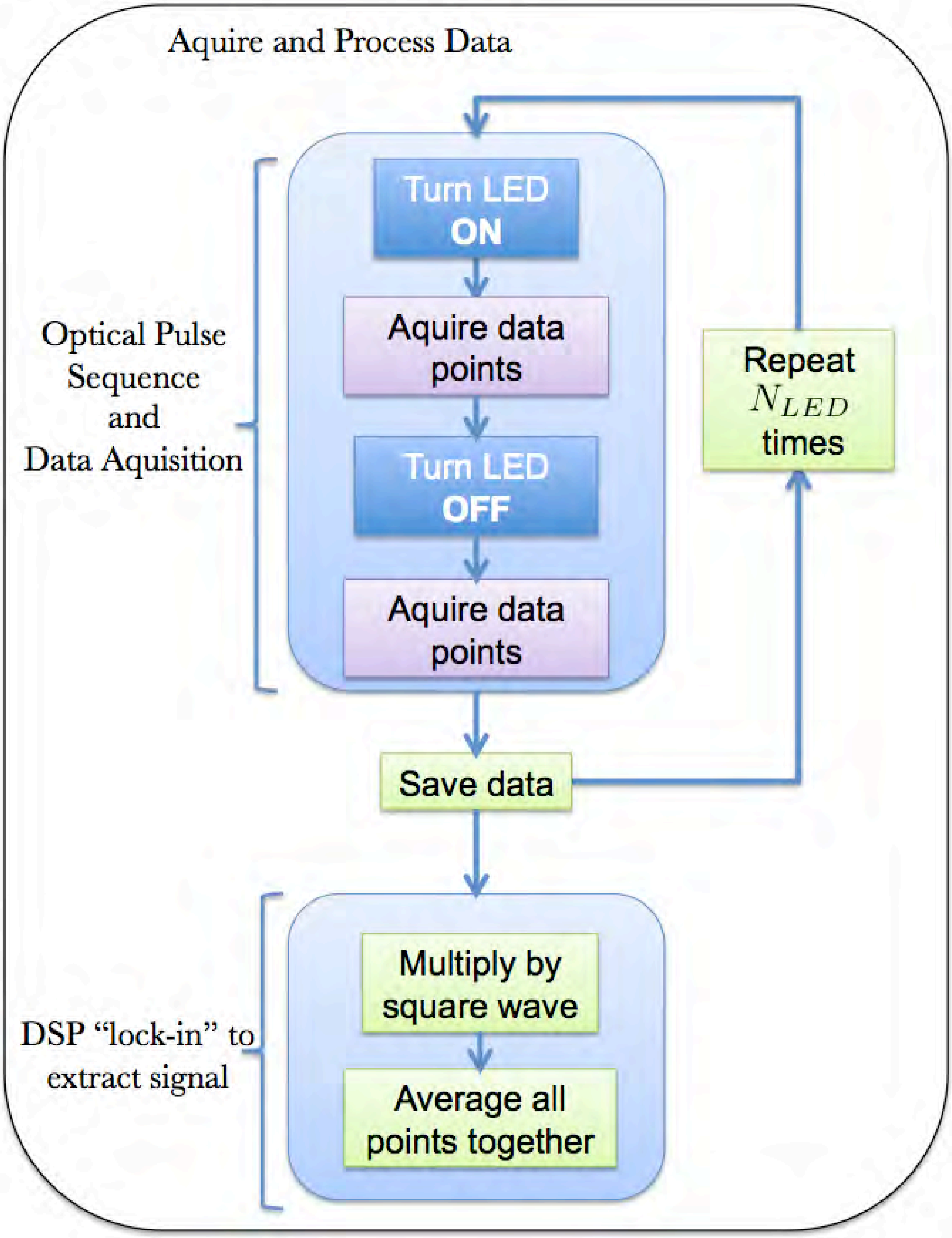

Figure 4.5: caption

The data acquisition sequence uses a logic signal to pulse the LED on and off N_{LED} times with a 50% duty cycle for a total time Δt_{PULSE}. During each cycle it simultaneously aquires voltage measurements (Chapter 3) at a sampling rate imposed by the specific choice for ADC. Finally after all the data is collected, it numerically multiplies the data by a square wave with the same frequency and phase as the LED pulses and averages all the points together. This is the digital "lock-in" filtering used to both narrow the measurement bandwidth to reduce noise, and extract the modulated signal so that it can be represented by a single number, the amplitude of the signal.

Finally, once the data is acquired, the single data value is sent to the external monitor by a single Zigbee data packet. The external monitor is then free to forward the data through the hospital network to the medical personal monitoring the patient. Following the transmission of data, the device immediately powers down into its low power sleep mode. After a pre-determined time, it wakes up to poll the network, and continues this sequence.

4.4 Power Consumption

4.4.1 Overview

One of the greatest challenges to miniaturizing an untethered device is the inherent difficulty in delivering enough usable energy to the device for it to function for a useful period of time. As such, the energy consumption of each subsystem needs to be carefully analyzed to determine the operational lifetime of the device. We use a battery to power the device (discussed in in Section 6.5.1). Typically, battery lifetimes are quoted in terms of the amount of stored charge (in units of mA·hours) that can contribute to a useful current. Each system process - powering an LED, a μC, or radio - consumes a fixed current while operational. However, because the device spends most of its time in an ultra-low-current sleep mode, the system processes will operate in discrete stages with each stage consuming a fixed amount of charge each time. By knowing the frequency with which each stage occurs, we can find the average current consumed by each stage, and finally, the total demands on the battery supply. It is most useful to compare dissipation characteristics across electronic subsystems using the language of charge and current. In this section, we examine the current demand of each subsystem of the device and derive expressions for both the amount of charge consumed during each stage of the device operation, as well as the total average current demand.

4.4.2 Sources of Current Consumption

There are three primary sources of current consumption in the device: the LED, μC, radio. The μC always consumes a current $I_{\mu C}$ when the device is active, the radio consumes I_{RADIO} when the radio is in use, and the LED consumes I_{LED} when the LED is on. When none of these subsystems are active, the device by definition is in its sleep mode, which consumes a fixed quiescent current I_Q. All other components (voltage regulars, opamps, *etc.*) have negligible current drain compared these three primary systems in both wake and sleep modes.

The actual device operation while awake can be divided into discrete stages, such that during each stage the current consumption can be broken into the consumption due to the CPU, and the relevant subsystem. During each active stage n, the μC is active for a time Δt_n, draining $I_{\mu C}$, and a single subsystem (LED or radio) is active for part of that time Δt_n^S, draining its current I_S (I_{LED} or I_{RADIO}). The total charge Q_n consumed during a single iteration of each active stage is thus

$$Q_n = I_{\mu C} \cdot \Delta t_n + I_S \cdot \Delta t_n^S. \tag{4.9}$$

During the device operation, each active stage will occur with a frequency f_n and so the average current I_n consumed due to each stage is

$$\langle I_n \rangle = Q_n \cdot f_n. \tag{4.10}$$

4.4.3 Total Current Consumption and Battery Lifetime

Since each stage is non-overlapping, the fraction of time the device is awake is $\sum_n \Delta t_n \cdot f_n$, and thus the average current consumed while sleeping is

$$\langle I_{SLEEP} \rangle = I_Q \left(1 - \sum_n \Delta t_n \cdot f_n \right). \tag{4.11}$$

Adding this to the active current we find that the total average current consumed by the device is

$$\langle I_{TOT} \rangle = \sum_n \langle I_n \rangle + \langle I_{SLEEP} \rangle . \tag{4.12}$$

Finally, for a battery with a total capacity Q_{BATT} measured in mA·hours, the total operational lifetime of the device is

$$\Delta t_{LIFE} = \frac{Q_{BATT}}{\langle I_{TOT} \rangle}. \tag{4.13}$$

This is the total amount of time that the device can operate for before the battery can no longer supply current to the device.

4.4.4 Stages of Charge Consumption

There are three discrete stages of operation of the Zigbee-based capsular biosensor: data acquisition (DAQ), data transmission (TX), and network polling (Poll) [44]. We first calculate the total charge consumed at by each stage.

Data Acquisition

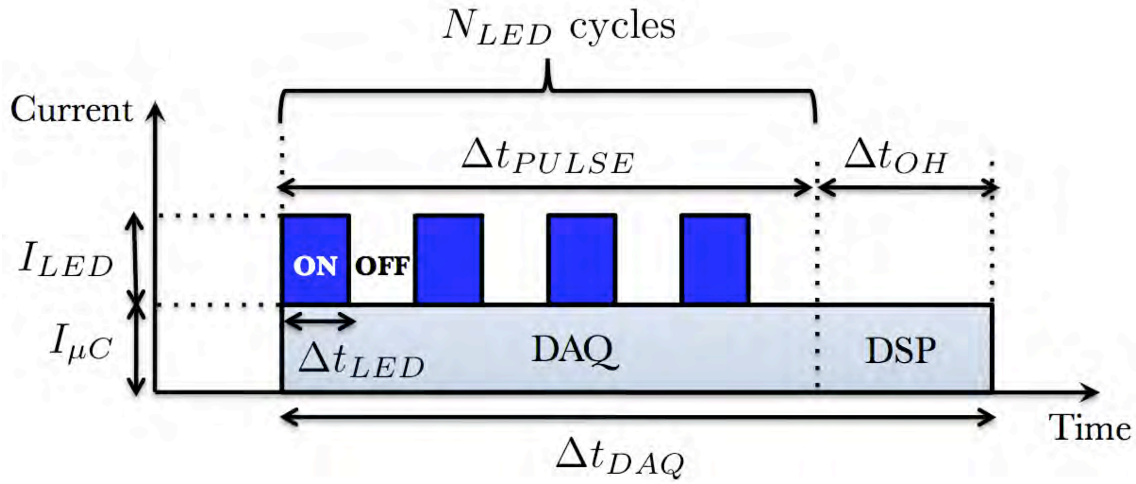

Figure 4.6: caption

The current drain during the data acquisition stage is shown in Fig. 4.6. This stage is completely general to any μC running the capsular biosensor application. The data acquisition stage takes a total time

$$\Delta t_{DAQ} = \Delta t_{PULSE} + \Delta t_{OH}, \tag{4.14}$$

where Δt_{PULSE} is the total time that the pulse sequence takes, and Δt_{OH} is the time required to initiate the sequence, perform the DSP to filter the data, compute the value of the signal, and package the data for sending. During the detection pulse sequence, the LED will pulse on and off N_{LED} times with a 50% duty cycle such that the time the LED is on is Δt_{LED} with each period lasting a time $2\Delta t_{LED}$. Thus, the total time the pulse sequence takes is $\Delta t_{PULSE} = 2N_{LED} \cdot \Delta t_{LED}$. Finally, the total charge consumption Q_{DAQ} of the data acquisition stage following Eq. (4.9) is

$$\begin{aligned} Q_{DAQ} &= I_{\mu C} \cdot \Delta t_{DAQ} + I_{LED} \cdot \Delta t_{PULSE}/2 && (4.15) \\ &= I_{\mu C} \left(2N_{LED} \cdot \Delta t_{LED} + \Delta t_{OH}\right) + I_{LED} \cdot N_{LED} \cdot \Delta t_{LED}. && (4.16) \end{aligned}$$

4.4.5 Data Transmission

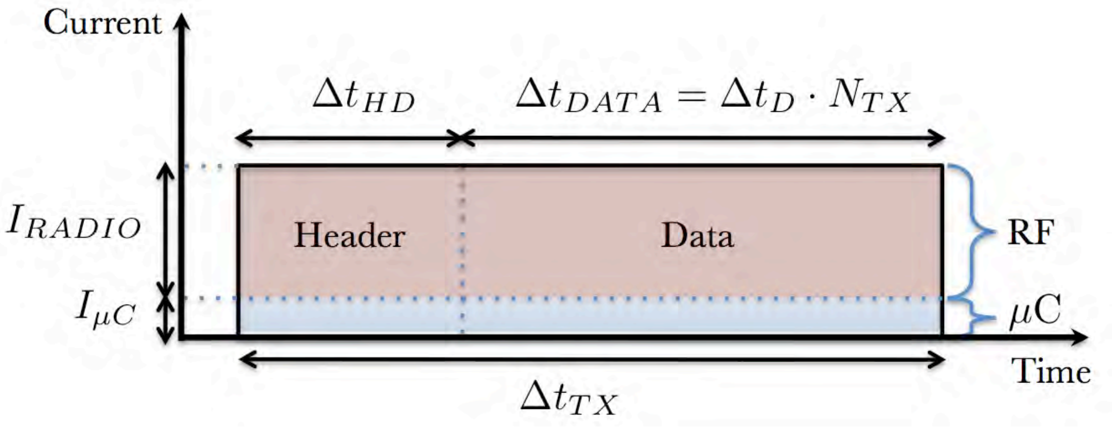

Figure 4.7: caption

The current drain during the data transmission stage for a Zigbee radio is shown in Fig. 4.7. The sensor node transmits a single data packet which consists of a header with the relevant packet routing information followed by the data buffer. The data transmission stage takes a total time $\Delta t_{TX} = \Delta t_{HD} + \Delta t_{DATA}$, where Δt_{HD} is the time it takes to transmit the packet header, and Δt_{DATA} is the time to transmit the data payload. The data is encoded as an array of bytes (8 bits each). All data we will be transmitting will consist of 16-bit integers (2 bytes), with each number taking a time Δt_D to transmit. If there are N_{TX} 16-bit integers in the data payload to be transmitted, then $\Delta t_{DATA} = N_{TX} \cdot \Delta t_D$. Finally, from Eq. (4.9), the total consumed charged Q_{TX} in the data report stage is

$$\begin{aligned} Q_{TX} &= I_{\mu C} \cdot \Delta t_{TX} + I_{RADIO} \cdot \Delta t_{TX} \qquad (4.17) \\ &= \left(I_{\mu C} + I_{RADIO}\right)\left(\Delta t_{HD} + N_{TX} \cdot \Delta t_D\right). \qquad (4.18) \end{aligned}$$

4.4.6 Network Poll

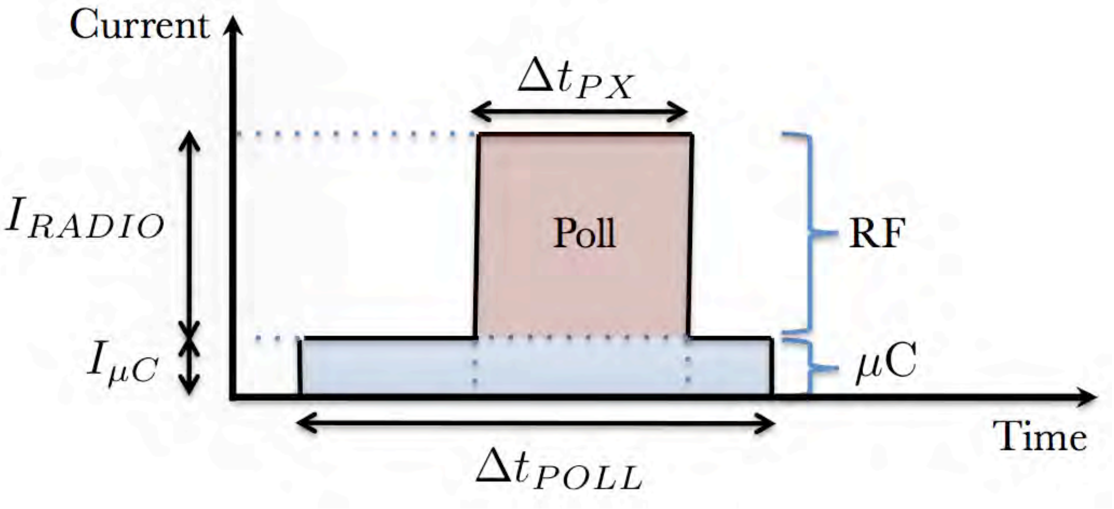

Figure 4.8: caption

The current drain during the network polling stage for a Zigbee radio is shown in Fig. 4.8. Periodic polling is a necessary and unavoidable part of being part of a Zigbee network, and happens every time the node wakes up from its sleep mode. The data poll packet is fixed in length and current consumption. The poll stage takes a total time Δt_{POLL}, with Δt_{PX} being the total time the radio is active for polling. Finally, from Eq. (4.9), the total consumed charged Q_{POLL} in the polling stage is

$$Q_{POLL} = I_{\mu C} \cdot \Delta t_{POLL} + I_{RADIO} \cdot \Delta t_{PX}. \qquad (4.19)$$

4.4.7 Total Current Consumption

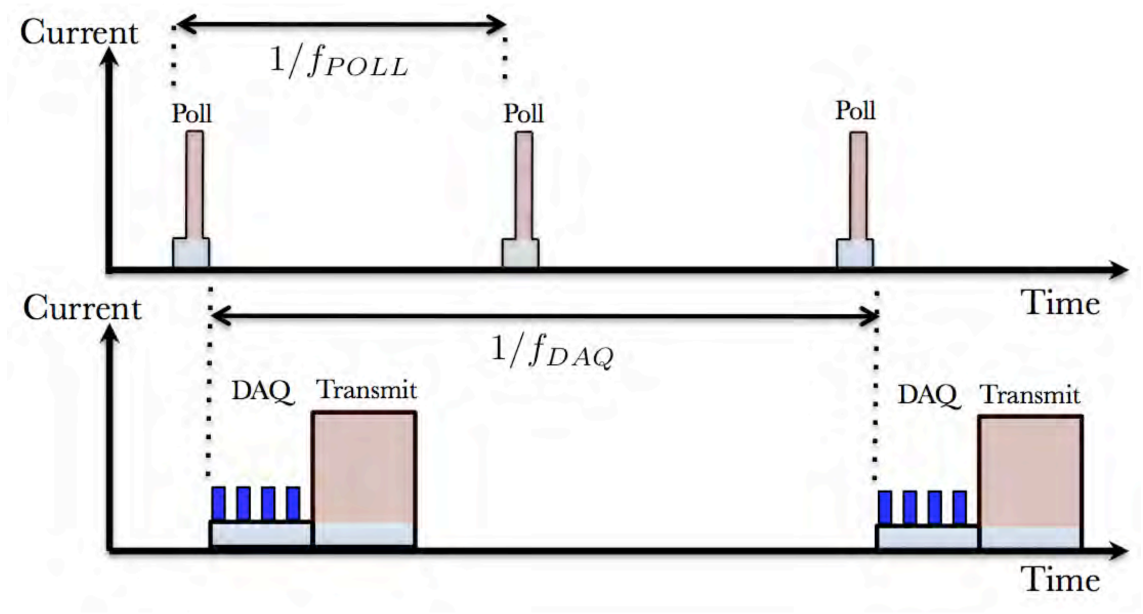

Figure 4.9: caption

The pulse sequence of the three operation stages are shown in Fig. 4.9. The rate at which data is acquired and transmitted is f_{DAQ} (data is always transmitted after a measurement). The device polling rate $f_{POLL} = N_P \cdot f_{DAQ}$ is an integer multiple N_D of the rate of data acquisition. Following Eq. (4.10), the total average current consumed by each stage is thus

$$\langle I_{DAQ} \rangle = Q_{DAQ} \cdot f_{DAQ} \tag{4.20}$$

$$\langle I_{TX} \rangle = Q_{TX} \cdot f_{DAQ} \tag{4.21}$$

$$\langle I_{POLL} \rangle = Q_{POLL} \cdot f_{DAQ} \cdot N_P \tag{4.22}$$

$$\langle I_{SLEEP} \rangle = I_Q \left[1 - (\Delta t_{DAQ} + \Delta t_{TX} + N_P \cdot \Delta t_{POLL}) \, f_{DAQ} \right]. \tag{4.23}$$

We will use these results when designing the lab-in-a-pill hardware platform our capsular biosensor device in the Chapter 6.

4.5 Conclusion

In this chapter, we have described the network topology for the BSN of the capsular biosensor. We have also described the Zigbee protocol for RF telemetry and presented the necessary formulas to calculate the link budget for the operation of an RF link through the human body. Next, we presented the software workflow to run the Zigbee protocol and data acquisition on a general low power μC. Finally, we have taken the primary stages of the workflow and analyzed the power consumption of each stage in the context of the Zigbee packet structure. In chapter Chapter 6, we will present the final design of our capsular biosensor and use the equations presented in this chapter to predict the radio and power performance of the device.

Chapter 5

Design of a Miniature Fluorometer for Bleeding Detection

5.1 Introduction

In this chapter, we present the complete design for the measurement optics and electronics to detect a fluorescent dye as a tracer indicating gastrointestinal bleeding. We begin by formally quantifying acute GI bleeding, and choose an appropriate fluorophore to be used as a tracer to detect bleeding. Next, we determine the necessary concentration limit of detection C_{LOD} to detect acute GI bleeding within an specific period of time t_{LOD}. Then, we present a complete design for a miniature fluorometer and calculate its theoretical sensitivity. Finally, we design the transducer and amplification electronics, and evaluate the predicted limit of detection in the context of detecting acute GI bleeding.

5.2 Choice of Fluorescent Tracer

We intend for the capsular blood detector to be immediately clinically relevant, and so we are constrained in the choice of fluorophore to those currently FDA approved for intravenous injection as fluorescent tracers in humans. The most common fluorophores that fulfill this criteria are Fluorescein Disodium (FD), Indo-Cyanine Green (ICG), and Methylene-Blue (MB). FD and ICG are typically used as contrast agents in opthomalogy and to study renal function [26][45], while MB is typically used as a tumor stain in oncology [46]. We compare these three fluorophores in Table 5.1 by listing the peak excitation wavelength (λ_{ex}), peak emission wavelength (λ_{em}), molar absorptivity (α), quantum yield (Q) in aqueous solution, and intravenous half-life ($T_{1/2}$) of the fluorophores in blood.

Fluorophore	λ_{ex} (nm)	λ_{em} (nm)	$\alpha(\lambda_{ex})$ (cm^{-1}M^{-1})	Q	$T_{1/2}$ (min.)
Fluorescein	490	520	0.9×10^5	90	84
Indo-Cyanine Green	780	830	1.5×10^5	1.2	3
Methylene Blue	665	710	0.7×10^5	4	5

Table 5.1: The following properties are listed for FD, ICG, and MB: peak excitation wavelength (λ_{ex}), peak emission wavelength (λ_{em}), molar absorptivity (α), and quantum yield (Q) in aqueous solution, as well as the intravenous half-life ($T_{1/2}$) of the fluorophores in blood. [47]

Optical Absorption and Quantum Yield

Examining Table 5.1, it is clear that while the absorption coefficients α are similar, the quantum yields Q are vastly different. For low concentrations ($C \ll 1$ mM) of fluorophore and a short optical path length ($d \ll 1$ m), the fluorescence power P_f for a fixed concentration C of fluorophore in a specific fluorometer geometry will follow

Eq. (2.32). Under these conditions, the detected power P_f for a fluorophore n will be

$$P_f \propto Q \cdot \alpha(\lambda_{ex}), \tag{5.1}$$

where Q is the quantum yield of fluorophore, and $\alpha(\lambda_{ex}^n)$ is the molar absorptivity of the fluorophore, evaluated at its peak absorption wavelength λ_{ex}^n. Using the values in Table 5.1, we find that the relative fluorescence powers for the different fluorophores under identical conditions would be $P_f^{FD}/P_f^{MB} = 29$ and $P_f^{FD}/P_f^{ICG} = 45$. This means that for equal concentrations of fluorophore and fluorometer geometry, we require 29 - 45 times more incident optical excitation power to achieve the same fluoresence intensity. For a small battery power device where power consumption needs to be tightly regulated, this substantial difference in excitation powers to get equivalent fluorescence signals is very significant.

Pharmacokinetics

According to the device specifications in Chapter 1, the capsular blood detector requires the ability to detect the tracer dye for at least a time $t \geq 4$ hours. In Chapter 2, we defined the concentration limit of detection of a fluorophotometer as the minimum concentration C_{LOD} of fluorophore that it can reliably detect, and found that $C_{LOD} < C_{iv}(t)$ for successful detection, where $C_{iv}(t)$ is the intravenous fluorophore concentration after injection at time $t = 0$. The maximum intravenous dose of fluorophore is typically around an initial concentration of $C_o \approx 100\ \mu$M [27]R, and so using Eq. (2.1) and the data in Table 5.1 we find that at $t = 4$ hours, the remaining concentrations of fluorophore would be $C_{FD} \approx 10\mu$M, $C_{ICG} \approx 10^{-4}$ fM, and $C_{MB} \approx 10^{-13}$ fM. Clearly ICG and MB are much more rapidly removed from the blood stream than fluorescein. After $t \geq 4$ hours, the the concentrations of ICG and MB are so low that they would only only be detectable by a fluorophotometer with single fluorophore sensitivity, a technique that is not readily miniaturizable for the capsular form-factor.

Conclusion

The combination of superior quantum yield and long intravenous half-life in comparison with other FDA approved intravenous fluorophores make *fluorescein* an excellent choice for our application.

5.3 Detecting Acute GI Bleeding

5.3.1 Quantifying the Bleeding Detection Threshold

The purpose of the capsular bleeding detector is detect acute GI bleeding when it occurs early in stage I blood loss (discussed in Chapter 1). The total blood volume of V_t in an average adult human male is $V_t \approx 5$ liters [48], and a volume of blood loss $V_b(t)$ at some time t is considered a stage I GI bleed when $V_b(t) < 0.15\, V_t$ (Chapter 1), which requires that $V_b(t) < 750$ mL of accumulated blood in the GI tract. However, even a healthy individual may still experience a typical rate of GI bleeding up to ≈ 1 mL/day [48]. Therefore, to be sensitive enough to provide early warning of stage I active GI bleeding, while avoiding constant false positives due to the normal amount of GI bleeding, we require that the fluorophotometer must have a detection threshold that is 1 mL $< V_b(t) \ll 750$ mL of accumulated blood loss. We choose a detection threshold volume V_a of for acute GI bleeding to be

$$V_a \equiv \text{ 10 mL}$$

of accumulated blood loss as a compromise between these two extremes. The fundamental performance requirement of the capsular bleeding detector is as follows:

1. The device must be able to detect V_a of blood that bleeds out in **any** way after initial injection of the intravenous tracer at $t = 0$.
2. The device must be able to do this reliably for at least $t^0_{LOD} \equiv$ 4 hours after initial injection, where t^0_{LOD} is the minimum allowable time limit of detection for our system.

Since the total volume of accumulated blood $V_b(t)$ is a monotonically increasing quantity, any volume $V_b(t) > V_a$ will by definition occur later in time then when V_a was reached, and thus detection of V_a is a necessary and sufficient condition for detection of *early* stage I acute GI bleeding for $t \leq t^0_{LOD}$

5.3.2 Detecting Blood Volume by Measuring the Concentration of Fluorescein

In Chapter 2, we developed a theoretical model for converting a volume of blood loss $V_b(t)$ into a bound on the detected concentration $C_S(t)$ for GI bleeding occurring in the stomach. As the most capacious segment of the GI tract, the lowest concentrations for equivalent blood loss will be reached in he stomach, and thus bounding our concentration limit of detection C_{LOD} within the geometry of the stomach is sufficient for detecting bleeding anywhere in the GI tract.

The maximum concentration of fluorescein that is FDA approved for intravenous injection is $C_0 = 300\ \mu$M, and according to Table 5.1, the blood half-life of fluorescein is $t_{1/2} = 84$ minutes. The human stomach can normally contain a volume $V_0 \approx 1$ L of contents [48], and thus we assume that the stomach has a fixed volume V_0 of contents at for all time $t > 0$ to calculate the lowest dilution possible. For a total accumulated volume of blood loss $V_b(t) = V_a$, the minimum possible concentration $C_{min}(t)$ achieved in the stomach at any time $t > 0$ according to Eq. (2.9) is shown in Fig. 5.1. We have seen in Section 2.5.3 that the fluorophore concentration C_s in the stomach is directly proportional to the a detectable optical power P for a given fluorometer. Since the detector will have a fundamental power limit of detection P_{LOD} (discussed in Section 5.5) imposed by unavoidable noise intrinsic to the detector electronics the system fluorescence detection will be limited by a corresponding concentration limit of detection C_{LOD}.

As the intravenous concentration $C_{iv}(t)$ decreases in time (Eq. (2.1)), so does the minimum possible stomach concentration $C_{min}(t)$, and due the non-zero C_{LOD}, the

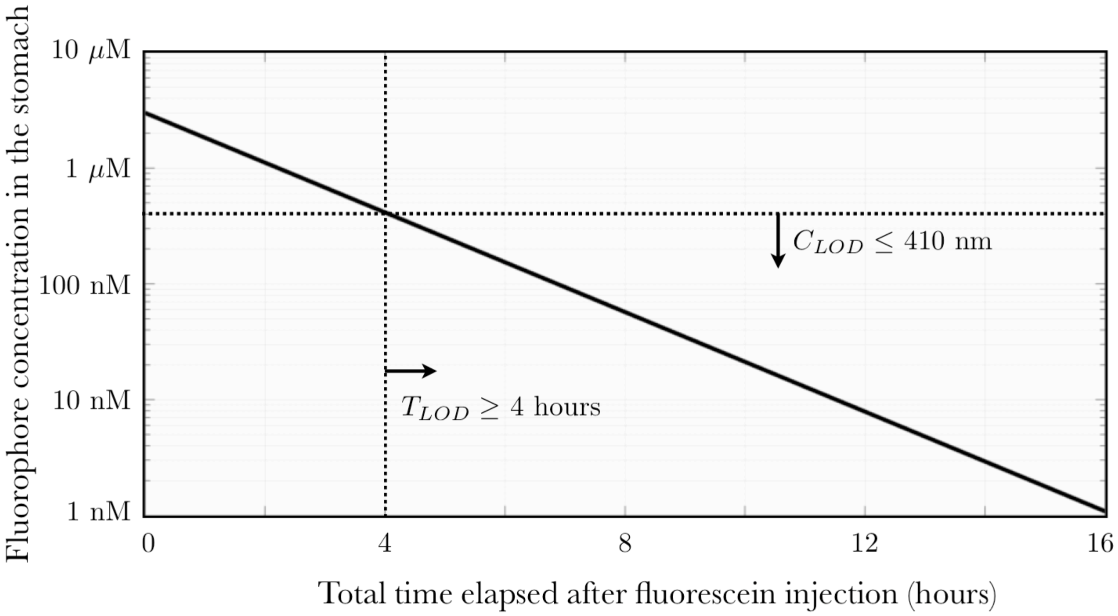

Figure 5.1: caption

fluorometer will not be sensitive to $C_{min}(t)$ forever. At some time $t = t_{LOD}$, we will find that $C_{min}(V_a, t_{LOD}) = C_{LOD}$, and thus for times $t > t_{LOD}$ we will have $C_{min}(V_a, t) < C_{LOD}$, at which time the fluorophotometer will no longer be able to always to detect V_a.

To satisfy the performance requirements delineated in Section 5.3.1, we require that the concentration limit of detection C_{LOD} satisfies $C_{LOD} \leq C_{min}(t^0_{LOD})$. According to Eq. (2.9) this evaluates to the requirement that

$$C_{LOD} \leq \text{ 410 nM.} \tag{5.2}$$

for the device to successfully detect $V_a = 10$ mL that bleeds out in *any* way during a time period $t \leq t^0_{LOD} = 4$ hours. For a $C_{LOD} < 410$ nM, we will be able to extend the t_{LOD} of the device beyond t^0_{LOD}, as seen in Fig. 5.1.

5.4 Fluorometer Design

5.4.1 Overview

In this section we present the design for a miniature fluorometer that detects the concentration of a fluorophore. We choose appropriate optical filters and LED to detect fluorescein and then present the fluorometer optical design. Finally we calculate the relationship between fluorescein concentration and detectable fluorescence intensity.

5.4.2 Choice of Optical Components

To simplify the fabrication of the device and reduce cost, we use off-the-shelf filters designed for fluorescence microscopy. We choose a low pass (LP) excitation filter (NT64-593, Edmund Optics) and bandpass (BP) emission filter (MF525-39, Thorlabs) with properties listed in Table 5.2, along with a miniature surface mount blue LED (LB E63C, OSRAM, Inc.) with specification in Table 5.3.

Filter Type	Thickness (mm)	Cut-on wavelength (nm)	Cut-off wavelength (nm)	Pass-band transmission (%)	Stop-band attenuation (dB)
Excitation	1.0	n/a	475	95	-20
Emission	1.9	506	545	90	-50

Table 5.2: Excitation and Emission filter properties.

Blue LED, LB E63C (OSRAM, Inc.)	
Size ($L \times W \times H$)	$3.4 \times 3.0 \times 3.5$ mm^3
Peak Wavelength	465 nm
Viewing Half-Angle	10^o
Optical Efficiency	30 mW/A

Table 5.3: LED specifications.

The LED also has an integrated lens with a viewing half angle of 10° which helps deliver more light intensity to a small sample volume very close to the LED. The transmission bands of the optical filters at normal incidence superimposed on the LED excitation spectrum and fluorescein absorption and emission spectra are shown in Fig. 5.2.

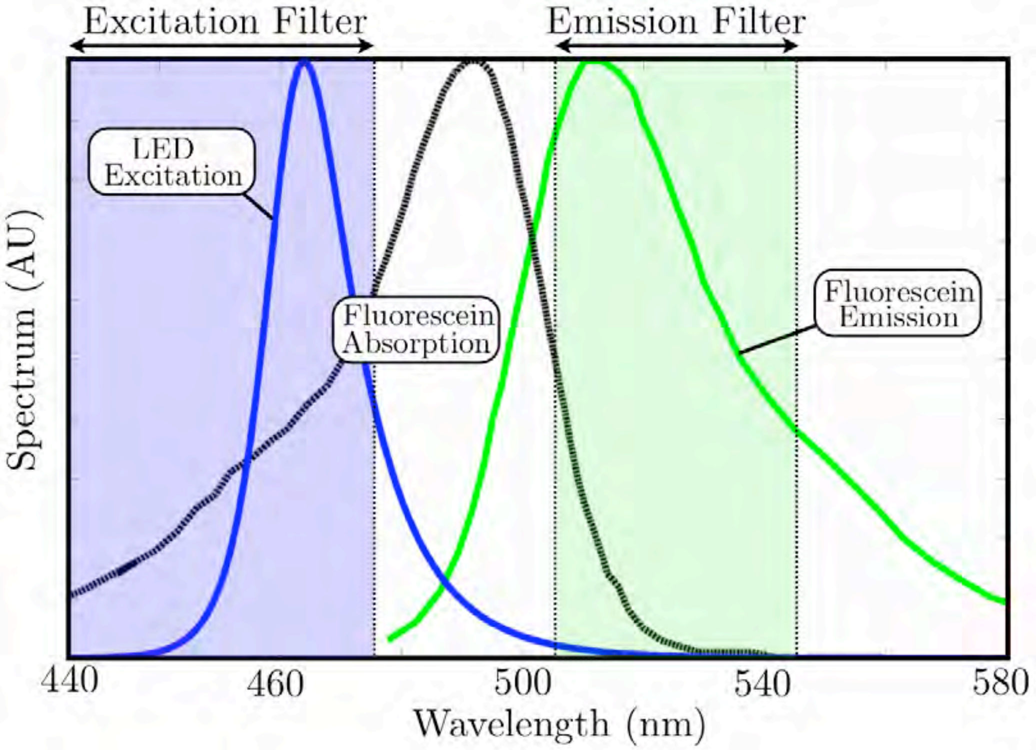

Figure 5.2: caption

We have chosen to excite the fluorescein at wavelengths shorter than peak excitation to create a wide isolation region Δ between the excitation and emission light, extending from 475 nm to 506 nm. As we have seen in Section 2.4.3, light incident at angles θ to the normal will encounter a blue-shifted passband, and if the isolation region is not wide enough excitation light may reach the detector, registering as a false signal. Thus, we have chosen a wide isolation region to allow the filter to work as intended for larger angles of incident light, leading to more collected light. The precise values were dictated by available parts that had both small size (LED) and thickness (filters).

Examining Fig. 5.2, we can see that the isolation region will be eliminated if the emission filter passband blue shifts by more than Δ_{max} = 506 nm - 475 nm = 31 nm. For an angle of incidence θ to the filter normal, the emission filter blue shifted pass band will behave according to Eq. (2.12), which is plotted in Fig. 5.3 for $\lambda_i = 525$ nm, and $\lambda_f = \lambda_i - \Delta_{max} = 494$ nm. Also shown is the full width half maxima (FWHM) of the fluorescein emission spectrum as well as the cut-off wavelength of the excitation filter. Inspection of Fig. 5.3 shows that the angle of incidence θ, must not exceed the critical angle of $\theta_c = 31^o$, if an optical isolation barrier between the excitation and emission filters is to be maintained.

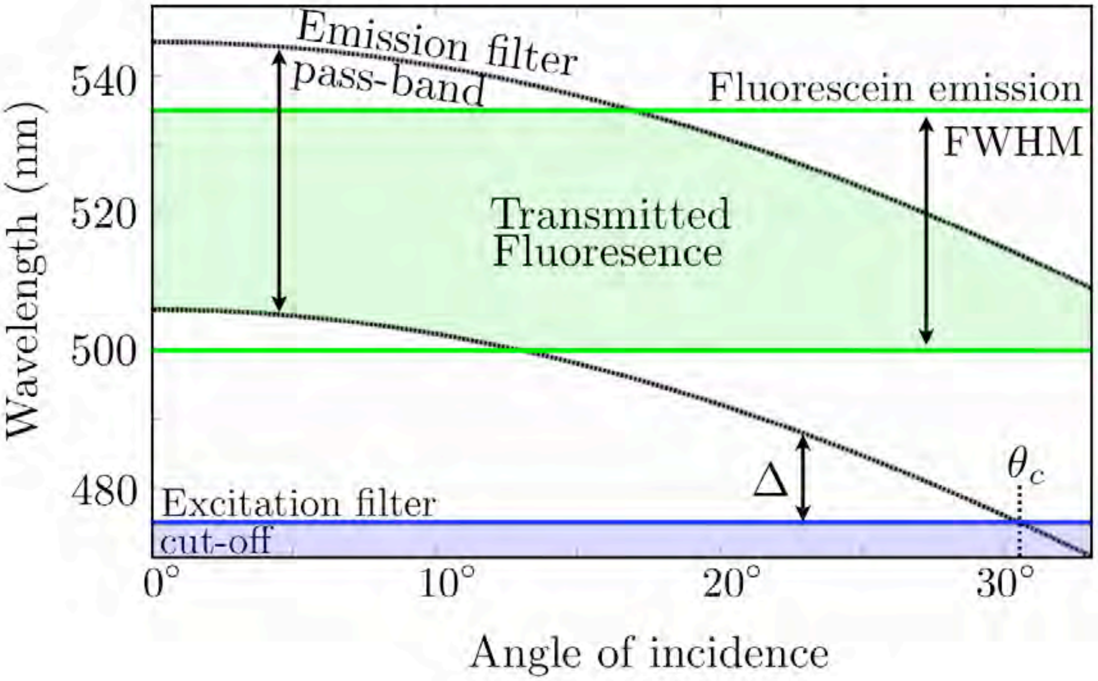

Figure 5.3: caption

Furthermore, the amount of passed emission light begins to decrease for $\theta > 17^o$, as the filter pass-band becomes more misaligned with the fluorescein emission spectrum. We choose the maximum allowable incident angle of light $\theta_{max} = 17^o$ because it maintains a 21 nm isolation band that reduces contribution from leaked excitation light, while passing most of the fluorescein emission.

Pinholes

As we have seen in Section 2.4.3, a pair of pinholes on either side of optical filter will constrain the angles of light that are passed through the filter. For an aqueous medium with index of refraction $n_w = 1.33$, and a glass filter with effective index $n_e = 1.5$, and thickness $t_f = 1.9$ mm (Table 5.2) we find that according to Eq. (2.16), a pinhole diameter $L_D = 0.5$ mm will constrain all angles of incidence to $\theta \leq 17^o$.

5.4.3 Optical Geometry

We now present the complete optical geometry for the fluorometer. A 3D schematic of the device (Solidworks, Corp.) is shown in Fig. 5.4. The LED and photodiode (described in Section 5.4.2) along with the optical filters are placed at right angles. Pinholes with $L_D = 0.5$ mm are included to constrain the angle of incidence. The detection volume is 0.2 μL, and the fluorometer dimensions are shown in Fig. 5.5.

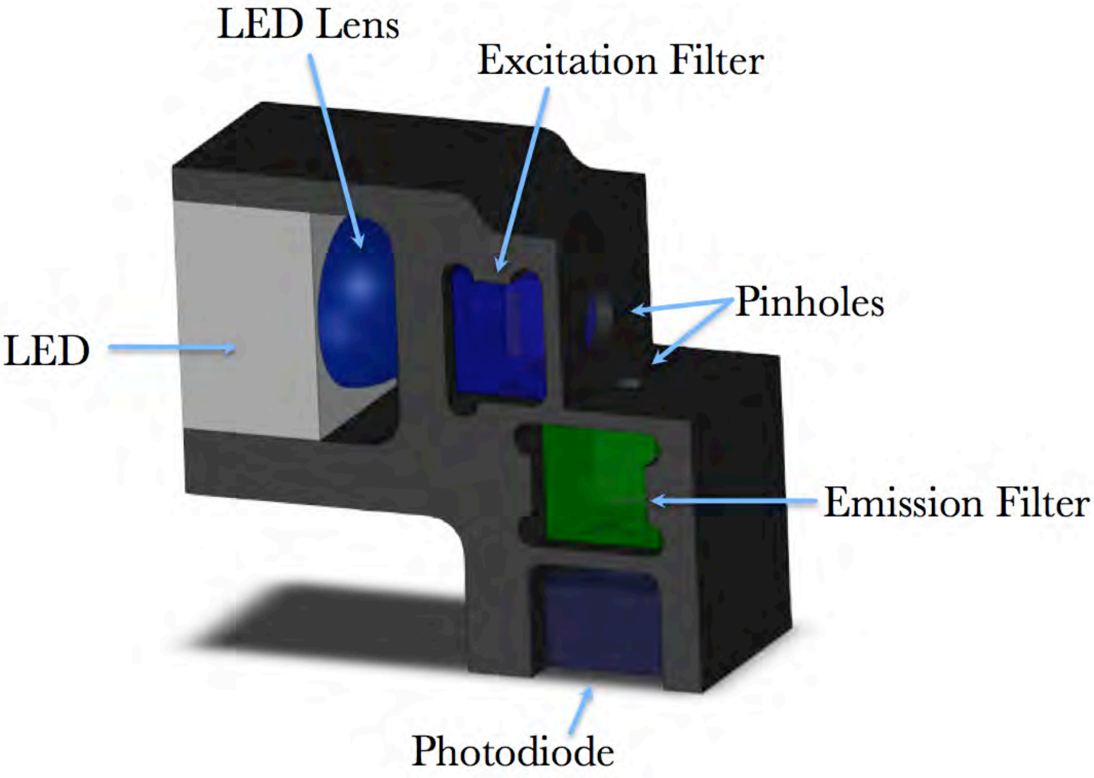

Figure 5.4: Fluorometer schematic. The detector photodiode is discussed in Section 5.5

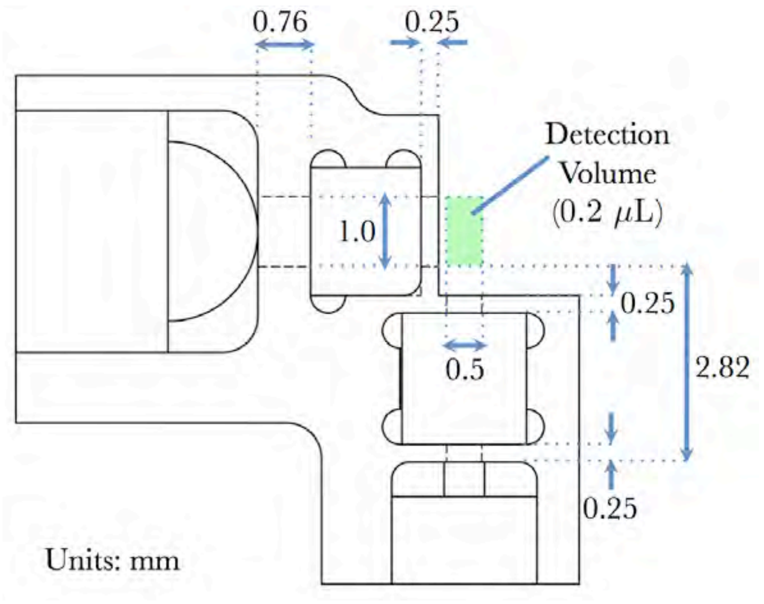

Figure 5.5: Fluorometer CAD schematic.

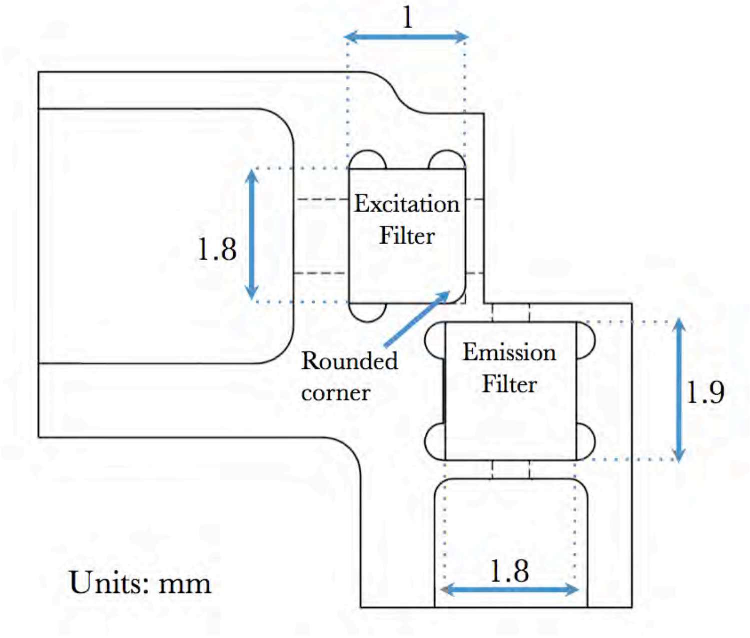

Figure 5.6: Fluorometer CAD schematic.

5.4.4 Detection Optical Intensity

We aim to calculate the low concentration sensitivity to ultimately find the concentration limit of detection C_{LOD}. First, we assume that the LED will excite the sample monochromatically at $\lambda_{ex} = 460$ nm. For this excitation wavelength, pure human blood has an absorption coefficient $\mu_b = 135$ cm^{-1}. Our fluorescein detection threshold is set at $V_a = 10$ mL in a stomach with 1 L of contents, and so we are dealing with dilutions $D \approx 1\%$. The blood absorption coefficient is thus altered such that the effective absorption coefficient factoring in dilution in the stomach is $\mu_b' = \mu_b \, D \approx 1.4$ cm^{-1}. Fluorescein has an absorption coefficient $\mu_f = \alpha \, C_s = 0.03$ cm^{-1} for $C_s = 410$ nM and $\alpha = 30{,}800$ cm^{-1} M^{-1} at $\lambda_{ex} = 460$ nm. For $x \approx 0.5$ mm typical of our geometry, we find that $\mu_b' \, x \ll 1$ and $\mu_f \, x \ll 1$. Thus, while blood is more absorptive than fluorescein at $\lambda_{ex} = 460$ nm, the overall attenuation is negligible over the span of $x \approx 0.5$ mm, and we are thus justified in using the low attenuation approximated given by Eq. (2.32).

For a total power P_{det} reaching the detector pinhole, the total optical intensity I_{det} per unit concentration of fluorescein is

$$I_{det} = \frac{P_{det}}{C_s \, A_{det}}, \tag{5.3}$$

where $A_{det} = \pi \, (L_d/2)^2$ is the detector pinhole area. In the low attenuation limit, the optical sensitivity, following Eq. (2.32), reduces to

$$I_{det} \approx \frac{P_0 \, Q \, L_d^2 \, \alpha(\lambda_{ex})}{4 \, \pi \, L_i^2} \left(\frac{1}{y_0} - \frac{1}{y_0 + L_i} \right), \tag{5.4}$$

where P_0 is the incident LED power, Q the quantum yield of fluorescein, L_i the excitation pinhole diameter, and y_0 the height of the excitation pinhole above the detector surface.

Eq. (5.4) is the ideal sensitivity, and does not factor in the passband mismatch between filters and light sources, as well as filter loss and reflection at surfaces. Examining figure Fig. 5.2, we find that the overlap between LED spectrum and excitation filter pass-band is 75%, and overlap between fluorescein emission spectrum and emission filter passband is 63.8%. Also, the transmissions are 95% for the excitation filter, and 90% for the emission filter. Furthermore, due to the LED pinhole, we have restricted the light from the LED to an $\approx 11^o$ half-angle, which, according to the LED specification, corresponds to 50% of the total output power. All these non-idealities multiplied together gives a correction factor of

$$\xi_0 = 0.2. \tag{5.5}$$

When the LED is driven with 10 mA, it will produce a power

$$P_0 = 30 \text{ mW/A} \times 10 \text{ mA} = 30 \ \mu\text{W}. \tag{5.6}$$

For $Q = 0.9$, $L_d = 0.5$ mm, $L_i = 1$ mm, $\alpha = 30{,}800 \text{ cm}^{-1}\text{M}^{-1}$, $y_0 = 2.83$ mm, and correcting by a factor of ξ_0, the fluorometer optical intensity concentration sensitivity is

$$I_{det} \approx 313 \, \frac{\text{nW/m}^2}{\text{nM}} = 313 \, \frac{\text{fW/mm}^2}{\text{nM}}. \tag{5.7}$$

In the next section, we will determine the power limit of detection P_{LOD} of the detection electronics to convert Eq. (5.7) into a more useful metric for detecting blood: the concentration limit of detection C_{LOD} and time limit of detection T_{LOD}.

5.5 Measurement Electronics

5.5.1 Overview

In this section, we choose electronic components for the capsular biosensor. We first review the design challenges of the capsular form-factor. We then present our choice of microcontroller (μC) and introduce the other front end measurement components (photodiode, opamp, etc.). Next, we design the transducer, transimpedance amplifier, and filtering stages. Finally, we use the circuit design parameters to calculate the predicted P_{LOD} for the device.

5.5.2 Electronic Component Constraints

The size and untethered nature of the capsular biosensor platform forces a trade off with circuit complexity and signal quality. If size, voltage supply, and power consumption were not an issue, it would be straight forward to design both a measurement front-end and central processing hardware to fulfill all the desired functions of the device with high accuracy. However, the small form factor of the capsular device presents a set of unique design challenges:

1. **Voltage**: To power a device of small size, a small battery must be used (discussed in Section 6.5). Batteries of this size typically offer supply voltages from 1.5 - 3.7 V. Thus any active components used must be able to run from a low voltage, single-sided supply ($V_{cc} \leq$ 1.5 - 3.7 V, $V_{ee} = 0$ V).

2. **Size**: To preserve compactness, we must take a minimalist approach to the electronic design. We wish to gain the maximal functionality and signal quality

from the fewest amount of components. Furthermore, each component should be in the a sub-miniature surface mount package size.

3. **Power**: We require low power consumption for each active component, with a quiescent current preferably $I_Q < 0.1$ mA.
4. **Quality**: All components must be very low noise.
5. **Cost**: We desire to keep cost and time to market low, so we prefer to use only off-the-shelf components.

5.5.3 Detector Component Selection

We now choose a suitable photodiode and op-amp to transduce the the optical signal to a current, and convert that current to a voltage with a transimpedance amplifier. In addition to satisfying the constaints in section 5.5.2, it is also necessary to keep input current noise extremely low ($\ll$ pA/$\sqrt{\text{Hz}}$). To that end, we choose the PIN photodiode and TIA op-amp with specifications listed in Table 5.4 and Table 5.5.

PIN Photodiode: PDB-C122 (Advanced Photonix, Inc)	
Length x Width x Height	2 x 1.5 x 1.7 mm^3
Active area (A_{pd})	0.33 x 0.33 mm^2
Responsivity (R) at $\lambda_{em} = 520$nm	0.27 A/W
Current Noise (i_{pd})	2 fA/$\sqrt{\text{Hz}}$
Shunt Resistance (R_{sh})	500 MΩ
Junction Capacitance (C_j)	5 pF

Table 5.4: Photodiode specifications.

Op-Amp: ADA-4505-2 (Analog Devices)	
Length x Width x Height	1.4 x 1.4 x 0.4 mm^3
Supply Voltage (V_{cc})	1.8 V - 5 V (rail-to-rail)
Power Supply when $V_{in}^{-} = V_{in}^{+}$	10 μA
Unity Gain Bandwidth (f_g)	50 kHz
Input Current Noise (i_{op})	2 fA/$\sqrt{\text{Hz}}$
Input Voltage Noise (v_{op})	65 nV/$\sqrt{\text{Hz}}$
1/f Noise Corner frequency (f_c)	10 Hz
Input Capacitance (C_{in})	7.2 pF

Table 5.5: Opamp specifications.

These parts have been chosen for their excellent noise performance, low power supply current, single rail low voltage supply, and extremely small surface mount size. Furthermore, the ADA-4505 comes in a package of 2 op-amps in an 8-ball WLCSP package which is extremely convenient for our application.

For data acquisition, we will be using the onboard ADC of the EM250 system on chip (discussed in Chapter 6). The relevant characteristics of the ADC for data acquisition are shown in Table 5.6

EM250 ADC	
Voltage Range	0 - 1.2 V
Sampling Rate	1.65 kHz
ENOB	12 bits (0.3 mV resolution)

Table 5.6: ADC specifications.

Generated Input Current

For a given concentration of fluorescein C_s, and detector active area A_{pd} the total power incident on the detector will be $P_{det} = I_{det} \cdot C_s \cdot A_{pd}$, and current generated by the photodiode will be $I_{pd} = R \cdot P_{det}$, where R is the detector responsivity. Therefore, the total generated current will be

$$I_{pd} = R \cdot I_{det} \cdot C_s \cdot A_{pd} \tag{5.8}$$

5.5.4 Measurement

The entire measurement front end circuitry is shown in Fig. 5.7.

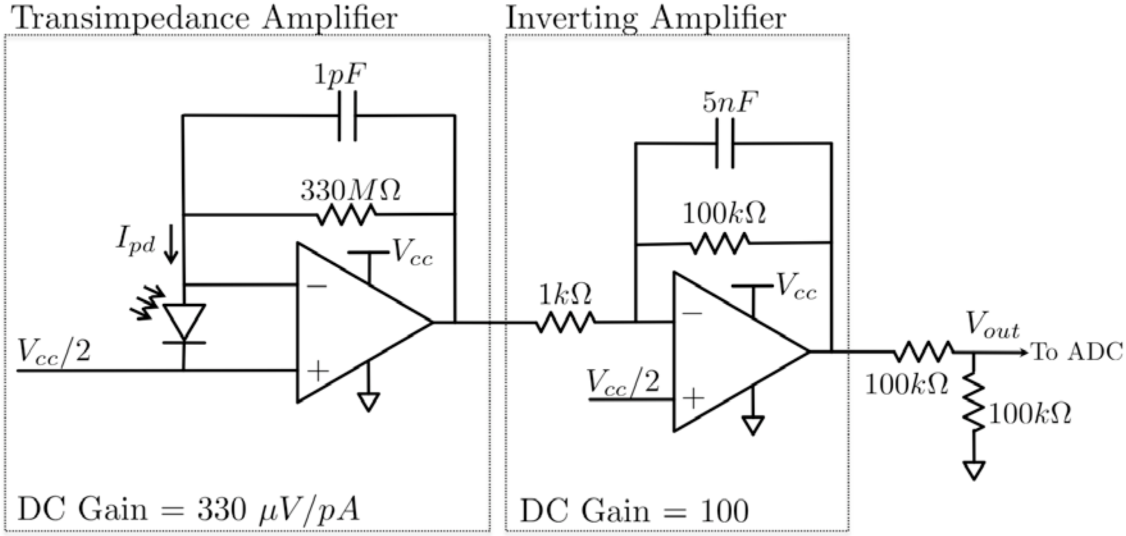

Figure 5.7: Measurement circuit.

The measurement circuitry can be be broken up into three stages: transimpedance amplifier, inverting amplifier, and voltage divider.

Transimpedance Amplifier

We want to get the maximum possible gain, while preserving enough bandwidth to still pass a signal. This entails choosing a large feedback resistance R_f, a feedback capacitor that eliminates TIA ringing, yet optimizing the two components so that the signal bandwidth remains far enough above the 10Hz 1/f noise corner frequency. We choose a feedback resistance of $R_f = 330$ MΩ to provide a DC current gain of $H_i = 330\ \mu$V/pA, and feedback capacitance of $C_f = 1$ pF eliminates TIA ringing. The feedback resistor and capacitor together enforce a 482 Hz low pass cut-off frequency, keeping the signal and noise bandwidth below the ADC Nyquist frequency of $f_n = f_s/2 = 825$ Hz [36], thus reducing aliasing of high frequency noise. Using Eq. (3.29) with the values for the opamp input capacitance C_{in}, photodiode junction capacitance C_j, and photodiode shunt resistance R_{sh} we show the current transfer function $H_i(f)$ in Fig. 5.8.

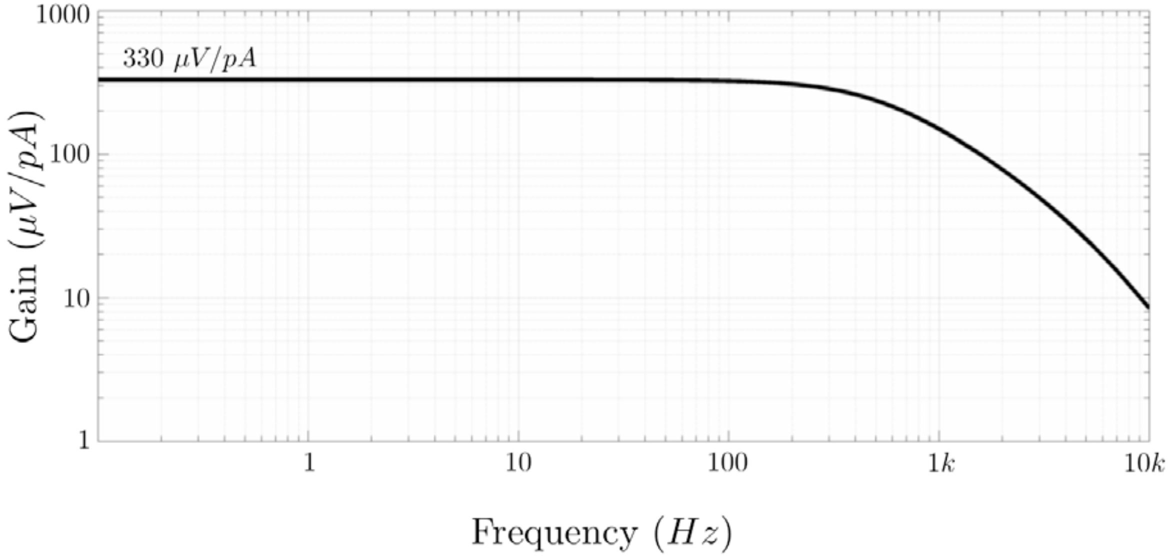

Figure 5.8: TIA current to voltage transfer function

Using Eq. (3.35) - Eq. (3.39) and the values from the component specifications in Table 5.4 and Table 5.5, we find that the low frequency contributions to the input referred current noise spectral density for the opamp are $i'_{op,i} = 2$ fA/$\sqrt{\text{Hz}}$ from input current noise, and $i'_{op,i} = 0.3$ fA/$\sqrt{\text{Hz}}$ from input voltage noise. The contribution

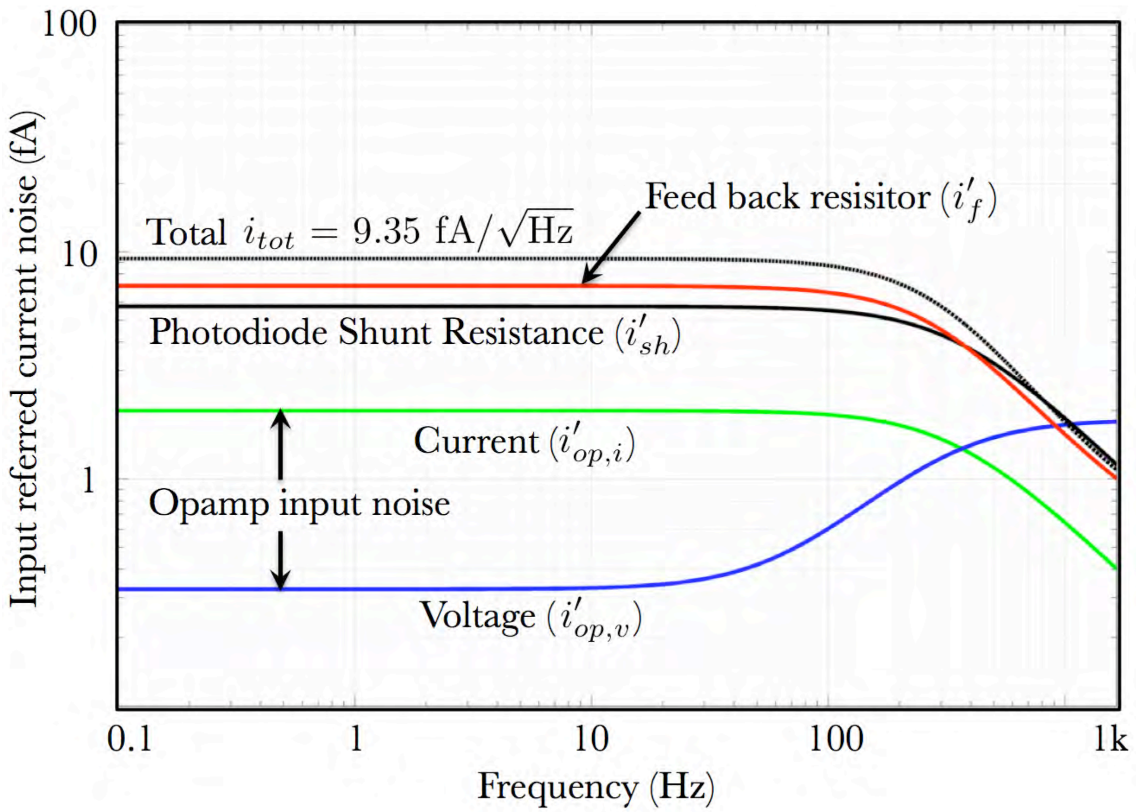

Figure 5.9: Input referred current noise due to all TIA noise sources. Each curve is labeled with its corresponding noise source

from photodiode current noise is $i'_{pd} = 5.75$ fA/$\sqrt{\text{Hz}}$ and the feedback resistor is $i'_f = 7.1$ fA/$\sqrt{\text{Hz}}$. Thus the total input referred current noise spectral density for low frequencies following Eq. (3.41) is $i_N = 9.35$ fA/$\sqrt{\text{Hz}}$, and is clearly dominated by the feedback resistor. The input referred contributions for each noise source and noise is shown in Fig. 5.9.

Additional Amplification Stage

Using Eq. (5.8), we find that for our target concentration limit of detection $C^0_{LOD} = 410$ nM, fluorometer sensitivity $I_{det} = 313$ fW mm^{-2} nM^{-1}, photodiode responsitivity $R = 0.27$ A/W at $\lambda = 525$ nm, and photodiode area $A_{pd} = 0.11$ mm^2, the current generated in the photodiode is $I^0_{pd} = 74$ fA. For the TIA low frequency gain $H_i = 330\ \mu$V/pA, this corresponds to a output voltage $V^0_{TIA} = 24\ \mu$V. The ADC we are using has 12 effective bits of resolution and a voltage range of 0 - 1.2 V leading to a signal resolution of 1.2 V / $2^{12} \approx$ 0.3 mV, which is not enough to resolve V^0_{TIA}. Thus we need further amplification to bring the signal into the range of the ADC. We add a second amplification stage consisting of an inverting amplifier with 100X gain to put the signal in the range of the ADC. The ADA-4505 used for the TIA conveniently comes in a CSP form-factor with 2 op-amps which allows us to stay compact while adding a second gain stage. We add a 5 nF feedback capacitor in parallel to the 100 kΩ feedback resistor to short the amplifier gain for frequencies above $f_c = 318$ Hz, thus behaving as single pole low pass filter. This low pass filtering combines with the two-pole role off of the TIA to effectively eliminate aliasing of high frequency noise into the ADC's Nyquist band of $\Delta f = f_n = 825$ Hz.

Voltage Divider

Lastly, the opamps will be running off of 0 - 3.3 V supply rails (discussed in Section 6.5.2), and the reference voltage for both gain stages is fixed at $V_{cc}/2 = 1.65$ V, which is now the output voltage for a zero input signal. This corresponds to a signal range at the output of the second stage of 0 V$< V_s <$ 1.65V . To put the signal into the voltage range of the ADC, a 50/50 voltage divider is added before the ADC input to shift the signal range to 0 V$< V_s <$ 0.83 V. Any signals outside the sampled voltage range will lead to sampling error, and so the buffer zone spanning 0.83 V - 1.2 V is left to account for any signal overshoot. All noise from the second amplification stage and voltage divider is negligible compared to the TIA.

Digital Filtering

In Section 3.5 we found that the N point digital "lock-in" filter effectively narrows the measurement bandwidth to $\Delta f = f_n/N$, around the signal frequency f_{sig}. We will measure at a signal frequency f_{sig} = 90 Hz and average over N_{LED} = 40 cycles of the signal, which for the ADC sample rate f_s=1.65 kHz, corresponds to N = 720 sampled points. Therefore, the measurement bandwidth is reduced to Δf = 825 Hz/720 = 1.15 Hz.

5.6 The Limit of Detection

Now that the entire fluorometer, transducer, and data acquisition system has been analyzed, we can calculate the detection limit of our device by working backwards starting from the electronics. The input referred current noise density was found to be i_N = 9.35 fA/$\sqrt{\text{Hz}}$. The digital "lock-in" filtering serves to narrow the bandwidth to Δf = 1.15 Hz. Therefore we expect an input referred current noise variance of σ_{in}^N = 10 fA. The current limit of detection $I_{LOD} = 3\,\sigma_{in}^N$ is thus

$$I_{LOD} = 30 \text{ fA}. \tag{5.9}$$

Using the photodiode responsivity $R = 0.27$ A/W, we find that the power limit of detection P_{LOD} of the detector is expected to be

$$P_{LOD} = 111 \text{ fW}. \tag{5.10}$$

Using the photodiode active area $A_{pd} = 0.11 \text{ mm}^2$, and the fluorometer sensitivity of $I_{det} = 313 \text{ fW mm}^{-2} \text{ nM}^{-1}$, we find that the concentration limit of detection C_{LOD} of the system is

$$C_{LOD} = 3.2 \text{ nM}. \tag{5.11}$$

Using Eq. (2.11) we find the that the theoretical time limit of detection T_{LOD} for detecting $V_a = 10$ mL of blood in $V_0 = 1$ L of stomach contents, after injection of $C_0 = 300\ \mu$M of fluorescein at time $t = 0$ is

$$T_{LOD} = 13.8 \text{ Hours} \tag{5.12}$$

Our target limits of detection were $C^0_{LOD} = 410$ nM, and $T^0_{LOD} = 4$ hours, and we find that our design should significantly outperform the device specifications.

5.7 Conclusion

In this chapter, we have presented the miniature fluorometer design and discussed the optical filters, pinholes, optics housing, and derived the theoretical concentration sensitivity of the fluorometer. We have also chosen all necessary electronics and designed a high sensitivity, low noise measurement circuit, and used a digital "lock-in" technique to reduce the measurement bandwidth. Finally, we have found the theoretical concentration and time limits of detection of the system to be well within our design specification.

Chapter 6

Design: Hardware Platform and Packaging of a Capsular Biosensor

6.1 Introduction

In this chapter we present, the entire design for a capsular "lab-in-a-pill" platform. We first choose an appropriate low power microcontroller and radio frequency electronics. Next we evaluate RF link budget in the body. Then, we choose an appropriate battery and analyze the device's power consumption to determine device lifetime. Finally, we present the miniature printed circuit board schematics and present a schematic design of the entire device.

6.1.1 Choice of Microcontroller

There are a number of IEEE 802.15.4 solutions currently on the market. The two most popular solutions use either a separate low power microcontroller (μC) and radio, or a single system on chip (SoC) which integrates the μC and radio into a single package. The first approach typically allows for more freedom in circuit design, and potentially more computation power and memory. However, for our low data rate, single measurement application, this is unnecessary. The latter approach typically offers better power efficiency and smaller overall size due to the high level of system integration, making it ideal for our design specification.

The two most popular Zigee SoC solutions are offered by Chipcon (subsidiary of Texas Instruments Inc.) and Ember Corp, with both offering similar performance and capability. We choose the Ember EM250 SoC, a highly integrated circuit that comes in a small surface mount package, and contains a microprocessor, flash memory, and a Zigbee radio. The EM250 general specifications are shown in Table 6.1.1.

System-on-chip: EM250 (Ember Corp.)	
Size	7×7 mm^2
Package	48 pin QFN
Microprocessor	XAP2B, 16-bit
Clock	12 MHz
Flash Memory	128 kB
Radio	Zigbee @ 2.4GHz
Voltage Supply	2.1 - 3.6 V
Digital I/O Channels	4 Channels
ADC Channels	4 Channels

Table 6.1: System-on-chip specification [44]

6.2 Hardware Platform Overview

By using an SoC to integrate the microprocessor, radio, memory, and ADC, we have significantly reduced the overall circuit complexity and size of the device. The entire device platform can be divided into four distinct categories (Fig. 6.1):

1. **Power Supply**: includes a battery and three separate voltage regulators to decouple the SoC[1], measurement, and LED driver circuitry.
2. **Sense Circuitry** - the electronics necessary to operate the fluorometer and aquire data:
    (a) Measurement circuitry: photodiode and amplifiers (Chapter Chapter 5)
    (b) LED and its current driver circuitry.
3. **System on Chip**: a single component - the Ember EM250. It includes a microprocessor, radio, memory, ADC, and digital I/O.
4. **Peripherals**: all remaining components necessary to run the platform
    (a) Crystal oscillator to supply the SoC with a clock signal and generate the 2.4 GHz frequency necessary for 802.15.4 telemetry.
    (b) RF front end: balanced / unbalanced signal conversion, microstrip line, and 2.4 GHz antenna

---

[1] While the EM250 has an internal voltage regulator, it is only rated for a maximum of 3.7 V input, and so we include an extra voltage regulator to allow battery voltages to exceed 3.7 Volts without adversely effecting the performance of the EM250.

(c) Routing and decoupling passives: resistors and capacitors to route power from one part of the SoC to another, and decouple the power lines from AC signals.

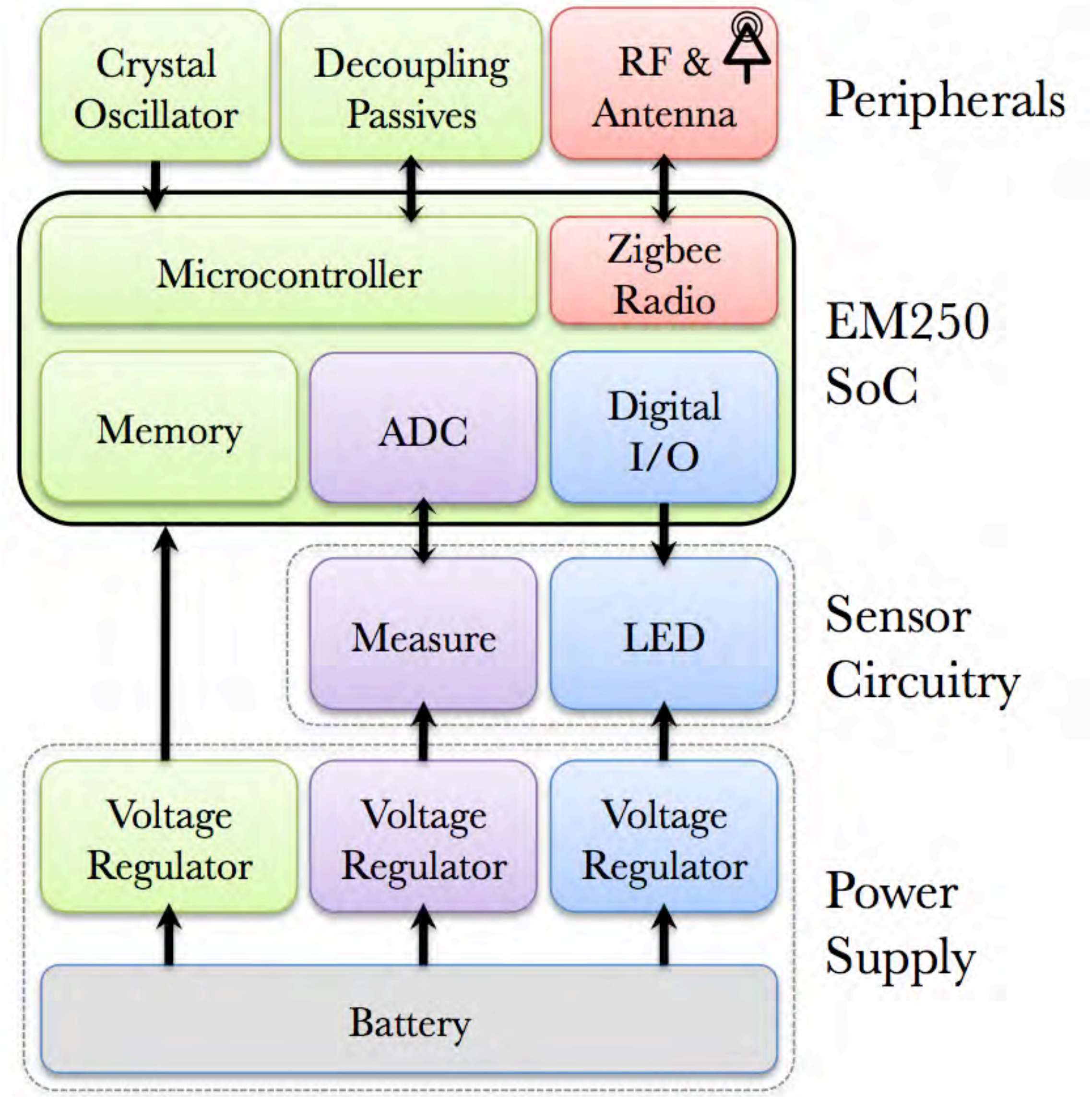

Figure 6.1: Platform hardware block diagram. Blocks are physically grouped according to function. Color coding provides a guide to how subsystems interact.

6.3 LED Pulsing Circuit

To pulse the LED, we use a digital I/O pin of the EM250, which can be switched between two states, 0V and 1.8 V. This logic pulse actives an NFET which connects the LED circuit to ground, allowing a current to pass through, and the LED to light. Our choice of NFET and LED are specified in Table 6.2 and Table 6.3, and the LED drive circuit shown in Fig. 6.2.

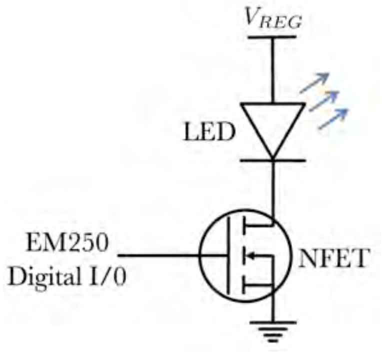

Figure 6.2: LED drive circuit.

Blue LED: LB E63C (OSRAM, Inc.)	
Size ($L \times W \times H$)	$3.4 \times 3.0 \times 3.5$ mm^3
Peak Wavelength	465 nm
Current (3.3 V)	10 mA
Total External Efficiency	30 mW/A

Table 6.2: LED specifications.

N-Channel Silicon MOSFET: EC4406C (Sanyo, Inc.)	
Size ($L \times W \times H$)	$1.0 \times 0.8 \times 0.6$ mm^3
Turn Off Voltage	≤ 0.4 V
Turn On Voltage	1.5 V

Table 6.3: NFET specifications.

6.4 Radio Frequency Communication

To minimize size, we choose an ultra-miniature 2.4 GHz dielectric chip antenna (Table 6.4) and surface mount ceramic balun (Table 6.5). We list relevant radio frequency (RF) parameters of the Ember EM250 SoC in Table 6.6, and present the designed RF circuitry in Fig. 6.3. The RF circuit is based on the EM250 SoC and WE-MCA antenna reference designs.

SMD Chip Antenna, WE-MCA (Wurth Electronics, Inc.	
Size ($L \times W \times H$)	$3.2 \times 1.6 \times 1.3$ mm^3
Frequency Range	2.4 - 2.5 GHz
Input Impedance	50 Ω
Average Gain (G_{ant})	- 0.5 dBi
Return Loss at 2.45 GHz (RL_A)	18.5 dB

Table 6.4: Antenna specifications.

SMD Multilayer Balun, HHM1521 (TDK Electronics, Inc.	
Size ($L \times W \times H$)	$2 \times 1.25 \times 0.95$ mm^3
Frequency Range	2.4 - 2.5 GHz
Unbalanced Impedance	50 Ω
Balanced Impedance	200 Ω
Insertion Loss at 2.45 GHz (L_I^B)	0.7 dB (max)

Table 6.5: Balun specifications.

EM250 SoC, RF Specifications	
Radio Transmission Power (P_{TX})	3 dBm (2 mW)
Radio Receiving Sensitivity (P_{RX})	-99 dBm (125 fW)

Table 6.6: EM250 Radio Frequency specifications.

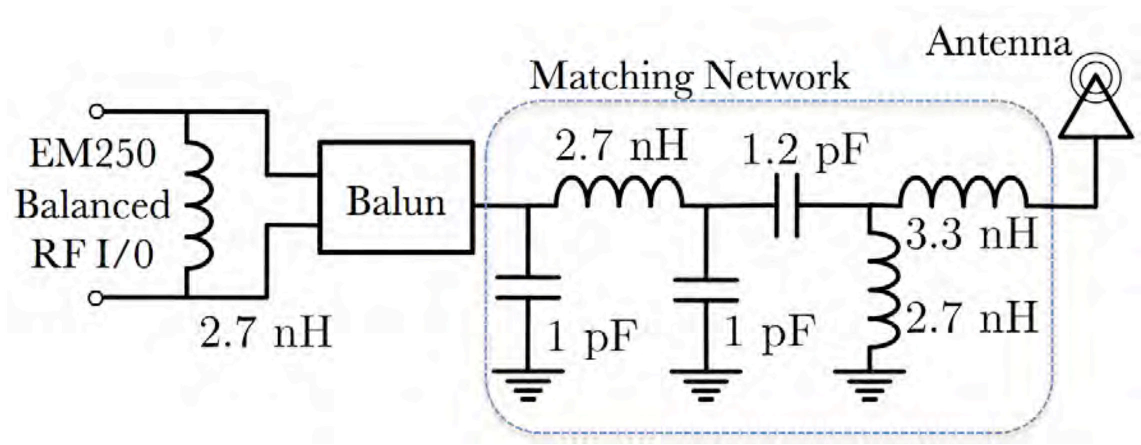

Figure 6.3: Radio frequency circuitry.

The EM250 radio input/output (I/O) is in the form a a two port balanced feed with 200 Ω output impedance. The ceramic balun is used to convert between the two line balanced and single line unbalanced versions of the RF signal, and impedance match between the 200 Ω balanced impedance, and 50 Ω antenna input impedance. A frequency matching π-network of reactive elements perform frequency filtering, and tunes the frequency of the antenna to 2.45 GHz, as necessary for the IEEE 802.15.4 standard. A 50 Ω controlled impedance microstrip line connects the unbalanced port of the balun with matching network and antenna (discussed in Section 6.6).

Using Eq. (4.4), we find that the antenna return loss of $RL_A = 18.5$ dB corresponds to a signal loss of $L_R = .06$ dB. The balun insertion loss is $L_I^B = 0.7$ dB, for a total electrical loss of $L_E = 0.76$ dB. The insertion loss due to all other passive components is negligible. Using Eq. (4.8), the total link budget for the system is thus

$$P_{RX} = P_{TX} - L_E + G_{ant} - L_{FS,Body} + G_{ant} - L_E, \tag{6.1}$$

where P_{RX} is the received signal electrical power (dBm), P_{TX} is the transmitted signal electrical power (dBm), L_E the electrical signal loss (dB), G_{ant} the antenna gain as different from an ideal isotropic antenna (dBi), and $L_{FS,Body}$ the loss due to body RF absorption and free space spreading of the RF wave (dB). We have explicitly assumed that the transmitting and receiving circuits are identical. For L_s = 0.76 dB, G_{ant} = -0.5 dBi, and $L_{FS,Body}$ = 70 dB, and P_{TX} = 3 dBm, we find that

$$P_{RX} = -69.5 \text{ dBm} = 112 \text{ pW}. \tag{6.2}$$

Comparing this to the minimum receiver sensitivity of -99 dB, we can see that we are just about three full decades above the minimum receive sensitivity.

To see what this means in terms of energy, we find that each 16-bit integer takes $\Delta t_{TX} = 2$ ms to transmit. At $P_{TX} = 3$ dBm = 2 mW, we would expend an RF energy of 4 μJ / integer, or 250 nJ / bit. Since we have a 29.5 dB buffer on the link budget, we can potentially lower the RF power to P_{TX} = -26.5 dBm $\approx$ 2.2 μW, such that we expend an RF energy of 4.4 nJ / integer, or 0.28 nJ / bit. This of course does not take into consideration the large current overhead that the radio and μC consume in order to operate, nor the length of the header in each packet.

6.5 Power

6.5.1 Battery

We choose to power the capsular biosensor with an onboard battery to ensure reliable and continuous access to a predictable energy supply in a small size. While it is becoming increasingly popular to use magnetic inductive coupling to power implanted devices, these usually require the patient to be placed near a large coil to supply RF magnetic energy [49]. We wish to emphasize mobility and simplicity for the patient, and since we do not need the device to function for years, a battery is sufficient for our purposes.

Battery energy densities tend to range from 0.2 - 2 kJ/cm^3, with voltages ranging from 1.35V - 3.7 V [50]. We choose a battery with specification listed in Table 6.7)

Li-Poly Battery, LP30-FR (Plantraco, Inc.)	
Chemistry	Lithium Polymer
Size ($L \times W \times H$)	$12 \times 10 \times 4$ mm^3
Weight	0.95 g
Output Voltage	3.7 V (4.2 V max)
Capacity	30 mAH = 108 C
Energy Density	0.83 kJ/cc

Table 6.7: Battery specifications.

We choose this type of battery for the following reasons:

1. **Rechargeable**: this will allows us to perform many experiments using a single device without having to replace the battery.
2. **Voltage supply**: the relatively high voltage of the Li-Poly batter ensures that we can supply enough voltage to the SoC, measurement circuitry, and LED to function properly.
3. **Voltage fluctuation**: our experimental tests have shown that the Li-Poly battery voltage stays constant regardless of instantaneous current draw, while more common button cell batteries used in watches and hearing aids tend to undergo severe voltage fluctuations for currents exceeding 10 mA.
4. **Flexibility**: Li-Polymer batteries have a chemistry that does not require external pressure to bring their internal layers into contact, and thus do not require an external metal shell [50]. This malleability allows for and increase packing efficiency in a size constrained capsular device.

6.5.2 Voltage Regulators

There are three identical voltage regulators included in the design to decouple the voltage supplies of the EM250 SoC, measurement circuit, and LED drive circuit. The specification is listed in Table 6.8, and circuitry shown in Fig. 6.4.

CMOS Voltage Regulator, LP3985 (National Semiconductor, Inc.)	
Size ($L \times W \times H$)	$1.4 \times 0.9 \times 0.9$ mm^3
Package	5 bump - micro SMD
Input Voltage Range	2.5 - 6 V
Output Voltage	3.3 V
Quiescent Current (shut down)	3 nA
Output Voltage Noise	90 nV/$\sqrt{\text{Hz}}$

Table 6.8: Voltage regulator specifications.

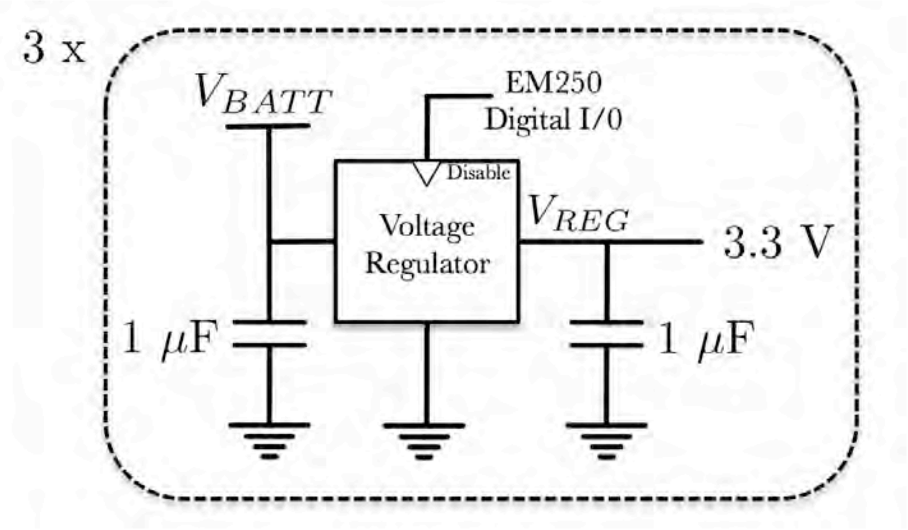

Figure 6.4: Voltage regulator circuitry. The EM250 and LED drive voltage regulators are exactly as shown. The measurement circuitry voltage regulator includes an extra 50/50 voltage divider on the output signal to establish the amplifier non-inverting input reference signal $V_{REF} = V_{REG}/2 = 1.65V$

It has been found that the measurement circuitry is very sensitive to voltage fluctuations due to instantaneous changes in current demand of the LED and microprocessor. Separate voltage regulators are one way to mitigate this effect. Each voltage regulator is connected directly to the battery, and the input and outputs include 1 μF decoupling capacitors. The measurement and LED voltage regulators are disabled when the μC goes into sleep mode by grounding the digital I/O pin connecting the EM250 and the voltage regulator disable. This ensures that the voltage regulator does not consume significant current over long periods of time.

The voltage noise of the voltage regulator (90 nV/$\sqrt{\text{Hz}}$) is comparable to the input voltage noise of the TIA opamp (65 nV/$\sqrt{\text{Hz}}$). However, as we have found in Section 5.5.4, for a properly designed current-to-voltage converter, the input voltage noise contributes negligibly to the total noise compared to other sources, and so the noise of the voltage regulator is does not adversely effect measurement accuracy.

6.5.3 Current Consumption

In Section 4.4 we developed the frame work to quantify the current consumption for the device. The device components can be categorized based on their individual current consumption while awake or asleep, and each stage in the devices operation involves one or more of the subsystems at a time. The current consumption for each relevant electronic component for our device platform is listed in Table 6.9.

System	Variable	Current
Microcontroller (wake)	$I_{\mu C}$	8 mA
Microcontroller (sleep)	I_Q	1 μA
Radio	I_{RADIO}	28 mA
LED	I_{LED}	10 mA
Voltage Regulator (awake)	-	0.1 mA
Voltage Regulator (asleep)	-	3 nA
Opamp power supply	-	7 μA

Table 6.9: Current consumption of the device subsystems.

The current consumption for the voltage regulator and op amp power supply are negligible in comparison with other sources and we do not factor them into the total current drain. As we have seen in Section 4.4, the actual operation of the device can be divided into four stages: data acquisition (DAQ), data transmission, network polling, and sleeping. The time durations of each part of each stage are listed in Table 6.10 using the convention presented in Section 4.4.

Stage	Type	Variable	Value
DAQ	Overhead	Δt_{OH}	72 ms
	LED	Δt_{LED}	5.5 ms
Transmit	Header	Δt_{HD}	16 ms
	Data	Δt_{TX}	2 ms
Poll	Total time	Δt_{POLL}	24.2 ms
	RX/TX	Δt_{PX}	12.2 ms

Table 6.10: Time duration of different stages of the device operation

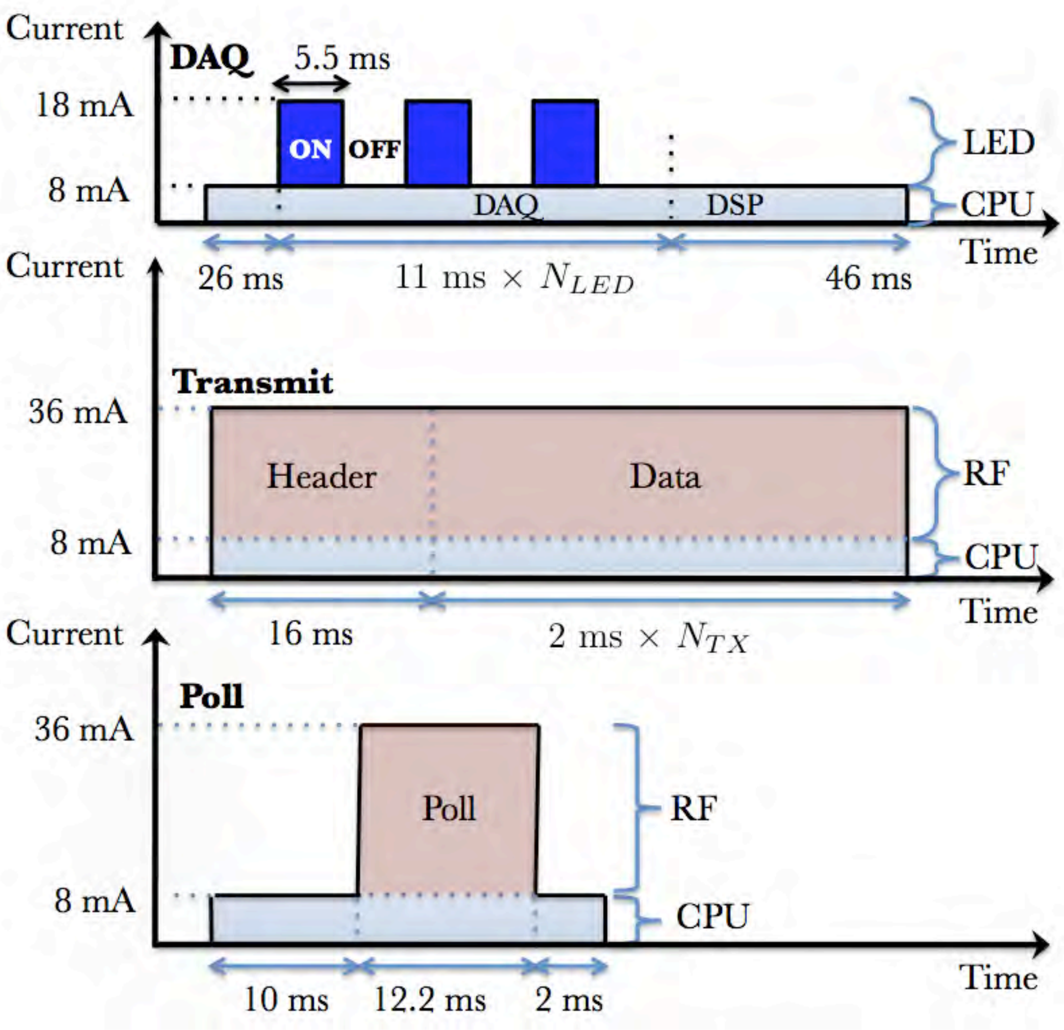

Figure 6.5: Time durations of the different stages of device operation.

Charge and Energy Consumption per Stage

According to Tables 6.9 and 6.10, and using Eq. (4.19) - Eq. (4.19), we calculate the total charge consumed during each stage, which is listed in Table 6.11. The battery voltage is $V_{BATT} = 3.7$ V, and so we also list the corresponding total energy consumption for each stage using $E_n = Q_n \cdot V_n$.

Variable	Charge Consumed	Variable	Energy Consumed
Q_{DAQ}	$576\ \mu\text{C} + N_{LED} \cdot 143\ \mu\text{C}$	E_{DAQ}	2.13 mJ $+ N_{LED} \cdot 0.53$ mJ
Q_{TX}	$576\ \mu\text{C} + N_{TX} \cdot 72\ \mu\text{C}$	E_{TX}	2.13 mJ $+ N_{TX} \cdot 0.27$ mJ
Q_{POLL}	$535\ \mu$C	E_{POLL}	1.98 mJ

Table 6.11: Charge and energy consumed for a single iteration of each stage of device operation. The energy of each stage is $E_n = Q_n \cdot V_{BATT}$

Current and Power Consumption per Stage

The device will perform each stage once, and spend most of the time in a low current sleep mode. The rate with which each stage is entered is f_{DAQ} for data acquisition and transmission, and f_{POLL} for network polling. For the sensor to remain on the network, it must poll once every 1.5 seconds, hence $f_{POLL} = 2/3$ Hz. Thus, the DAQ/Transmission rate is constrained to

$$f_{DAQ} = N_P^{-1} \cdot 2/3 \text{ Hz}, \tag{6.3}$$

where $N_P = f_{POLL}/f_{DAQ}$ is the integer ratio between the polling and DAQ frequencies. With this information we compute the total average current consumed by each stage, and list it in Table 6.12. We also compute the average power consumed by each stage using $\langle P_n \rangle = \langle I_n \rangle \cdot V_{BATT}$.

Variable	Average Current Consumed	Variable	Average Power Consumed
$\langle I_{DAQ} \rangle$	$\frac{1}{N_P}\,(384\ \mu\text{A} + N_{LED} \cdot 95\ \mu\text{A})$	$\langle P_{DAQ} \rangle$	$\frac{1}{N_P}(1.4\ \text{mW} + N_{LED} \cdot 0.4\ \text{mW})$
$\langle I_{TX} \rangle$	$\frac{1}{N_P}\,(384\ \mu\text{A} + N_{TX} \cdot 48\ \mu\text{A})$	$\langle P_{TX} \rangle$	$\frac{1}{N_P}(1.4\ \text{mW} + N_{TX} \cdot 0.2\ \text{mW})$
$\langle I_{POLL} \rangle$	$357\ \mu\text{A}$	$\langle P_{POLL} \rangle$	1.3 mW
$\langle I_{SLEEP} \rangle$	$\approx 1\ \mu\text{A}$	$\langle P_{SLEEP} \rangle$	$3.7\ \mu\text{W}$

Table 6.12: Average current and power consumption for each stage of device operation. The average power consumed by each stage is $\langle P_n \rangle = \langle I_n \rangle \cdot V_{BATT}$

We find that the average sleep current $\langle I_{SLEEP} \rangle$ is negligible compared to the average network polling current $\langle I_{POLL} \rangle$, which for the battery's $Q_{BATT} = 30$ mAH capacity imposes a maximum lifetime of $Q_{BATT}/\langle I_{POLL} \rangle = 3.5$ days, assuming that the device never aquires data or transmits it.

Once data has been acquired and processed on the device, it is only necessary to transmit a single value: the latest measured signal amplitude, and so we set $N_{TX} = 1$. Also, in Section 5.5.4 we set $N_{LED} = 40$ to achieve a small measurement bandwidth. Finally, if we define T_{DAQ} as the time between consecutive DAQ/transmission stages then

$$T_{DAQ} \equiv \frac{1}{f_{DAQ}} = N_P \cdot 1.5\ \text{s.} \tag{6.4}$$

For reasonable value of $N_P = 200$ such that $T_{DAQ} = 5$ min. Between measurements, $\langle I_{DAQ} \rangle = 20.9\ \mu$A, $\langle I_{TX} \rangle = 2.2\ \mu$A, and $\langle I_{TOT} \rangle = 380\ \mu$A, leading to a battery lifetime reduced to 3.3 days. In Fig. 6.6, we show the total battery lifetime vs T_{DAQ}. For any reasonable T_{DAQ} on the order of minutes, the device will be able to function much longer than its usefulness in terms of $T_{LOD} = 11.4$ hours, meaning that power consumption is not a bottleneck for device operation. In principle, we could alter the

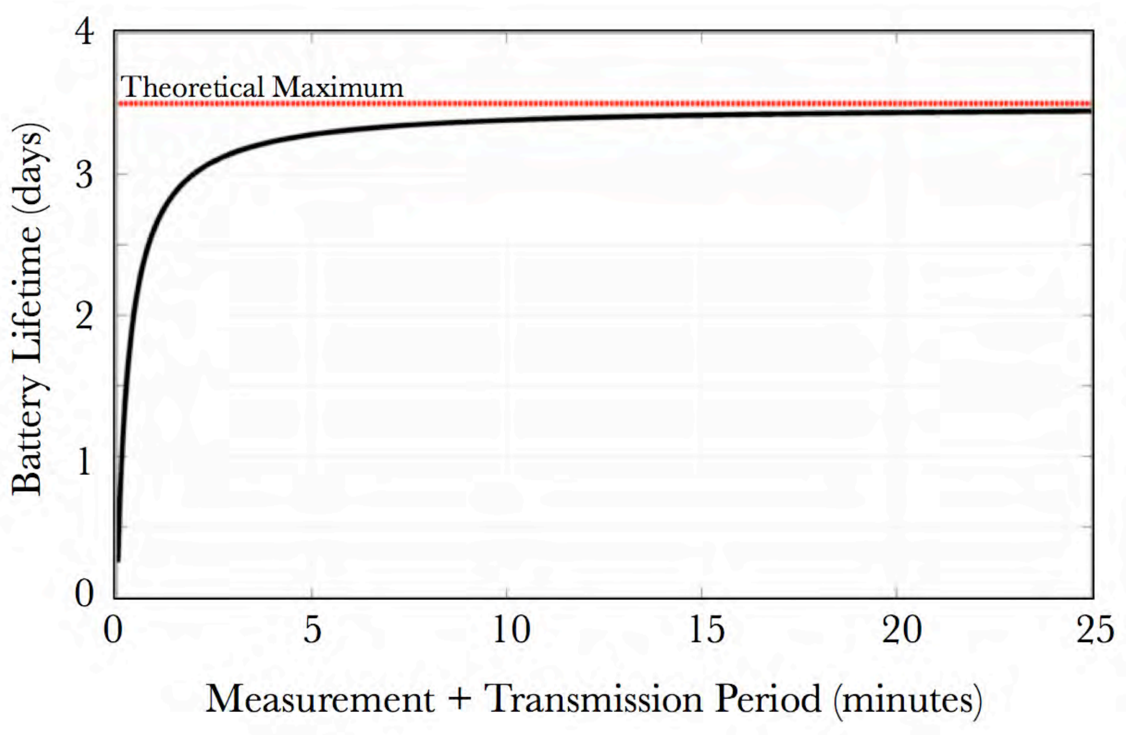

Figure 6.6: Device battery life vs, measurement period

device networking protocol to hibernate without polling for longer periods of time. For example, the device could go into its sleep mode, and lose contact with the network. When the internal sleep timer expires, the device would wake up and re-acquire all network settings (which takes a few seconds). Upon doing so, it could resume normal function. The fundamental upper bound on the lifetime is then limited by the non-zero sleep current $\langle I_{SLEEP} \rangle \approx 1$ μA, and is 3.4 years. This is attractive for very long term medical monitoring, but is outside the scope of our present application.

6.6 Printed Circuit Board Design

The printed circuit board (PCB) is designed to have 4 layers with with an overall thickness of 31 mils and traces formed out of 1 oz copper (Fig. 6.7).

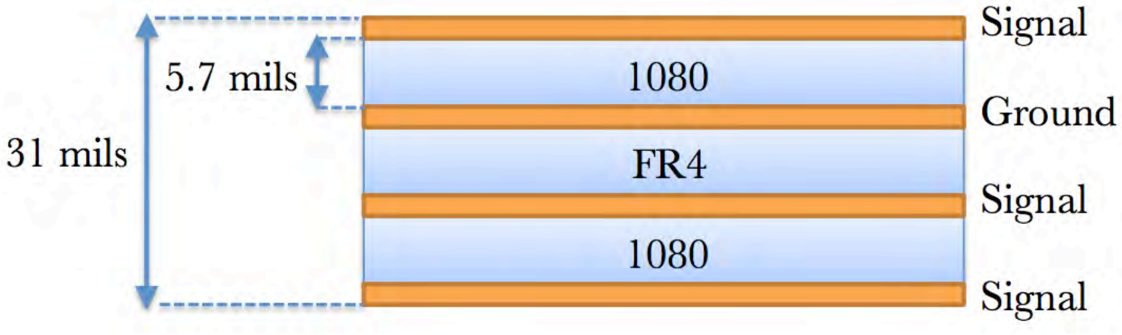

Figure 6.7: PCB stack up.

While the trace widths are not especially important for most of the signals and power routing, it is important to maintain $Z_0 = 50\Omega$ characteristic impedance for all traces in the RF circuitry. The characteristic impedance [51] for a microstrip line is

$$Z_0 = \frac{87}{\sqrt{\epsilon + 1.41}} \ln\left(\frac{5.98\,d}{0.8\,w + t}\right), \tag{6.5}$$

where ϵ is the relative dielectric constant of the dielectric spacer layer, d the distance separating the signal and ground layers, t the thickness of the signal trace, and w the width of the signal trace (Fig. 6.8).

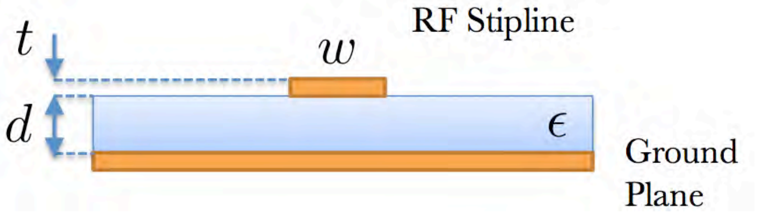

Figure 6.8: Microstrip line geometry.

For $\epsilon = 4.2$ at 2.4 GHz for the 1080 dielectric, $d = 5.7$ mils, and $t = 1.41$ mils for 1 oz copper, we find that the trace width must be $w = 9$ mils to maintain $Z_0 = 50\ \Omega$.

The PCB designs for each layer are shown in Fig. 6.9, Fig. 6.10, Fig. 6.11, and Fig. 6.12. All components are packed as close as possible, with the minimum trace width and trace gap width of 7 mils (0.18 mm). The via holes all have an 8 mil inner diameter and an 18 mil total diameter (0.46 mm). Most passive components are in the 0402 package size (0.4×0.2 mm^2), which is the second smallest package size available for purchase through commercial vendors. The $R_F = 300$ MΩ feedback resistor for the TIA is in the 0805 package size (0.8×0.5 mm^2), and two inductors in the RF circuitry are in the 0603 package size (0.6×0.3 mm^2).

The first (top) layer contains the EM250 SoC, measurement circuitry, voltage regulators, and entire RF front end, along with decoupling capacitors for the EM250. The second layer is designated as exclusively a ground layer. The third layer is for signal routing. The fourth (bottom) layer contains the crystal oscillator and associated passive components, the connection pads for the LED and photodiode from the fluorometer, and the current and voltage driving sources for the LED and measurement amplifiers.

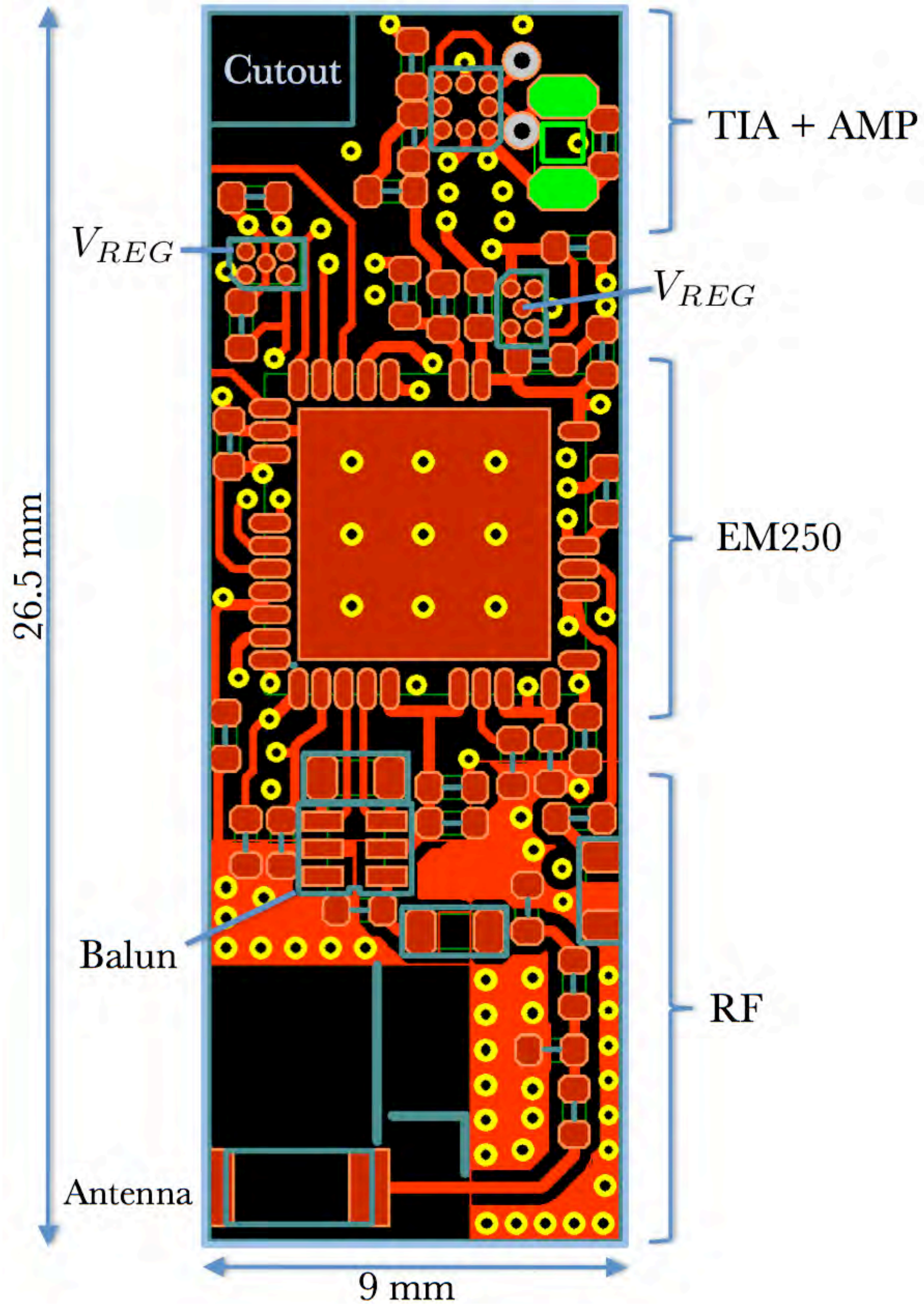

Figure 6.9: PCB top layer design

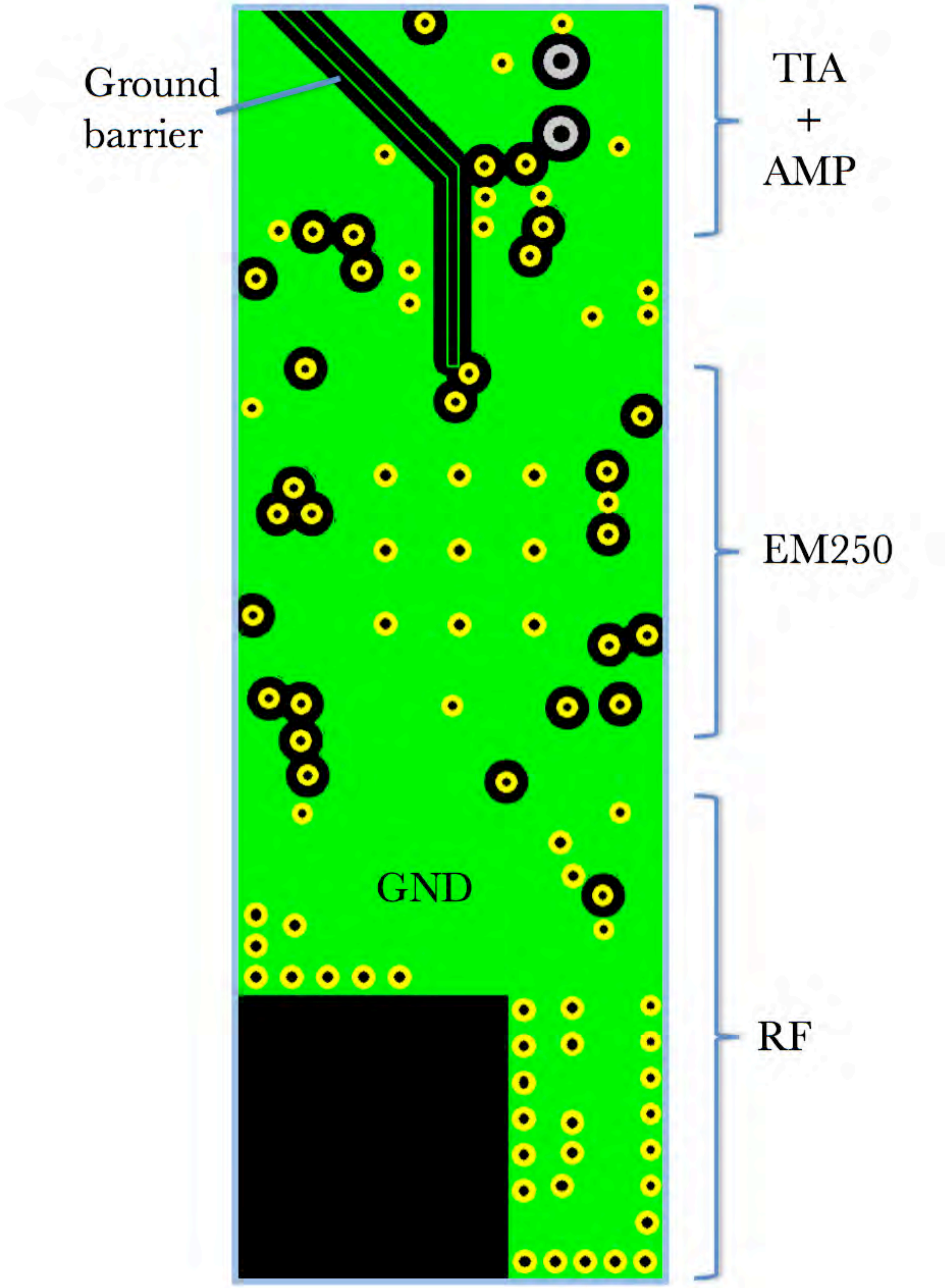

Figure 6.10: PCB ground layer design

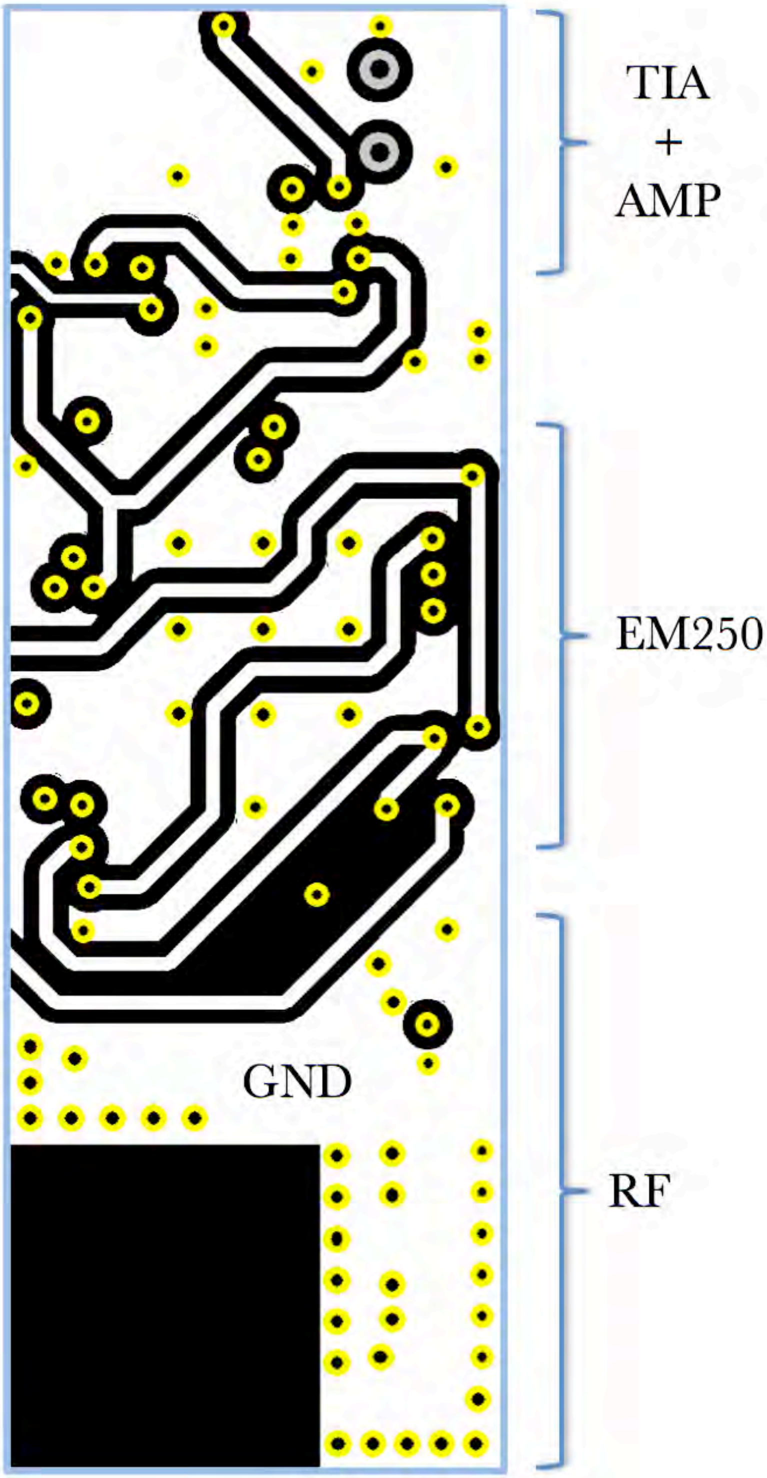

Figure 6.11: PCB signal routing layer design

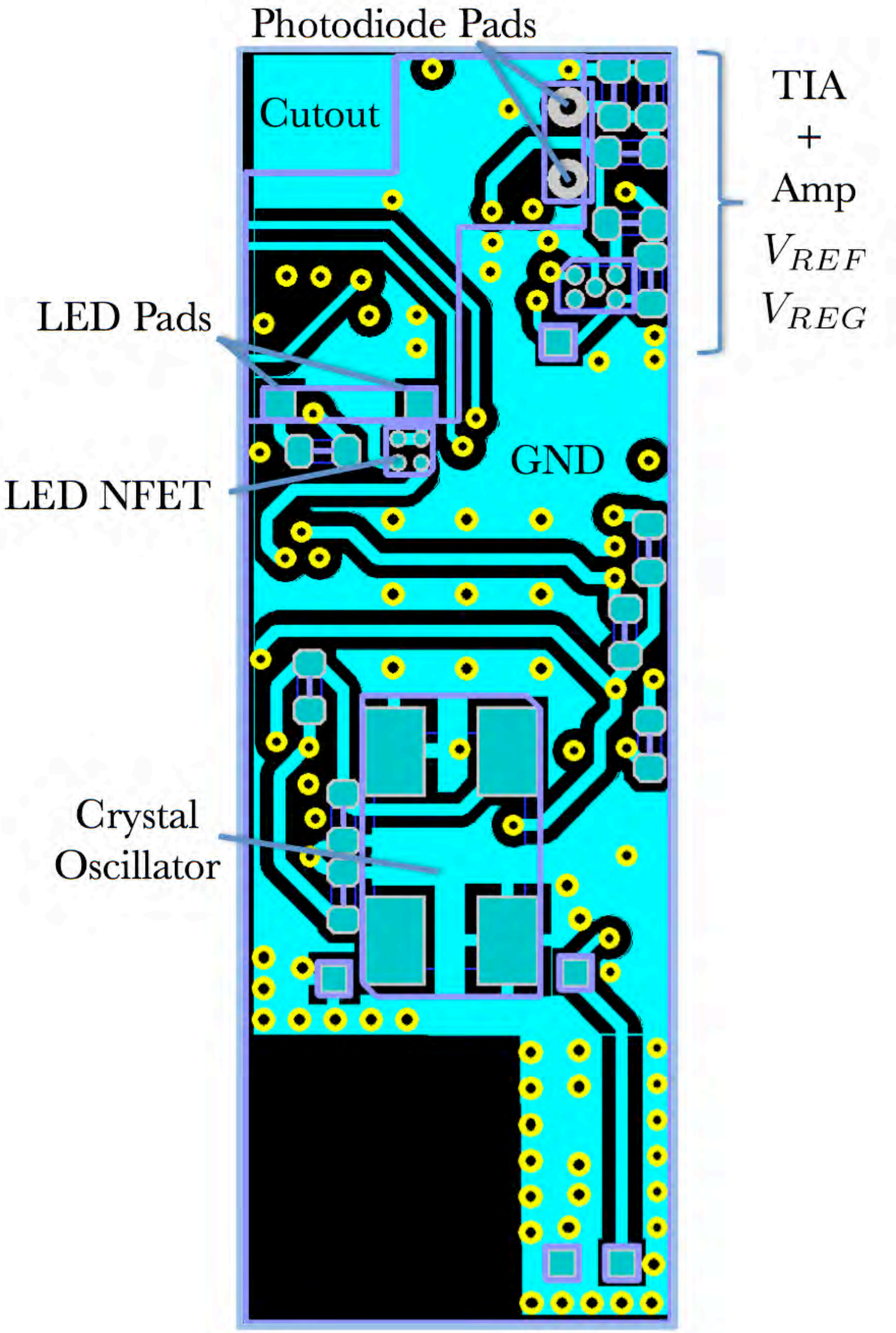

Figure 6.12: PCB Bottom layer design

6.7 Packaging

The device packaging is shown in Fig. 6.13. Shown are the fluorometer, PCB, EM250, antenna, crystal, and battery. The the device is encased in a cylindrical capsule with a 11 mm diameter, 27 mm length, and 0.25 mm wall thickness.

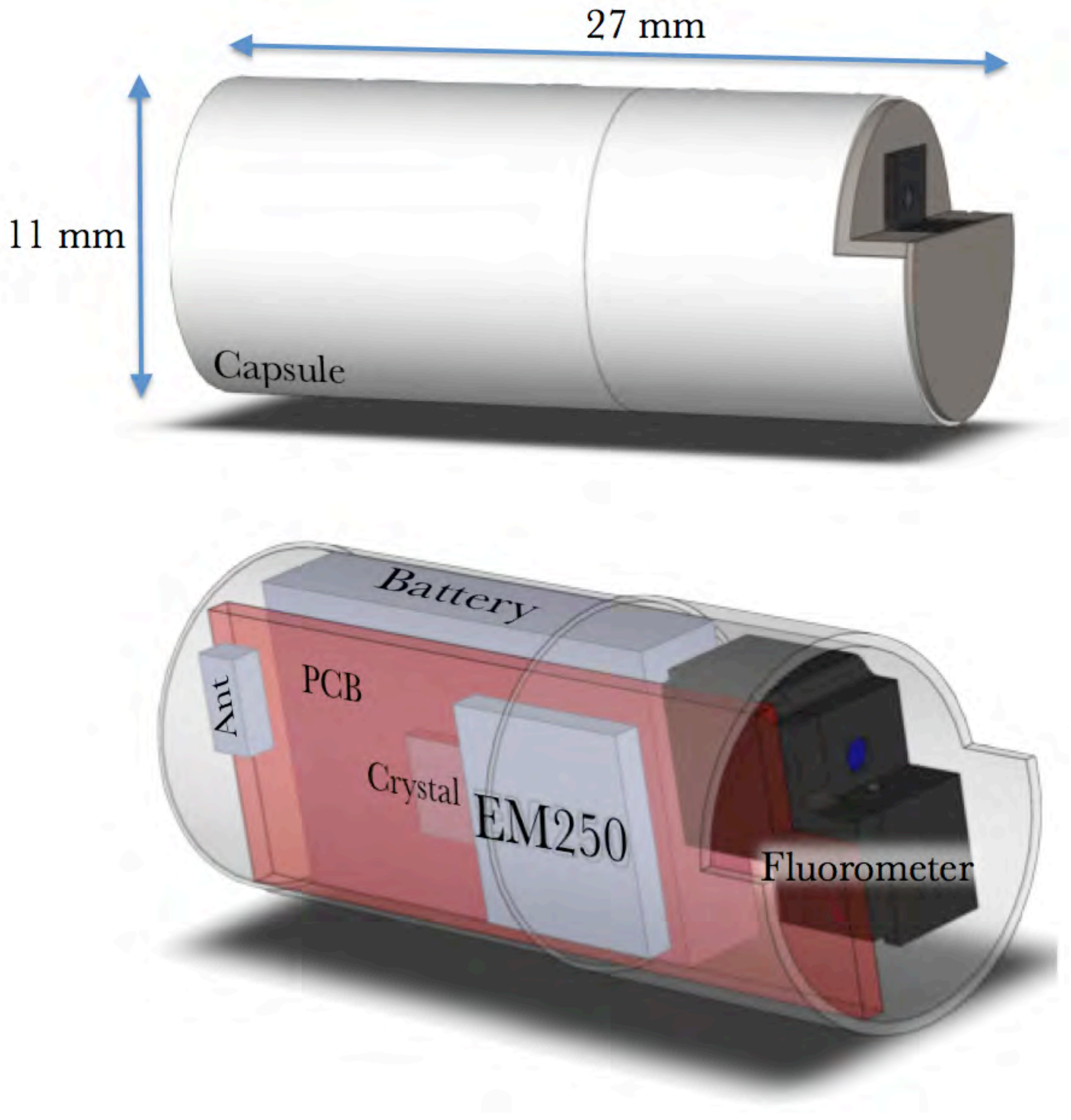

Figure 6.13: caption

6.8 Conclusion

In this chapter, we have presented a hardware platform design based on the Ember EM250 SoC. We have designed the RF, voltage regulator, and LED current drive circuitry. Our analysis of the 2.4 GHz RF link budget has shown that there is enough signal strength to establish a reliable telemetric link between a swallowed capsular device in the stomach and an external monitoring device 30 cm away. We have chosen a battery to power the device, analyzed the power consumption be each subsystem, and concluded that the device can operate for 3.3 days when performing a single measurement and transmission every 5 minutes. Finally, we have presented a 4 - layer PCB design for all the electronics and a packaging design for all the components in a capsular form factor that has an 11 mm diameter and 27 mm length. This concludes the design phase of this thesis.

Chapter 7

Construction of the Lab-in-a-Pill Biosensor

7.1 Introduction

In this chapter, we present the steps involved in constructing a lab-in-a-pill biosensor. We begin by describing the fabrication process for creating the fluorometer (Section 7.2). This involves cutting miniature optical filters, fabricating an optical housing, and then fitting all optical components into the housing to assemble the fluorometer. Next, we describe the process for assembling the electronic circuitry (Section 7.3), which involves a custom printed circuit board that is cut to size, loaded with surface mount components, and programming the μC with custom firmware. We conclude by describing the final lab-in-a-pill assembly (Section 7.4), which involves joining the fluorometer with the PCB, adding a battery power supply, and enclosing the device in a water tight capsule.

7.2 Fluorometer: Fabrication and Assembly

7.2.1 Optical Filter Fabrication

The fluorometer has two optical filters, a low pass excitation filter (NT64-593, Edmund Optics) and an bandpass emission filter (MF525-39, Thorlabs) with sizes listed in Table 7.1.

Filter Type	Thickness (mm)	Diameter (mm)	# of Square Filters
Excitation	1.0	12.5	60
Emission	1.9	25	25

Table 7.1: Excitation and Emission filter sizes.

To fit into the miniature fluorometer, the filters need be cut into small squares. First each large filter is mounted on a silicon wafer with melted wax using a hotplate (Fig. 7.1a and Fig. 7.2a). The wafer with mounted filters is then diced with an automatic diamond saw (DISCO DAD-321) into 1.8×1.8 mm^2 squares to fit into the optical housing shown in Fig. 5.6. After dicing, the wax is re-melted using a hot plate so that the filters can be removed from the wafer. The dicing saw can only cut 1.5 mm deep, and so while the excitation filter is diced all the way through, the emission filter is not (Fig. 7.1b). Therefore, the excitation filter squares can be individually removed from the wafer (Fig. 7.2c), but the emission filter is removed as a solid piece (Fig. 7.2b). The cuts in the emission filter however are deep enough such that it can be carefully broken apart into its constituent filter squares (Fig. 7.2c).

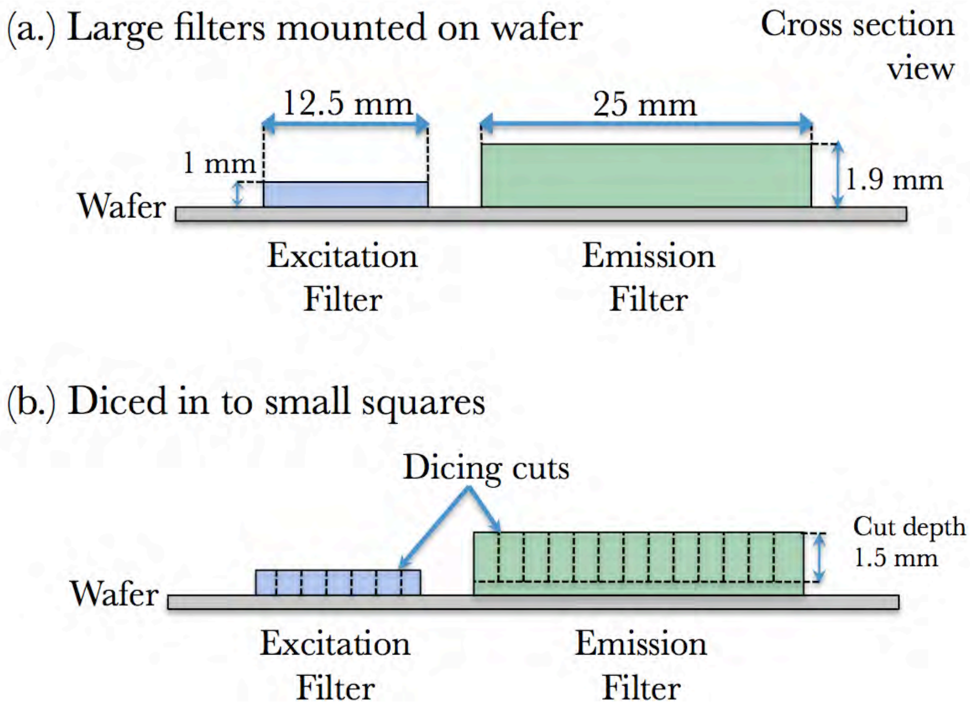

Figure 7.1: (a.) Large filters are mounted on a silicon wafer with melted wax. (b.) Filters are diced in small squares by a diamond dicing saw with a 1.5 mm cut depth.

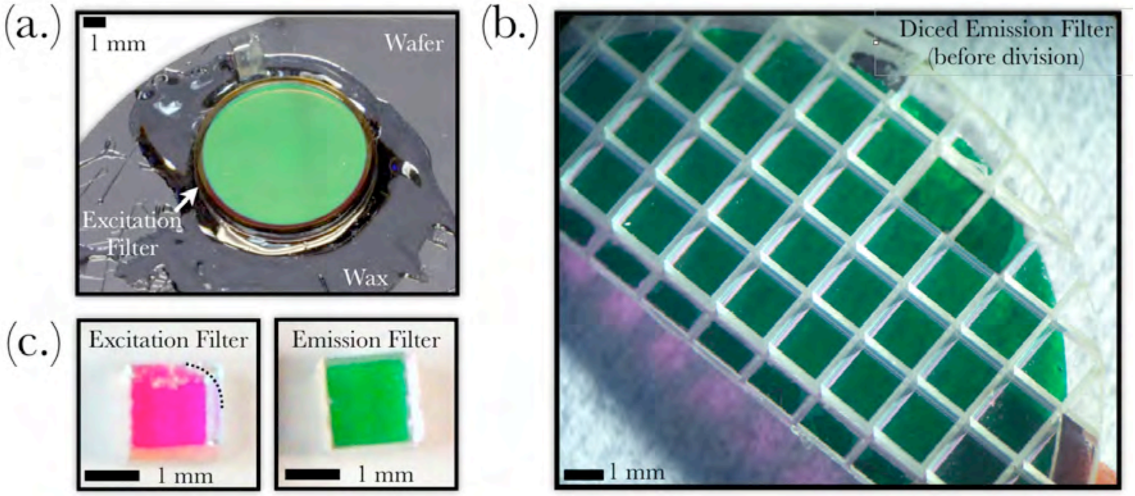

Figure 7.2: (a.) Emission filter mounted on silicon with wax. (b.) Excitation filter after dicing with a 1.5 mm cut depth. (c.) Excitation and emission filter squares after dicing. Emission filter is manually broken apart to form the squares. A corner of the excitation filter is rounded off with a diamond grinding wheel to fit the optical housing

A single corner of each excitation filter square is then rounded off with a diamond wheel saw (Model 650, South Bay Technology, Inc.) to fit into the optical housing (Fig. 7.2c). Each emission filter square's edge is planarized with the grinding wheel to eliminate jagged features incurred during the breaking step of the diced filter.

Finally each filter square is then individually cleaned of wax and debris with a swab soaked in methanol. A single 12.5 mm diameter excitation filter makes 25 squares, and a single 25 mm diameter emission filter makes 60 filter squares.

7.2.2 Optical Housing Fabrication

All optical components of the fluorometer are held together with a housing that is CNC milled[1] out of a 0.125" thick black Delrin acetel thermoplastic sheet (Dupont, US) following the design shown in Fig. 5.6. First the filter slots are milled out with a 0.02" diameter 2-flute square endmill (GR2SI 0.02, Roundtool Labs) at 2800 RPM, and the LED and photodiode slots are milled with a 0.04" diameter 2-flute square endmill (GR2SI 0.02, Roundtool Labs) at 2800 RPM (Fig. 7.3a). Next, the entire housing is cut out of the sheet with the 0.04" endmill. After the housing is cut out, it is mounted vertically (Fig. 7.3b) and the excitation pinholes are drilled with a 0.04" (size #60) micro drill-bit, and the emission pinholes drilled with a 0.02" micro

---

[1] We require a minimum feature size 0.01", which is possible with milling. For comparison, to our knowledge, the smallest feature size offered by commercial 3D printing printing is (0.02")

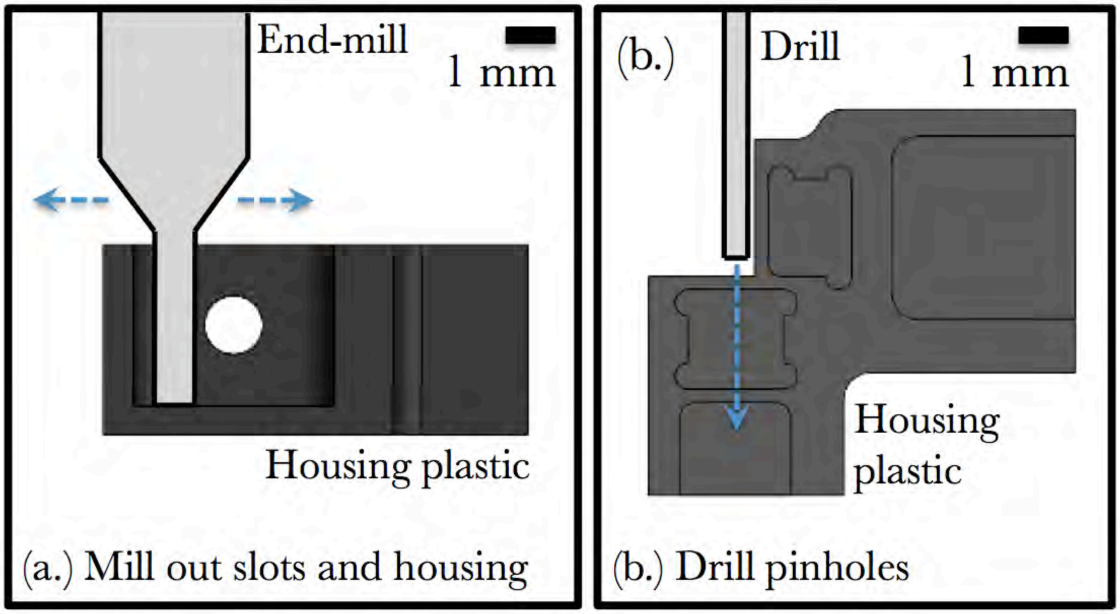

Figure 7.3: Fabrication of the optical housing.

drill bit. Finally, a 0.02” thick housing cover is separately milled out from the same plastic following a similar procedure as the housing.

A photograph of the finished housing is shown in Fig. 7.2a. The cut overshoot seen in the all corners is an unavoidable product of cutting right angles with a round endmill. A photograph of the housing cover after milling is shown in Fig. 7.4b.

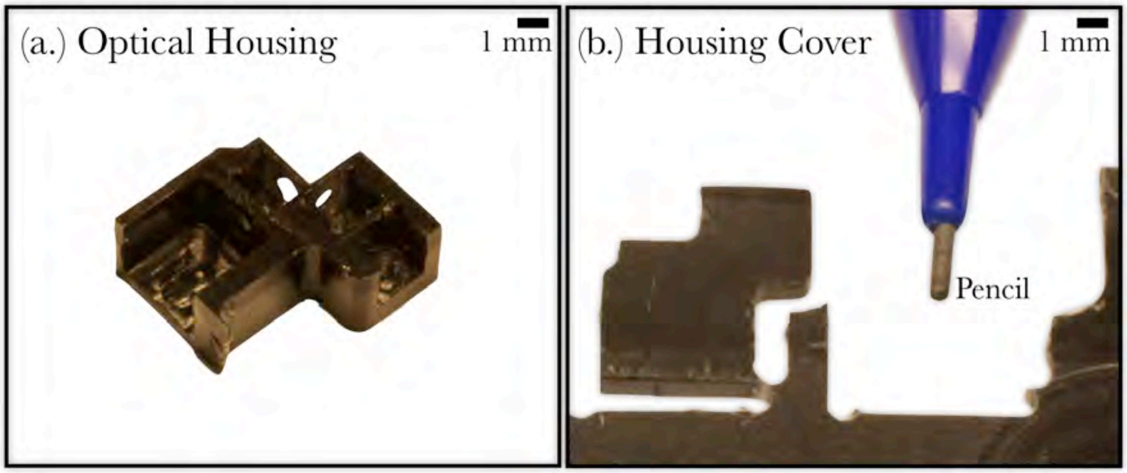

Figure 7.4: Fabricated optical housing and housing cover. In (b.) the housing cover is pictured near a pencil, and shown attached to the plastic sheet after milling. This connection is severed when the cover piece is needed.

7.2.3 Fluorometer Assembly

The fluorometer is assembled out of the following components:

1. **Photodiode** (PDB-C122, Advanced Photonix, Inc.) shown in Fig. 7.5a.
2. **LED** (LB E63C, OSRAM, Inc.) shown in Fig. 7.5a.
3. **Excitation and emission filter squares**, shown in Fig. 7.5c: diced following the procedure in Section 7.2.1
4. **Plastic housing**, shown in Fig. 7.5b, fabricated following the procedure in Section 7.2.2.
5. **Plastic housing cover**, show in Fig. 7.4b, and fabricated following the procedure in Section 7.2.2.

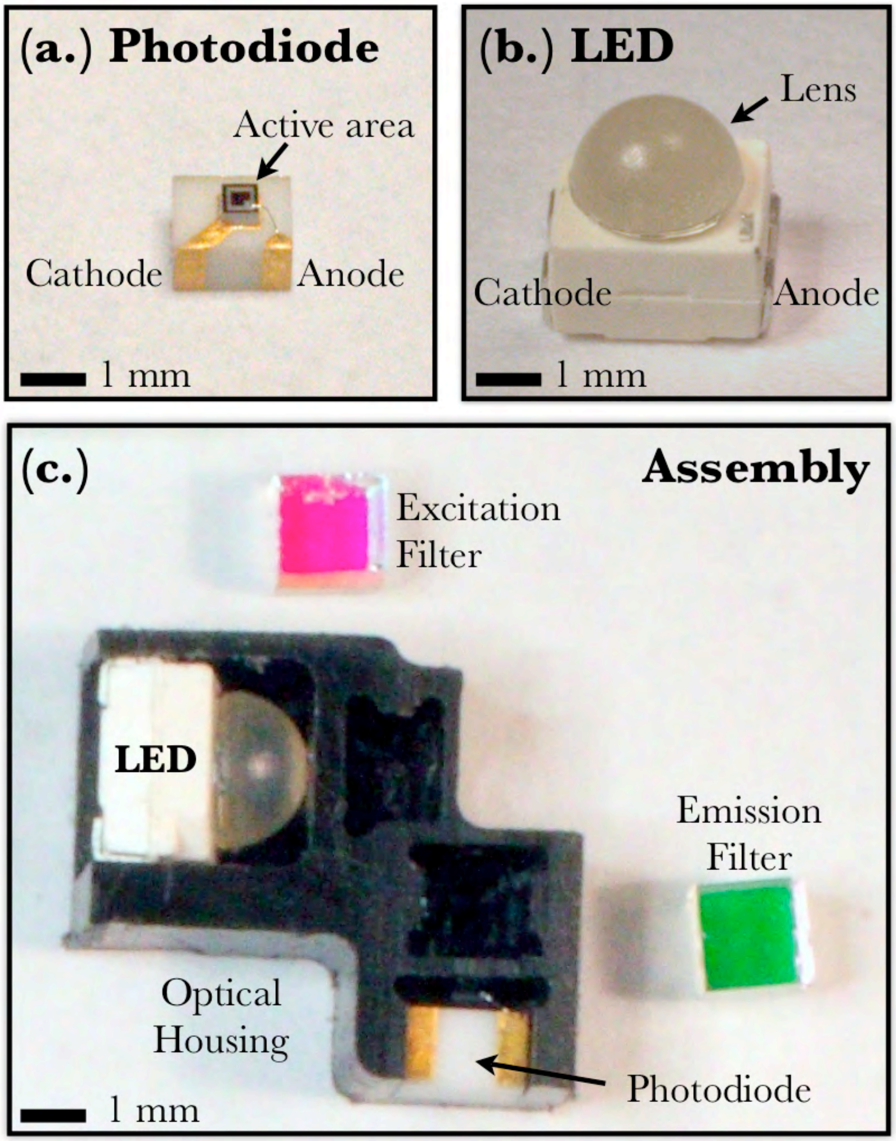

Figure 7.5: Fluorometer components and assembly.

First, the LED and photodiode are inserted into their respective slots (Fig. 7.5c). These two components are fixed in place with a 2-part optically clear epoxy (Bondit-45, Reltek) which is specified for bonding difficult to bond plastics such as Delrin [52]. Before inserting the optical filters, their perimeters are first coated in a thin layer the epoxy to prevent fluid from leaking in through the pinholes. Next, the optical filters are inserted into their respective slots. The epoxy coats the entire filter slot interior, while surface tension prevents it from filling in the pinhole area. We show the assembly at this stage in Fig. 7.6 with the LED lit.

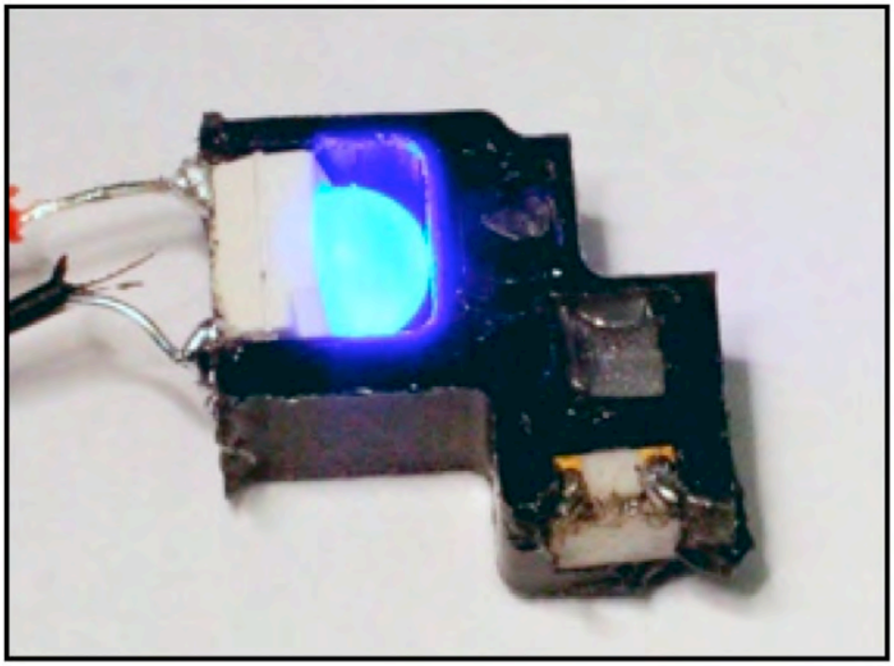

Figure 7.6: Assembled fluorometer (prior to attaching cover), with LED lit.

Next, the housing cover is bonded to the housing with a thin layer of epoxy (Fig. 7.7b). The epoxy remains in a liquid form throughout the entire assembly process (≈ 30 min.). Finally, the entire fluorometer is baked in air on a hot plate at 90°C for 3 hours to cure the epoxy. A photograph of the finished fluorometer assembly is shown in Fig. 7.7. In the inset of Fig. 7.7b, we show the active area of the photodiode as seen through the emission filter pinhole to confirm that it is well aligned with the pinhole.

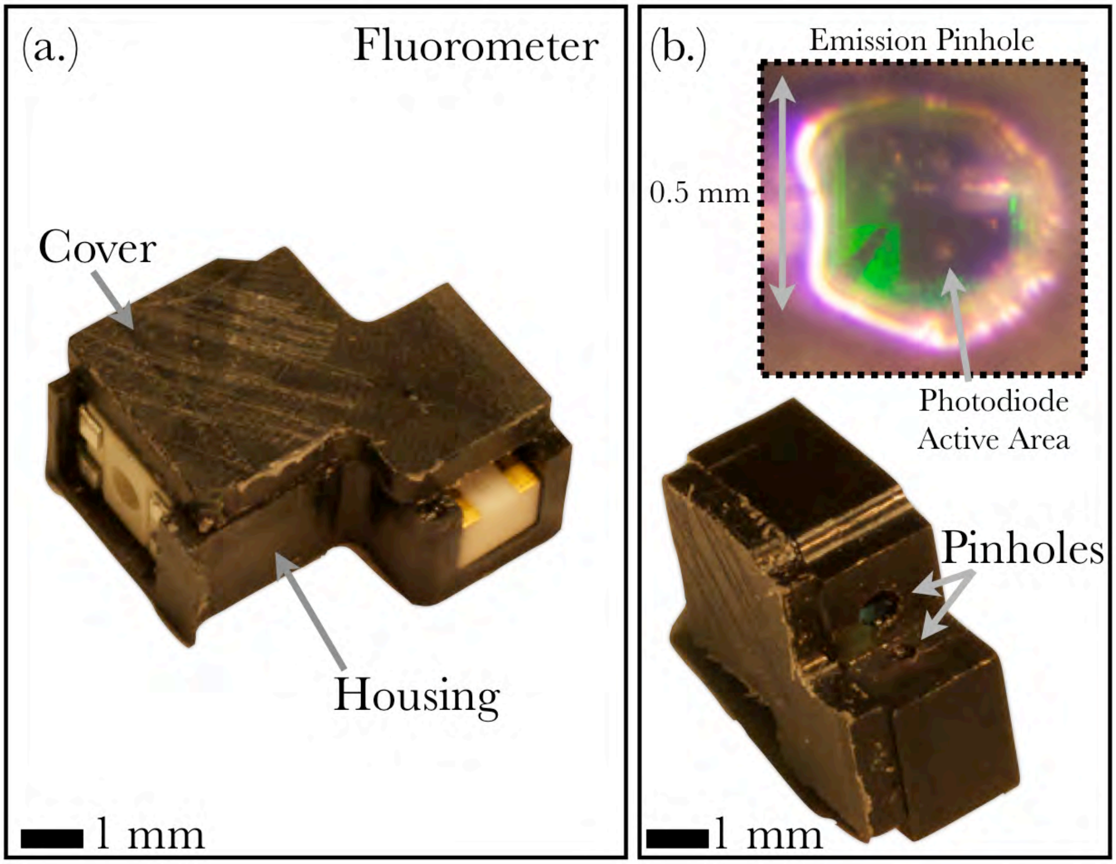

Figure 7.7: (a.) Fully assembled fluorometer. (b.) Different view of the fluorometer. (Inset) A view through the emission pinhole to reveal the proper alignment of the photodiode active area.

7.3 Electronics Fabrication and Programming

7.3.1 Overview

The construction of the electronics is divided into 4 primary steps:

1. Pre-cut the manufactured PCB to size (Section 7.3.2).
2. Assemble all surface mount components and reflow solder paste (Section 7.3.3).
3. Program microcontroller with custom firmware with a computer through a USB connection (Section 7.3.4).
4. Finish cut the PCB to final size (Section 7.3.5).

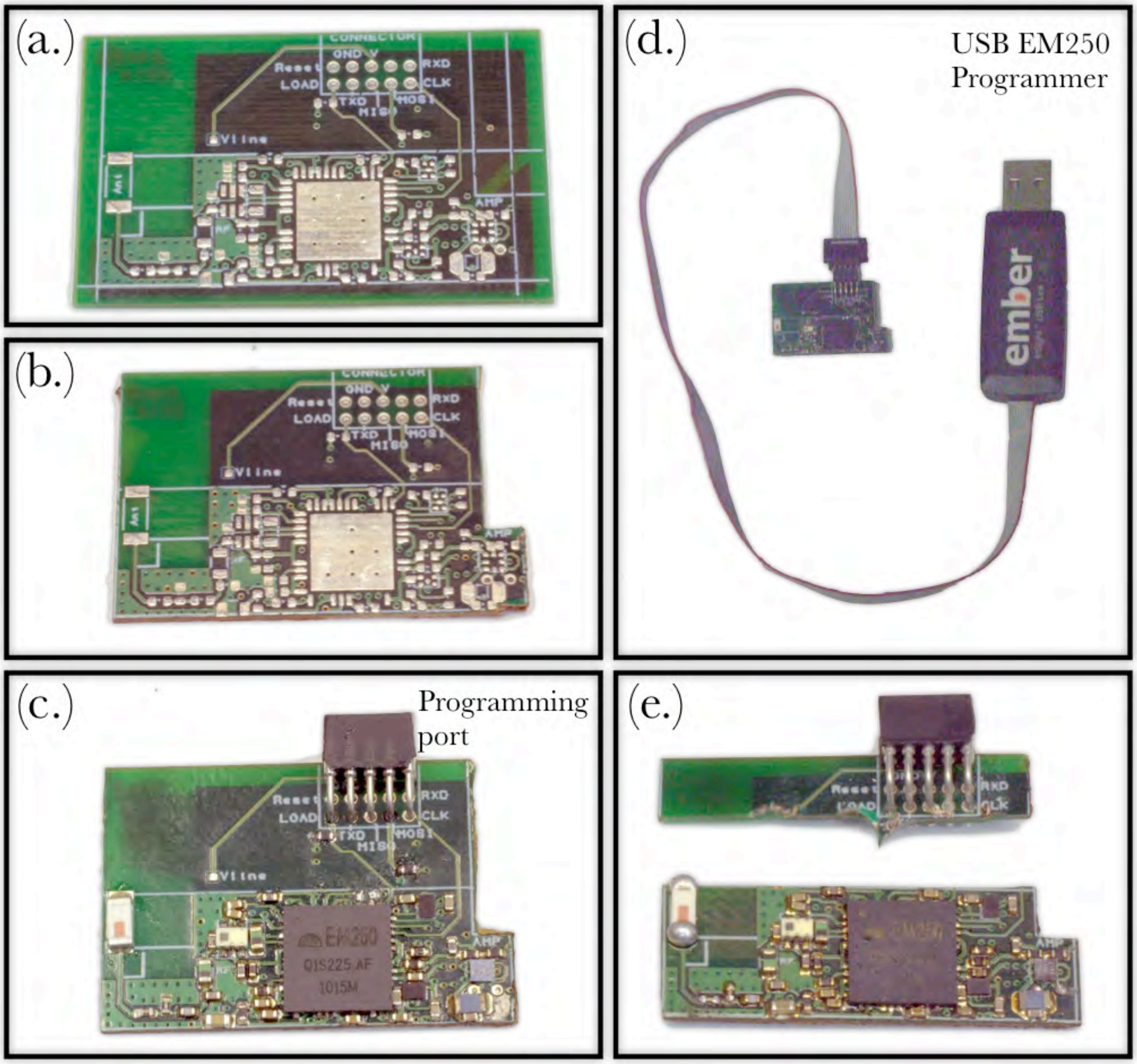

Figure 7.8: PCB fabrication process. (a.) PCB as supplied by the manufacturer. (b.) Pre-cut milling step. (c.) All surface mount components added to PCB and reflowed. (d.) USB programming connector attached to device. (d.) Final cut severs the programming connection and brings the PCB to its final size (9 mm × 26.5 mm).

7.3.2 Printed Circuit Board Pre-Cut

The 4-layer printed circuit board (PCB) is manufactured by Advanced Circuits from the PCB design schematics shown in Section 6.6. In Fig. 7.8a, we show the PCB exactly as it arrives from the manufacturer. The intended PCB size is outlined with the white lines, while the additional traces and pads above the device are for programming the microcontroller, which are cut off after assembly and programming is complete (Section 7.3.5). The design rules specified by the manufacturer impose a 0.04" clearance between the edge of the cut-out PCB and the nearest metal traces, therefore, the PCB needs to be cut-to size fit in the capsular form-factor with a CNC mill. However, milling a PCB with assembled electronics can introduce cracks in the solder joints or components themselves. Therefore, we pre-cut the PCB by perform most of the milling prior to assembling the surface mount components on the PCB (Fig. 7.8b). The PCB is carefully mounted in a vice, and each cut made by a standard 1/8" 2-flute square endmill.

7.3.3 Surface Mount Assembly

The PCB surface mount component assembly is performed under a stereoscope. First, all pads on the top-side of the PCB are coated with a liquid solder paste (Zephpaste SPE-0012, Zephyrtonics. Inc.) applied with a needle. Next, each top-side surface mount component is carefully put in place with tweezers (antenna, SoC, RF circuitry, voltage regulators, opamp package, and passive components). The voltage regulators and opamps have solder bumps on their pads applied by the manufacturer, however, solder paste is still applied to their PCB pads to aid in placement and adhesion. After each component has been put in place the pad alignment is visually verified, and minor misalignments are corrected by careful nudging with the tweezers.

Once the top-side is assembled, the PCB is placed in an infrared reflow oven (T-962, Tai'an Puhui Tech, CO, LTD.) to activate the solder flux, melt the solder, and permanently bond all the components. The reflow temperature profile is shown in Fig. 7.9, and has been experimentally found to reproducibly reflow both the applied solder paste as well as the solder bumps on the voltage regulator and opamp packages.

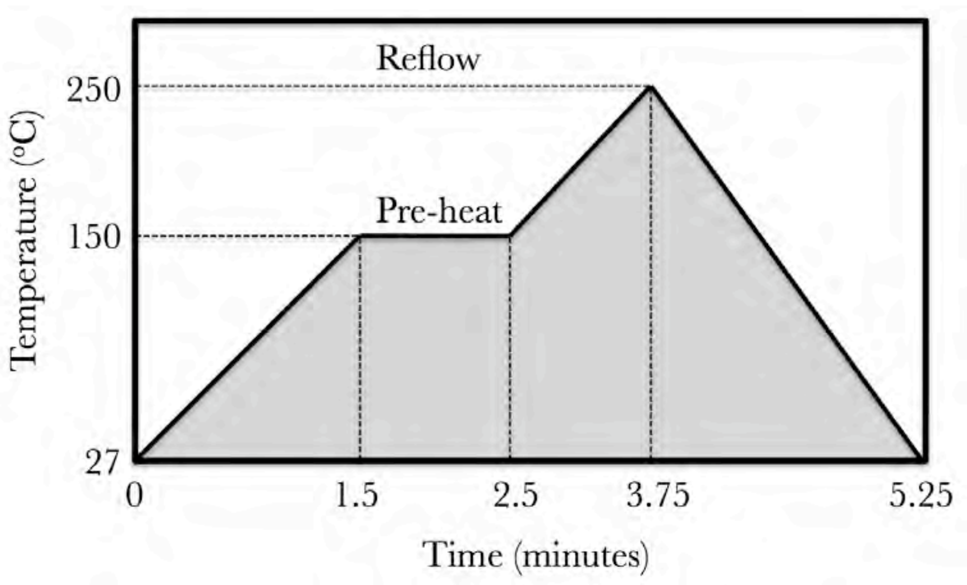

Figure 7.9: Infrared oven reflow profile.

The assembled and reflowed PCB top-side is shown in Fig. 7.8c. After top-side reflow, the bottom-side of the PCB is assembled with the same procedure as the top-side, and subsequently reflowed in the infrared reflow oven with the same temperature profile. Solder bridges that short neighboring pads are mostly eliminated through the surface tension of the solder flux during reflow, any accidental solder-bridges that remain after reflow are manually repaired with a soldering iron. We have found that $\approx 90\%$ of all assembled devices are fully functional at this point in the assembly process. This includes attempts to fix initially unresponsive devices by repairing solder bridges, and re-flowing components.

7.3.4 Device Programming

At this point in the fabrication process, the SoC needs to programmed before the programming connector is cut off to fit the capsular size. The 10 pin (5 pins × 2 rows) programming connector socket is cut from a two row 50 pin (RT ANG 2X50 .050, Millmax, Inc.) right angle socket and and soldered into place (Fig. 7.8c). A proprietary programming cable (Insight USB Link, Ember Corp.) connects the PCB to a computer through a USB connection to allow programming of the EM250 SoC's flash memory with custom firmware designed specifically for our application (Fig. 7.8d).

Device firmware is written in C programming language using a development environment and compiler (xIDE, Ember, Corp) specifically designed for the EM250 SoC. The development environment includes all libraries and files unique to the Ember and Zigbee software stack. The device firmware for the capsular biosensor is based on the "Sleepy-Sensor" reference application supplied in the development kit (Ember, Corp.), and follows the software workflow designed in Section 4.3. The software is then compiled in xIDE and uploaded to the EM250 SoC via the USB cable by the communication software (Insight Desktop, Ember Corp.) supplied in the development kit.

7.3.5 Finish Cut

Before the finish cut is made, the crystal oscillator (pictured in Fig. 7.10b) is removed using a heat gun, because we have found this to be the component most likely to be permanently damaged by the vibration caused by milling the finish cut. Next, the PCB is carefully mounted in a vice and the finish cut is made at 1000 RPM, using a standard 1/8" 2-flute square endmill along the top cut line. The PCB cut to final size is shown in (Fig. 7.8e), along with the severed programming connector. Finally, the crystal oscillator is soldered back into place with a standard soldering iron, and the entire device reflowed one final time in the IR reflow oven (discussed in Section 7.3.3) to repair any cracks that may have developed in the hardened solder joints. We have found that $\sim$ 90% of devices survive this process, which includes all attempts to fix initially unresponsive devices. The final device yield is therefore $\sim$ 80%.

In Fig. 7.10 we show the top and bottom sides of the assembled and reflowed PCB. The final PCB dimensions are 0.3543" (9 mm) × 0.6731" (26.5 mm), and the thickest points including surface mount components is 0.1" (2.54 mm), and occurs at the point where the EM250 SoC and crystal oscillator are aligned.

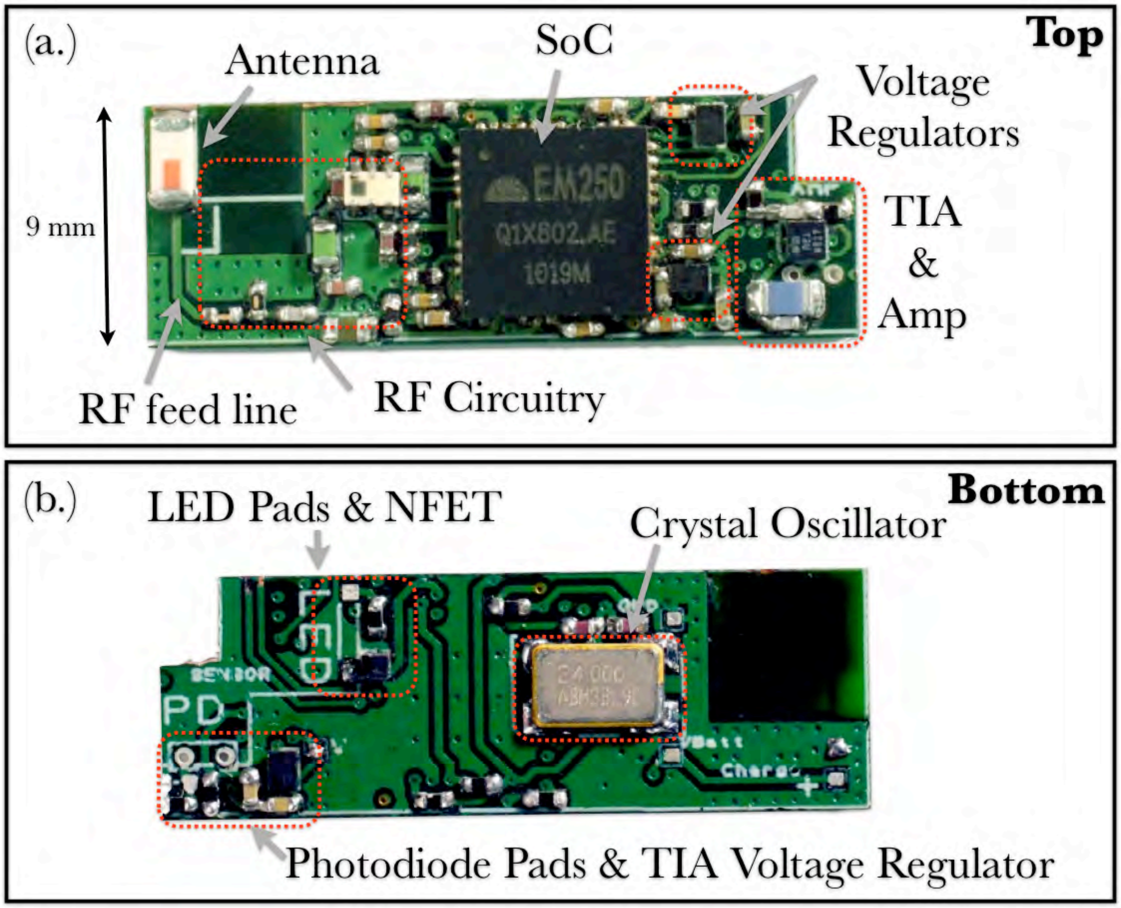

Figure 7.10: (a.) Top view of the assembled and cut PCB. (b.) Bottom view of the PCB.

7.4 Final Assembly and Packaging

7.4.1 Overview

The final assembly steps of the capsular biosensor device are as follows:

1. Mount the fluorometer and battery on the PCB and make a conductive connection between land pads (Section 7.4.2).
2. Connect battery and wrap the device with a insulating layer and a grounded conductive shielding layer (Section 7.4.3).
3. Insert the device into a two part capsule package and seal with teflon tape (Section 7.4.4).

7.4.2 Attaching the Fluorometer and Battery

The housing cover of the assembled fluorometer (Section 7.2.3) is first coated with a thin layer of the epoxy introduced in Section 7.2.3. Next, the fluorometer is mounted on the back-side of the PCB, and aligned with the right-angle PCB cut as shown in Fig. 7.11a. The device is placed on a hot plate and baked in air at 90°C for 3 hours to cure the epoxy. Next, the LED and photodiode are connected to the PCB by manually soldering a short piece of wire between the component pads (two per component) and their corresponding PCB pads, shown in Fig. 7.11b.

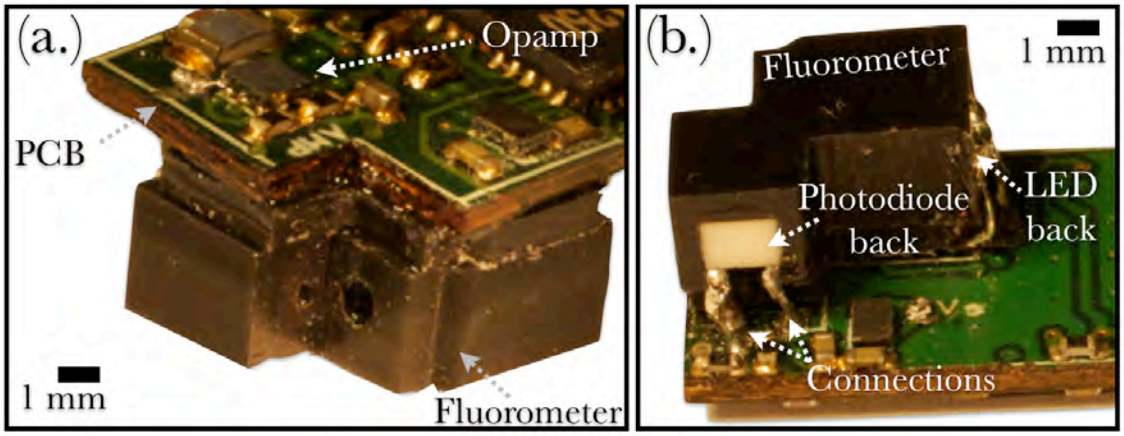

Figure 7.11: (a.) Fluorometer mounted to the PCB with epoxy. (b.) Electrical connections made between the LED, photodiode, and corresponding PCB pads.

The a miniature re-chargeable lithium-polmer battery (LP30-FR, Plantraco, Inc.) is then mounted with Super Glue (Super Glue Corp.) to the back of the PCB onto the crystal oscillator (Fig. 7.12a). A wire is manually soldered to make a connection between the V_{BATT} pad of the PCB and the battery's positive terminal V_+. Separate wires are also manually soldered to the PCB's ground pad V_{GND}, battery's positive terminal V_+, and two to the battery's negative terminal V_-. The battery is charged by connecting the extra V_+ and V_- wires to a battery charger (Plantraco, Inc.) specifically designed for use with the LP30-FR battery. When the battery is fully charged, a solder connection can be made between the PCB's ground pad V_{GND} and V_- to complete the circuit at which point the device is automatically turned on.

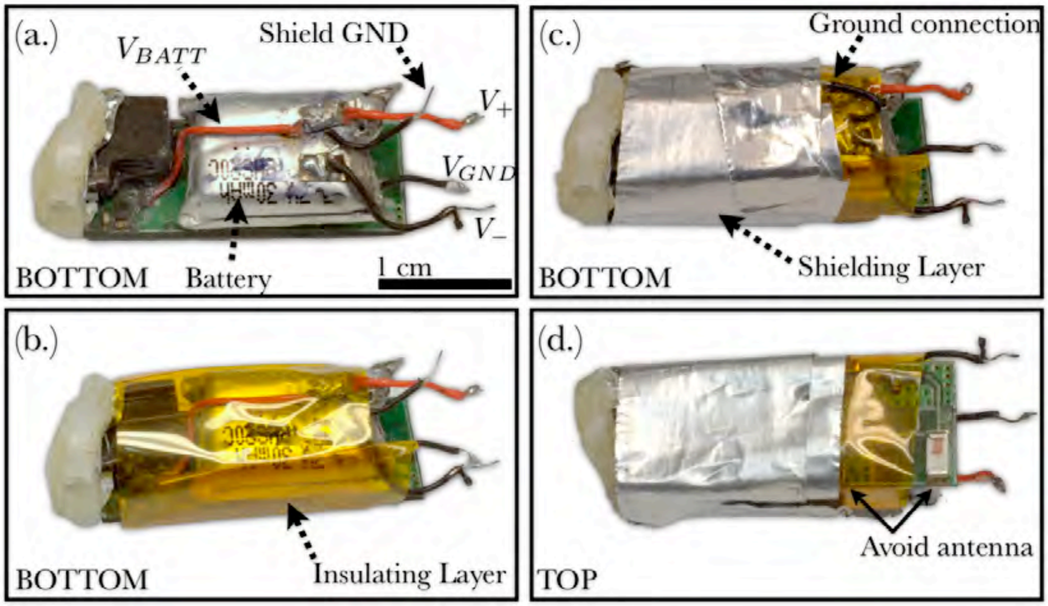

Figure 7.12: (a.) Battery is glued to the bottom side of the PCB and wires attached. (b.) Device is wrapped in a insulating layer of Kapton tape. (c.) Device is wrapped in a conductive sheilding layer of aluminum foil and grounded through a wire to the battery's negative terminal. (d.) Top view of the shielded device, revealing the exposed antenna.

7.4.3 Device Shielding

The device is then wrapped with an insulating layer of Kapton tape, as shown in Fig. 7.12b. Next, the device is wrapped with aluminum foil (Fig. 7.12c), providing a conductive shielding layer which prevents electric interference from external sources to corrupt the highly sensitive measurement electronics. The shielding layer is grounded by taping one of the extra V_- wires to the aluminum foil with a conductive tape; this also secures the shielding layer by preventing it from unwrapping during final assembly. The shielding layer is wrapped in a way which avoids covering the antenna, as this would screen the device's RF communication (Fig. 7.12d).

7.4.4 Capsular Packaging

A cylindrical capsule is fabricated out of a white Delrin acetel thermoplastic rod (Dupont, US). The rod is mounted in a lathe, and a 0.413" (10.5 mm) inner diameter (ID) is drilled and reamed at 1300 RPM. Next, the outer diameter (OD) is carved down to 0.433" (11 mm), forming a wall thickness of .01" (0.25 mm), and 1.043" (26.5 mm) of the the capsule sliced off: these form the final dimensions of the capsule. Finally, the capsule is mounted onto a complementary plastic rod with OD 0.413" and clamped in a vice. A corner is milled out to match the fluorometer and PCB, as seen in Fig. 7.13a.

The capsular end cap is fabricated with the same process, except the ID drilling/reaming step is altered to ensure a depth of 0.65" (16.5 mm). The capsular end cap is then sliced off 0.02" (0.5 mm) past the drilled/reamed depth to form a final length of 0.67" (17 mm), and a 0.02" base.

The PCB with fluorometer and battery is inserted into the capsule and the fluorometer end closed off with epoxy to provide a water-tight seal. The device is again heated on a hotplate at 90° for 3 hours to cure the epoxy. Next the capsule is wrapped in teflon tape to make a water-tight seal with the end-cap. Finally, the capsule and end-cap are joined together (Fig. 7.13b). The final device has a diameter of 11 mm and length of 27mm.

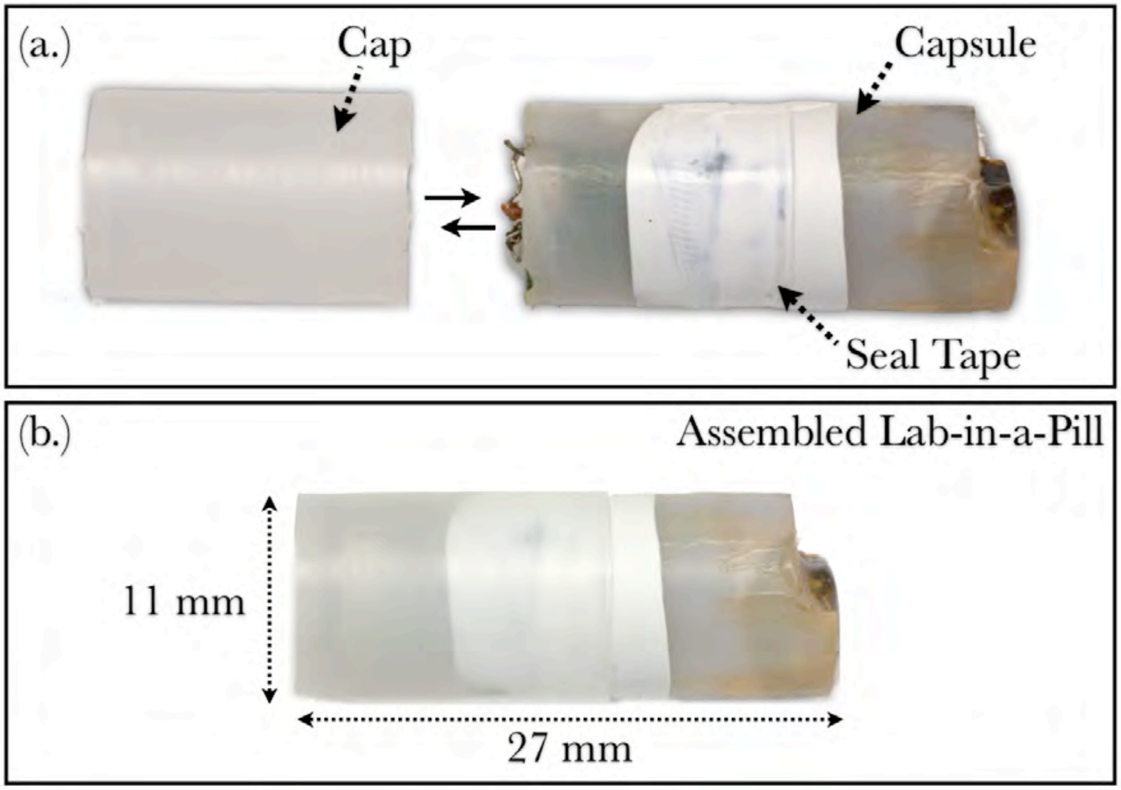

Figure 7.13: Final device assembly. (a.) PCB inserted into capsule and sealed with epoxy. Teflon seal tape is then wrapped at the end-cap connection point. (b.) End cap and capsule joined together.

The device is shown next to a paper clip (Fig. 7.14a) and in a hand (Fig. 7.14b) to provide a sense of scale. Finally, an exploded view of the entire device is shown in Fig. 7.14c.

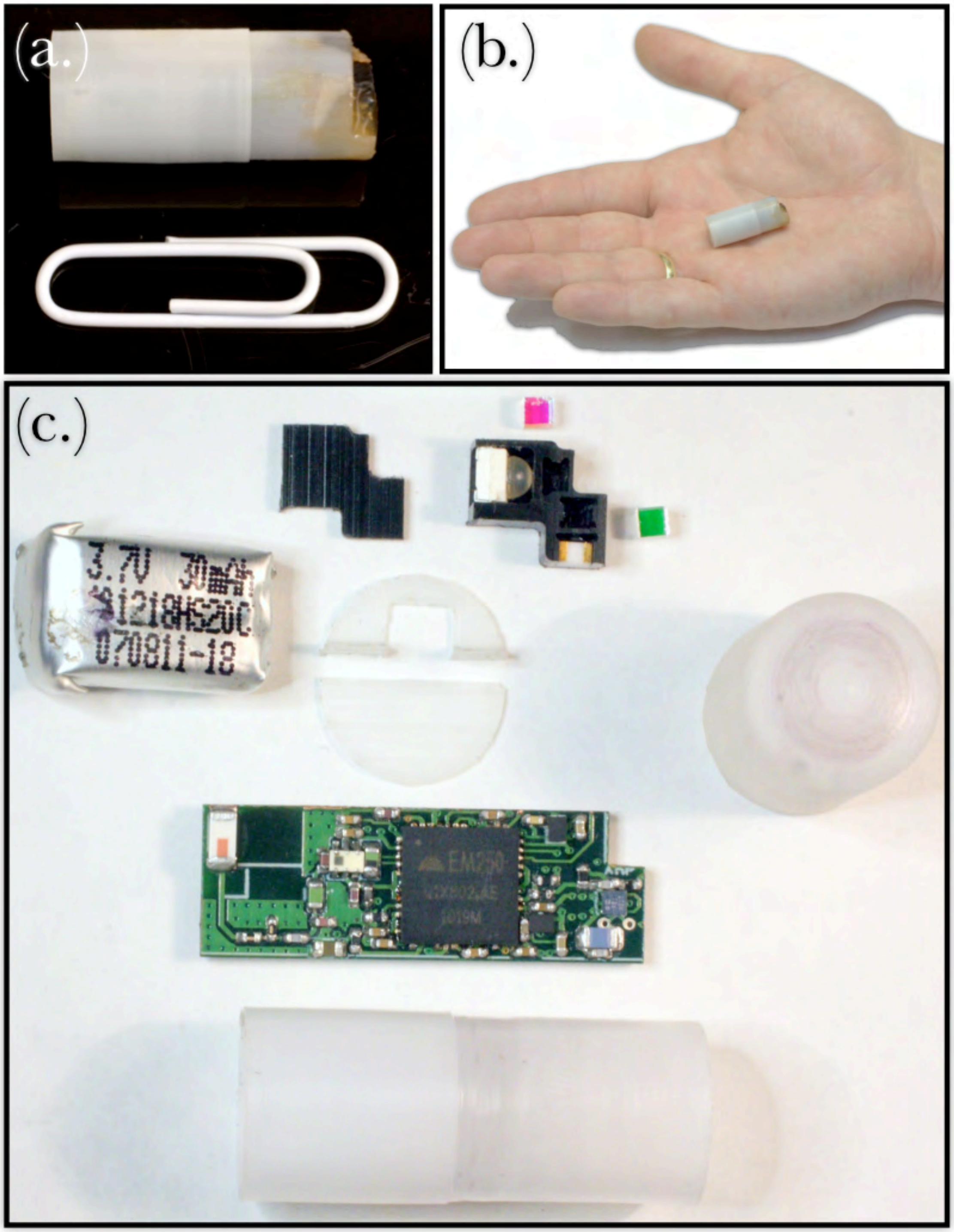

Figure 7.14: (a.) Device next to a paper clip. (b.) Device in a hand. (c.) Exploded view of all device components.

7.5 Conclusion

In this chapter we have detailed the entire process of fabricating and assembling the capsular biosensor that we designed in Chapter 5 and Chapter 6. We described the process of fabricating and assembling the fluorometer, cutting the PCB, surface mount assembly of electronic components, device programming, electric shielding layers, and capsular packaging. The entire device costs $110 in parts, and the entire bill of materials is listed in Appendix A.

Chapter 8

Experimental: Fluorometer and Capsular Biosensor Performance

8.1 Introduction

In this chapter, we perform measurements to characterize the detector performance of the capsular biosensor device. We begin by characterizing the optical spectra of the LED, optical filters, and fluorescence (Section 8.2). Next, we enable the device for wireless streaming, and collect data to characterize the inherent electronic dark noise of the detector (Section 8.3). Finally, we measure the fluorometer sensitivity for detecting fluorescein in water, and demonstrate a characteristic instance of blood detection (Section 8.4).

8.2 Characterizing Fluorometer Optics

8.2.1 Measurement Set-up

The transmission spectra of the filter optics are collected by partially assembling a fluorometer such that it only contains optical filters, and no LED or photodiode. The fluorometer is then fixed with a clamp, and exposed to a white light source (100 W Mercury lamp, Chiu Tech. Corp.). The output spectrum is collected by a 1 mm core step index multimode optical fiber (BFH37-1000, Thorlabs, Inc.) and measured with a spectrometer (HR2000CG-UV-NIR, Ocean Optics, Inc.). The spectrometer outputs data through a USB connection to a computer. The data is recorded and spectra calculated on a computer using SpectraSuite (Ocean Optics, Inc.). This measurement set-up is shown in Fig. 8.1.

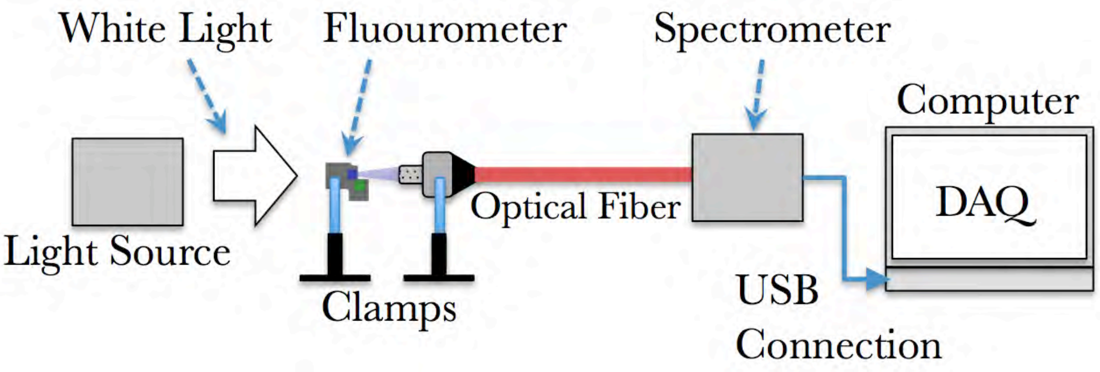

Figure 8.1: Measurement set-up for characterizing optical transmission spectra.

The reference spectrum of the white light source is first found by exposing the fiber aperture directly to the light source. Next, the spectra of each individual filter are found by inserting the fluorometer into the optical path without disturbing the light source or fiber. We use a clamp to fix the fluorometer such that each filter is alternately aligned with the the white light source and the collection fiber, as shown in Fig. 8.2 for each optical filter. The output spectrum is then collected by the optical fiber. The filter transmission is calculated by subtracting the reference spectrum from the filter output spectrum.

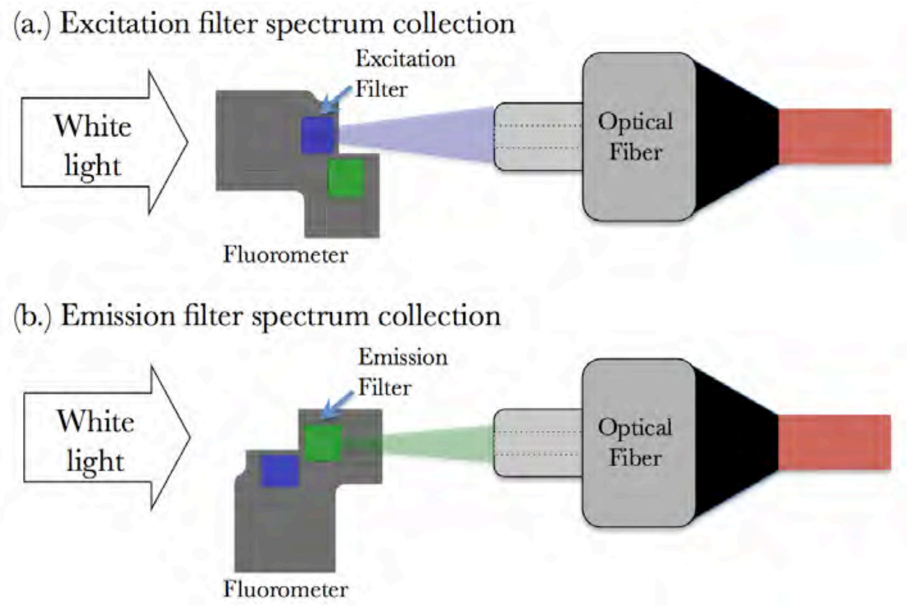

Figure 8.2: Experimental set-up for collection of transmission spectra through the (a) excitation filter and (b) emission filter.

The spectrum of the LED output is collected in a similar fashion. The LED is soldered to a small PCB, and is connected to a 3.3 V supply, which drives the 10 mA current needed to drive the LED. We then collect the LED spectrum as shown in Fig. 8.3a. Next the fluorometer is carefully inserted into the optical path without disturbing the LED, and the LED spectrum that is transmitted by the emission filter is collected as shown in Fig. 8.3a

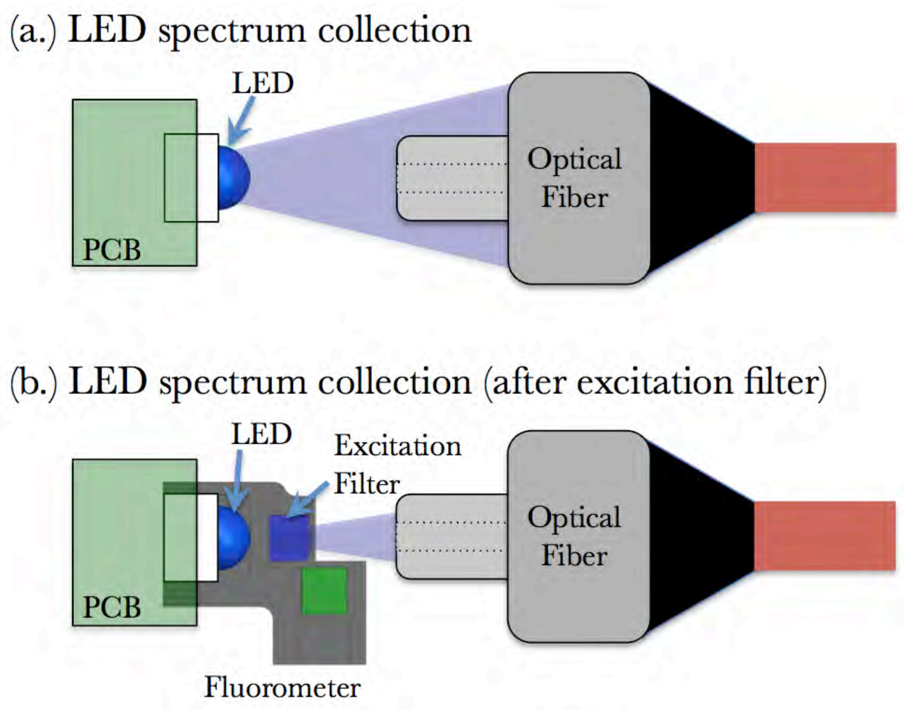

Figure 8.3: Experimental set-up for collection of optical spectrum from the (a) LED and (b) transmitted LED light. LED is soldered to a PCB which supplies the current driving the LED. Fluorometer housing is inserted into optical path to collect light transmitted after the excitation filter.

Next, we collect the emission spectrum of fluorescein by mounting the fluorometer vertically with a clamp, while the LED is attached to the PCB. A droplet of of deionized water with a concentration $C = 10$ μM dissolved fluorescein is placed into the detection volume, and held in place with surface tension. The LED is then lit, and the emission spectrum of the fluorescein is collected with an optical fiber as shown in Fig. 8.4a. To collect the spectrum as detected by the photodiode, we reposition the optical fiber as shown in Fig. 8.4b, and light the LED to collect the emission spectrum that is transmitted by the optical filter. We maintain a constant distance of the fiber aperture to the detection volume in both cases to maintain an equivalent solid angle, so that relative intensities can be compared.

(a.) Fluorescein spectrum collection

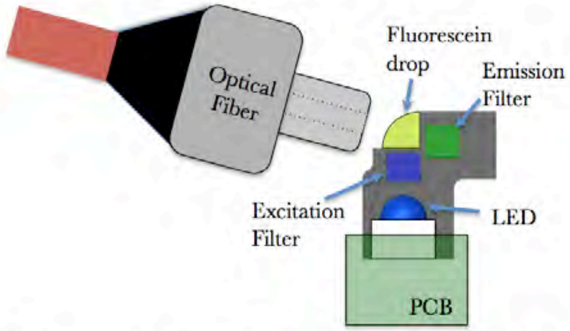

(b.) Fluorescein spectrum collection (after emission filter)

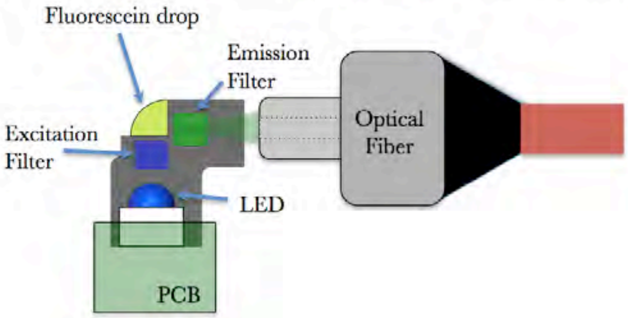

Figure 8.4: Measurement set-up for collecting the fluorescein spectrum.

Finally, we measure the angular spectrum of the emission filter to gauge the effectiveness of the pinholes. We first measure the light source reference spectrum, and then take an uncut emission filter, and insert it in the optical path mounted on a standard 25 mm filter mount. We collect the output spectrum with an optical fiber, as shown in Fig. 8.5. The spectrum is first collected at normal incidence, and then the filter is rotated to $\theta = 17°$, and spectrum collected again. This corresponds to the maximum acceptance angle enforced by the 0.5 mm diameter emission pinholes spaced 1.9 mm apart.

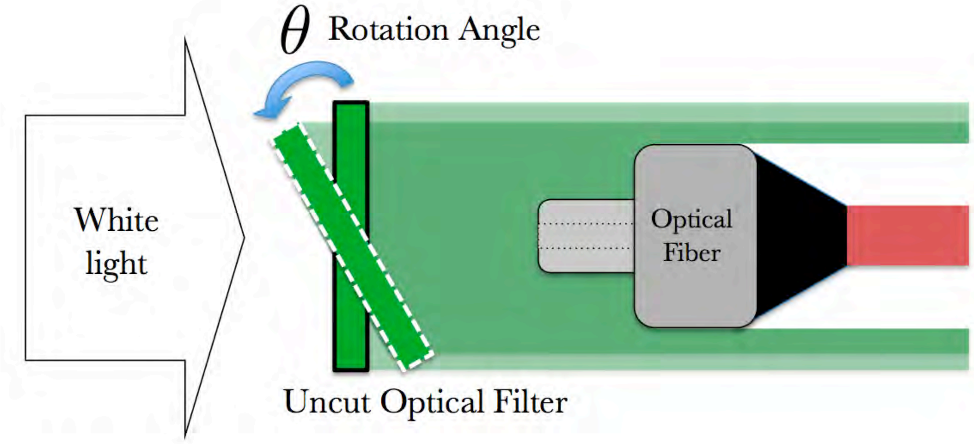

Figure 8.5: Measurement set-up for collecting the angular spectrum of an uncut excitation filter.

8.2.2 Fluorometer Spectral Data

We show the collected spectral data in Fig. 8.6. The LED and fluorescein spectra are normalized to their corresponding unfiltered spectra. We show the unfiltered LED and fluorescein spectra, the transmission spectra of the excitation and emission filters in the fluorometer, and the filtered LED and fluorescein emission spectra as described in Section 8.2.1.

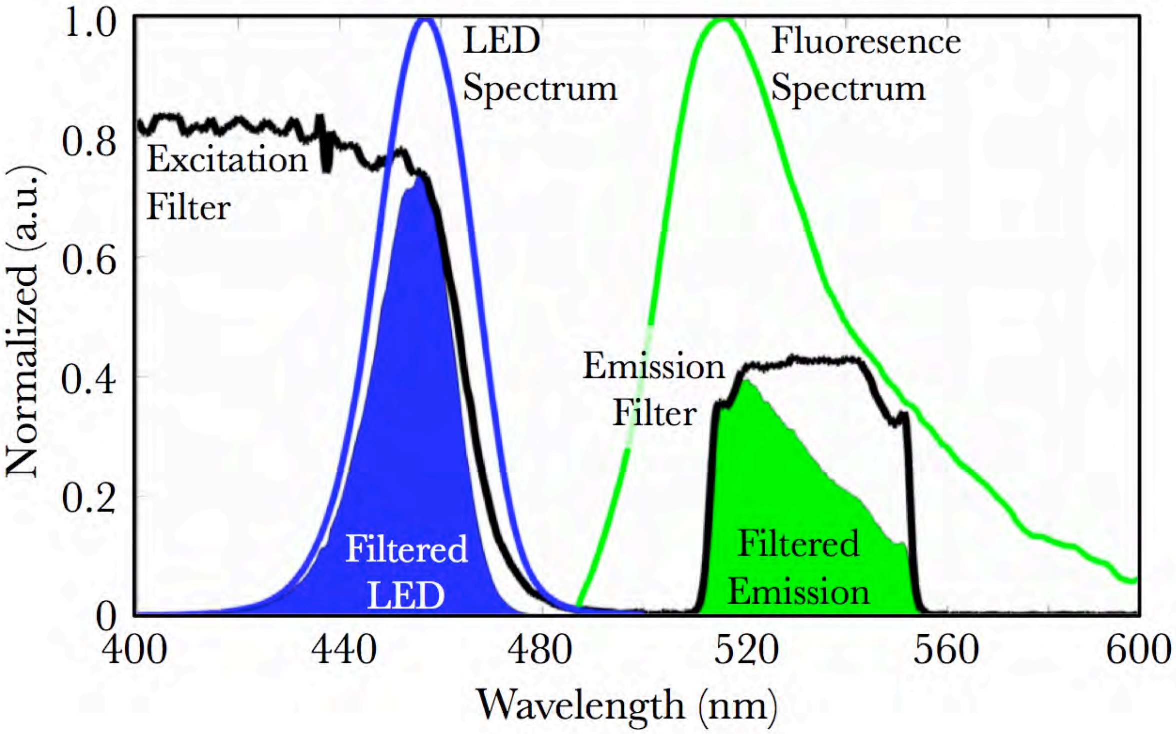

Figure 8.6: Optical transmission spectra of the excitation filter and emission filter, filtered and unfiltered LED excitation spectrum, and filtered and unfiltered fluorescein emission spectrum.

Examining Fig. 8.6 we draw the following relevant conclusions:

1. The excitation filter transmission at $\lambda = 460$ nm is reduced from the 95% for the uncut filter, to 75% for the cut filter. The transmitted power of the LED is reduced from 71.3% (calculated in Section 5.4.4) to 61.1%.
2. The emission filter is red shifted by 15 nm from the expected spectrum, although the 40 nm FWHM passband is preserved. The maximum transmission is reduced from 90% for the uncut filter to 45%, and the total fraction of emission power collected through the emission filter is reduced from 57.4%, (calculated in Section 5.4.4), to 22.3%.

The collected optical spectra suggest that the correction factor ξ_0, calculated in Eq. (5.5), be changed to

$$\xi = \xi_0 \left(\frac{\text{Experimental}}{\text{Theoretical}} \right) = \xi_0 \left(\frac{61.1\% \cdot 22.3\%}{71.3\% \cdot 57.4\%} \right) = 0.332\, \xi_0. \tag{8.1}$$

Expected Fluorometer Sensitivity

Therefore, altering Eq. (5.7) by a factor 0.332, we expect an optical intensity concentration sensitivity of

$$I_{det} = 104\, \frac{\text{fW/mm}^2}{\text{nM}}, \tag{8.2}$$

for low fluorophore concentrations, based purely on collected optical spectra. Using Eq. (5.8), with a detector area $A_{det} = 0.11$ mm^2 and R=0.27, we expect a current sensitivity of

$$I_S = 3.09\, \frac{\text{fA}}{\text{nM}}, \tag{8.3}$$

and, for a predicted input current noise of variance $\sigma_{in} = 10$ fA, a concentration limit of detection

$$I_{LOD} = \frac{I_{SENSE}}{3\,\sigma_{in}} = 9.1 \text{ nM} \tag{8.4}$$

Using Eq. (2.11) we find the that the theoretical time limit of detection T_{LOD} for detecting $V_a = 10$ mL of blood in $V_0 = 1$ L of stomach contents, after injection of $C_0 = 300$ μM of fluorescein at time $t = 0$ is

$$T_{LOD} = 11.7 \text{ hours} \tag{8.5}$$

which is still significantly better than the target time limit of detection $t^0_{LOD} = 4$ hours according to our device specification.

8.2.3 Angular Transmission

Finally, we measure the angular spectrum of the emission filter to gauge the effectiveness of the pinholes. We first measure the spectrum at normal incidence, and then the filter is rotated to $\theta = 17°$, and spectrum collected again, as shown in Fig. 8.5. This rotation corresponds to the maximum acceptance angle enforced by the 0.5 mm diameter emission pinholes spaced 1.9 mm apart. The measured transmission spectrum for normal incidence, where $\theta = 0°$, and $\theta = 17°$, are shown in Fig. 8.7.

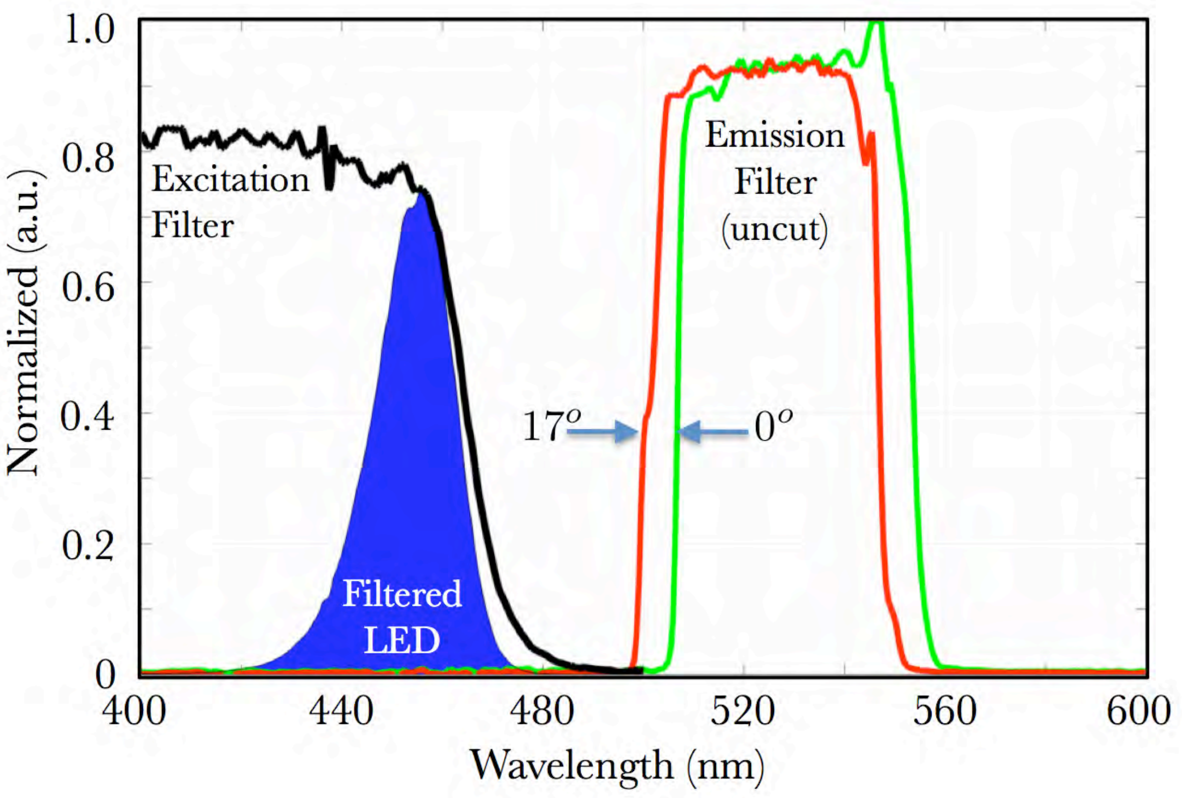

Figure 8.7: Transmission spectrum for uncut emission filter at $\theta = 0^o$ and $\theta = 17^o$. The excitation filter and filtered LED spectrum are shown for comparison.

We also show the spectrum of the filtered LED as a reference. In Section 5.4.2, we calculated that the emission filter pass band should be blue shifted by 10 nm at $\theta = 17°$, relative to normal incidence at $\theta = 0°$. We find experimentally that at $\theta = 17°$, the uncut emission filter passband is blue shifted by 5 nm, relative to $\theta = 17°$, indicating that the pinholes should be effective at filtering out out-of-band light such as LED leak. We believe the discrepancy results from the fact that Eq. (2.12) is only intended to be accurate for small angular deviations.

8.3 Characterizing Fluorometer Electronic Noise

8.3.1 Measurement Wireless Networking

Before measuring the sensitivity of the fluorometer to detecting fluorescein, we measure the input electronic dark noise. The assembled sensor is first fully charged using a battery charger. Next the sensor is disconnected from the battery, and connection made between the the V_+ and V_{BATT} pads to activate the device (defined in Fig. 7.12). A single wireless Zigbee transceiver in a USB stick form factor (ETRX2, Telegesis Inc.) serves as the network coordinator and parent device for the capsular sensor end-device (discussed in Section 4.2.3), thereby fulfilling the role of the external monitor.

Figure 8.8: Zigbee USB transceiver based on the EM250 SoC.

The USB monitor contains the same EM250 SoC as the capsular biosensor device, and is programmed over a virtual serial interface through the USB port with custom firmware written in the C programming language in the xIDE development environment (Ember, Corp.) and uploaded through InSight Desktop (Ember, Corp.). As soon as the USB monitor device is plugged into the measurement computer, and capsular device is turned on, they both announce their roles in the Zigbee network by exchanging corresponding Zigbee packets: this process is completely automated through the Zigbee stack libraries supplied by Ember for use with the EM250, and is part of the firmware uploaded in Section 7.3.4. Once the capsular device MAC address is recognized (it is hardcoded into the Zigbee/USB device), the capsular device automatically begins to stream data to the Zigbee/USB monitor following the software work flow specified in Section 4.3.

Furthermore, when changes need to made to the device firmware, the new firmware is updated wirelessly over-the-air using InSight Desktop through the USB monitor device. However, the initial firmware load must be made through the wired connection discussed in Section 7.3.4 because the firmware libraries enabling over-the-air updating are not preloaded on the EM250.

8.3.2 Measurement Set-Up

The measurement set-up is shown in Fig. 8.9. Once the capsular device and USB monitor are activated they automatically form a wireless connection as discussed in

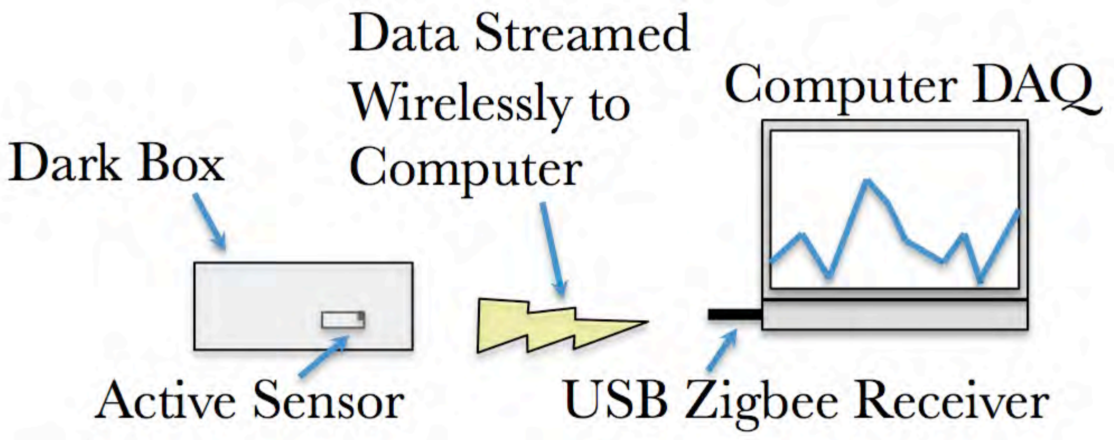

Figure 8.9: Measurement set-up for wirelessly acquiring data from the capsular biosensor.

the previous section. The measurement computer uses custom MATLAB (Mathworks, Inc.) data acquisition software specifically written for this application. The software communicates with the USB monitor through a virtual serial port interface, and each data point transmitted by the capsular sensor is routed to and recorded by MATLAB software through the USB monitor. The capsular device is placed on a wooden table $\approx$ 1 m away from the USB monitor and continuously streams acquired data. The fluorometer is sensitive to white light from the room lights and computer monitor, and therefore, a small cardboard box is place over the device, and room light turned off to minimize this effect.

8.3.3 Noise Measurement

Before Digital Filtering

The MATLAB DAQ program first sends a command to the capsular device to disable the LED and DSP filter so that the raw dark noise data is streamed to the computer as it is input to the ADC. The ADC samples N = 18 points of data at f_s = 1.65 kHz during each DAQ cycle, which occurs with a 3 second period following the sequence shown in Fig. 4.9. Every time a new batch of data is received by the computer, it is concatenated with all previous raw data. Finally, after L = 7002 total data points (389 consecutive DAQ cycles) were collected, we perform an L-point discrete fourier transform (dFT) on the acquired data. The experimental input referred current noise i_{exp} is thus,

$$i_{exp} = \text{dFT[RAW DATA]} \cdot \sqrt{\frac{2}{L\,\Delta f_{RBW}}} \cdot \left(\frac{1}{H}\right), \tag{8.6}$$

where we define the dFT frequency bin resolution bandwidth (RBW) to be

$$\Delta f_{RBW} = \frac{f_s}{L} = 0.24 \text{ Hz}, \tag{8.7}$$

for the L-point dFT sampling at a frequency f_s, and H defined in Eq. (8.8). The second term in Eq. (8.6) scales the raw dFT to reflect the noise measured in a 1 Hz bandwidth, and the factor of $\sqrt{2}$ collapses the positive and negative amplitude spectrum into a single positive spectrum (discussed in Section 3.3.2). The last term in Eq. (8.6) transfers the measured voltage noise spectrum as sampled by the ADC, into an input current noise spectrum, where H is defined as the full circuit current transfer function, and is found to be

$$H = 2 \cdot \frac{1}{100} \cdot \frac{1}{330\,\mu\text{V/pA}} = 0.061\,\frac{\text{pA}}{\text{mV}} \tag{8.8}$$

which can be found by tracing the the data acquisition circuit path shown in of Fig. 5.7 in reverse, from the ADC input to photodiode input.

The measured input current noise spectrum i_{exp} is shown in Fig. 8.10, along with the theoretical input referred current noise spectrum i_{th} as calculated in Section 5.5.4. We also show a 50 point moving average smoothing filter performed on the acquired frequency spectrum to help better see the correspondence between the measured noise spectrum and the experimental noise spectrum.

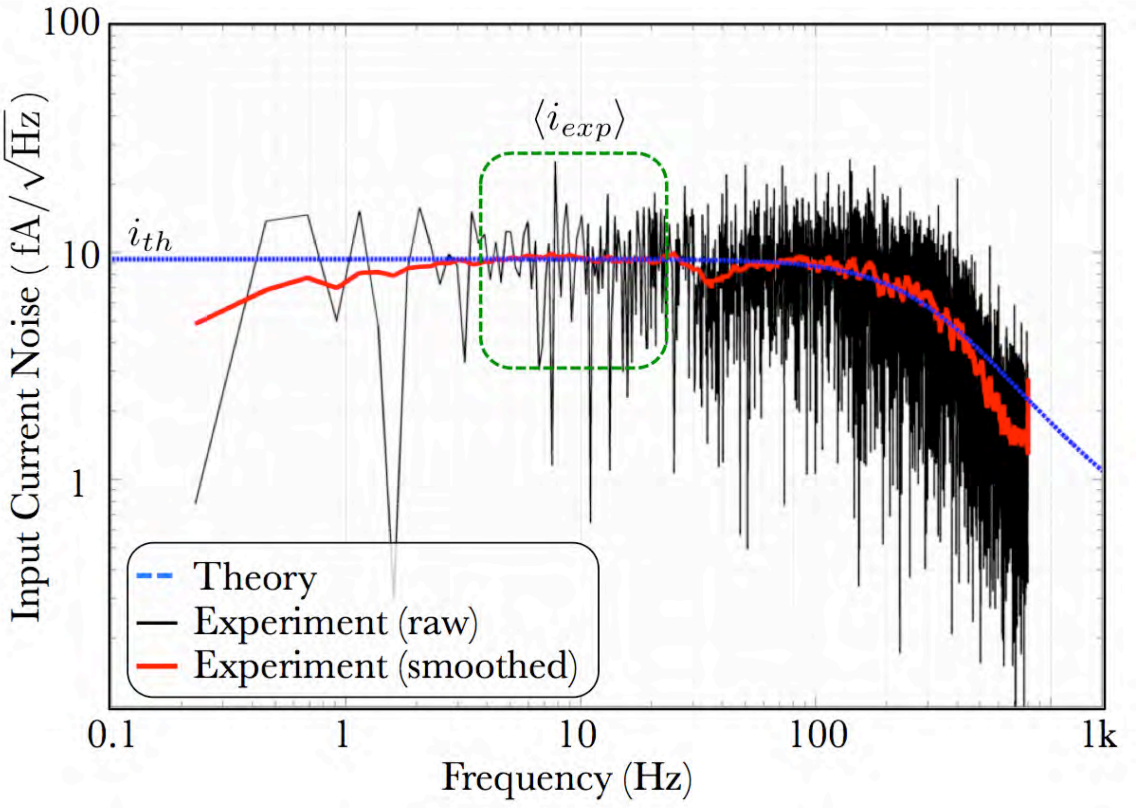

Figure 8.10: Experimental and theoretical input referred current noise. A 50-point smoothed version of the experimental data is shown in red.

The acquired noise spectrum appears to correspond well to the theoretical spectrum. We choose a low frequency flat region of the spectrum to compare to the theory (green box in Fig. 8.10), and find that in a 10 Hz bandwidth of the input current noise around $f = 10$ Hz, the average current noise spectral density is

$$\langle i_{exp} \rangle = 9.35 \frac{\mathrm{fA}}{\sqrt{\mathrm{Hz}}}. \tag{8.9}$$

We compare this to the theoretical input white current noise,

$$\langle i_{th} \rangle = 9.33 \frac{\mathrm{fA}}{\sqrt{\mathrm{Hz}}}, \tag{8.10}$$

found in Section 5.5.4, and find excellent agreement the expected noise spectrum.

Using Eq. (3.48), we find the effective bandwidth of the unfiltered noise is

$$f_e = 358.7 \text{ Hz}. \tag{8.11}$$

With Digital Filtering

Next, we send a wireless command through the USB monitor to the capsular device which actives the digital filter. This performs a 40 cycle "lock-in" filter on the sampled data with 18 points per cycle, totaling N = 720 points per DAQ period, as discussed in Section 5.5.4. The 720 acquired data points are collapsed into a single average value and transmitted to the USB monitor once every 3 seconds. We compare 200 consecutive transmitted filtered measurements with unfiltered data, as collected in the previous section, and show the measurement result in Fig. 8.11.

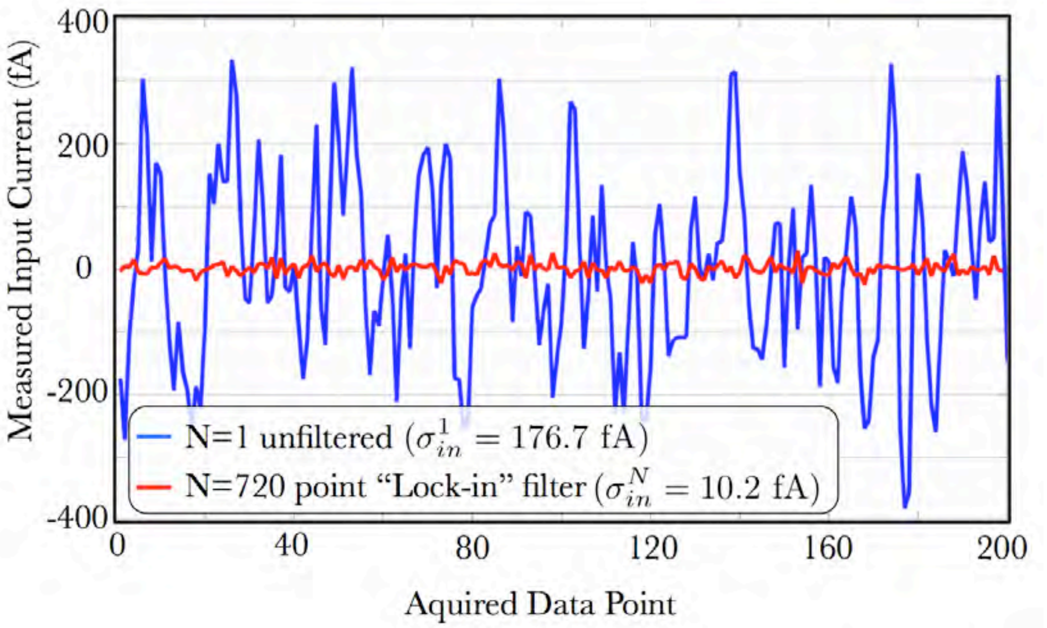

Figure 8.11: Time trace of raw data (blue) and data filtered with a N = 720 point, 40 cycle "lock-in" filter (red).

The standard deviation of the unfiltered data is measured to be

$$\sigma_{in}^{1} = 176.7 \text{ fA}, \tag{8.12}$$

and the standard deviation of the N = 720 point filter is

$$\sigma_{in}^{N} = 10.2 \text{ fA}. \tag{8.13}$$

This corresponds closely to the expected reduced noise variance due to bandwidth narrowing described in Section 3.5.2: using (3.50), we find that

$$\sigma_{in}^{N}(expected) = \sigma_{in}^{1}\sqrt{\frac{f_n/f_e}{N}} = 10.13 \text{ fA}, \tag{8.14}$$

for $f_n = f_s/2 = 850$ Hz, $f_e = 358.7$ Hz (Eq. (8.11)), and N = 720 points.

The experimental current limit of detection is then

$$I_{LOD}^{exp} = 3\,\sigma_{in}^{N} = 30.6 \text{ fA}. \tag{8.15}$$

We compare this with the theoretical limit of detection $I_{LOD}^{th} = 30$ fA, found in Section 5.6, and find excellent agreement. We conclude that the “lock-in” filter works as designed in Section 3.5.2.

8.4 Fluorometer Sensitivity and Blood Detection

8.4.1 Measurement Set-Up

The measurement set-up is shown in Fig. 8.12. A beaker is filled with 200 mL of de-ionized water and a small magnetic stirring rod (VWR, Inc.) submerged is at the bottom. The detector is lowered into the beaker and fixed in place with a clamp, approximately at the center of the beaker. The entire set-up is placed on a magnetic stirrer (Thermolyne, Inc.) which is rotating at 600 rpm throughout the experiment. This allows added fluorophore molecules to be rapidly mixed through the sample volume. The data acquisition set-up is shown in Fig. 8.13. Stock dilutions of fluorescein in water are prepared ranging from C = 10 μM to 1 mM. A command is sent wirelessly to the capsular device to activate both the LED, and the 40 cycle, N = 720 point “lock-in” filter. A volume V = 1 mL sample of each stock solution is sequentially added with a standard pipette to the beaker, and the transmitted data averaged by the MATLAB DAQ software for 20 consecutive periods.

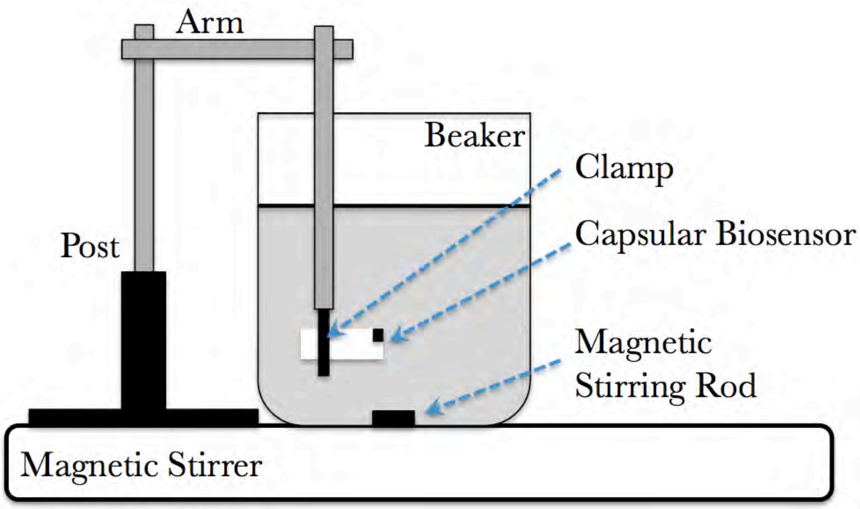

Figure 8.12: Set-up for wirelessly measuring fluorescein concentration.

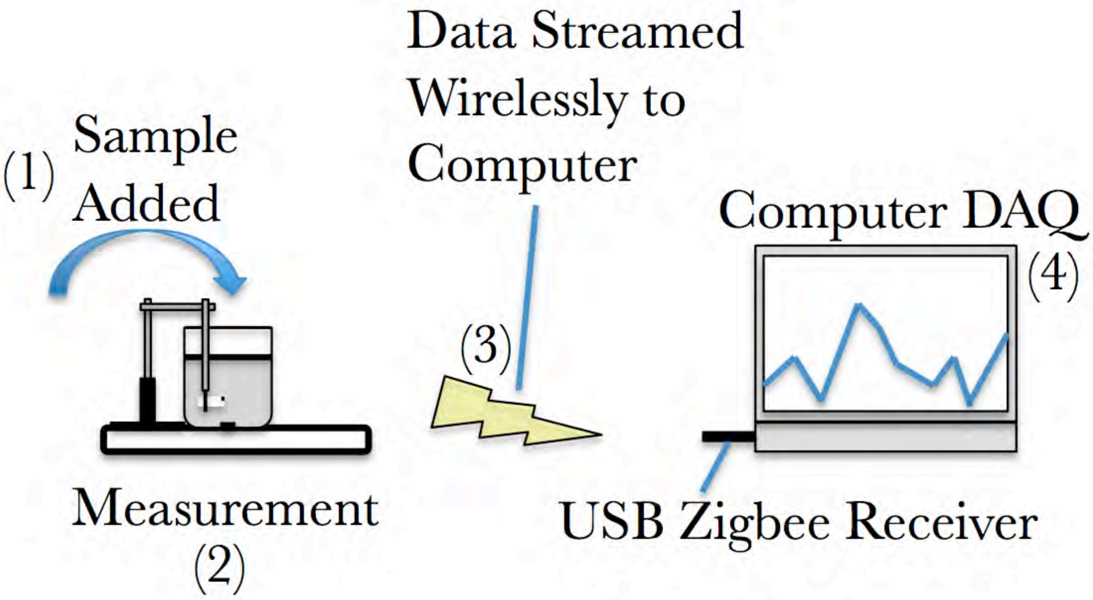

Figure 8.13: Set-up for data acquisition for concentration measurement.

8.4.2 Fluorometer Sensitivity

The collected sensitivity data is shown in Fig. 8.14. We calculate a linear fit to the data, which is the fluorometer sensitivity, and find that it is

$$I_S^{(exp)} = 1.48\,\frac{\text{fA}}{\text{nM}}. \tag{8.16}$$

We compare this value to the expected sensitivity of $I_S = 3.09$ fA/nM. Our detector is ≈ 2.1 less sensitive than predicted by our calculations in Section 8.2.2.

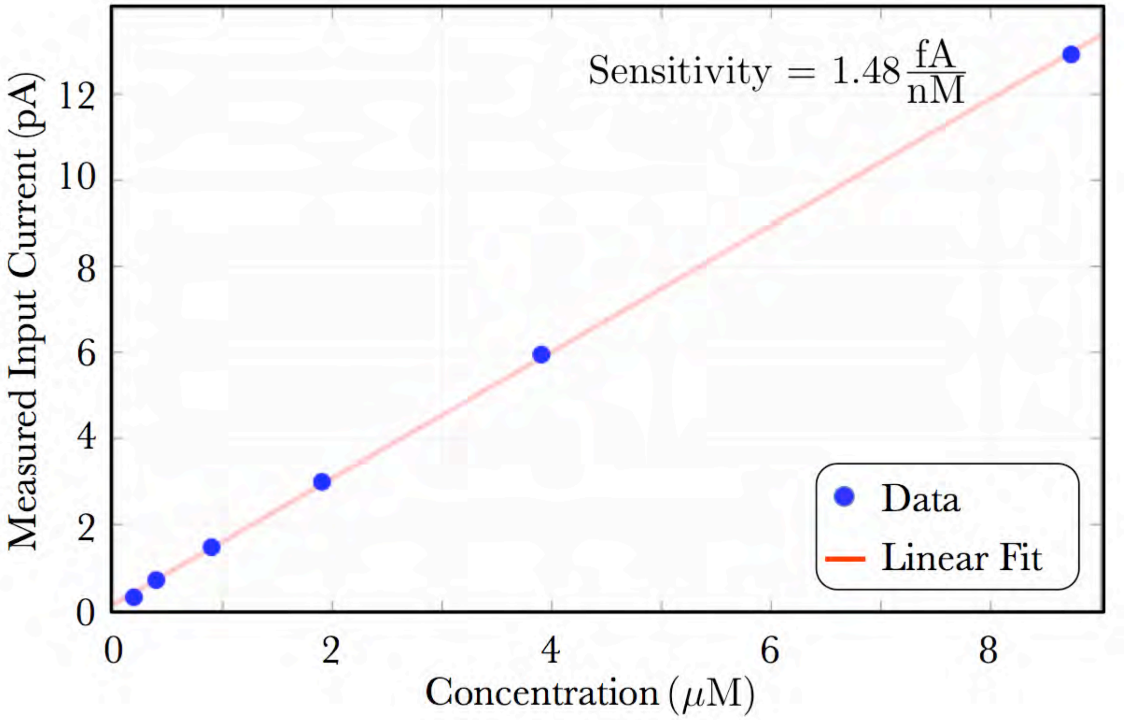

Figure 8.14: Fluorometer sensitivity.

8.4.3 Limit of Detection

We show the low concentration limit of the collected sensitivity data in Fig. 8.15 on a log-log plot. We calculate the linear slope to be $m = 0.995$ indicating that the sensor current is linear in the concentration. We also plot the show the level of input referred current noise σ_{in}^{N}, as well as $I_{LOD} = 3\,\sigma_{in}^{N}$. The concentration limit of detection is found to be

$$C_{LOD}^{exp} = 20.7 \text{ nM}, \tag{8.17}$$

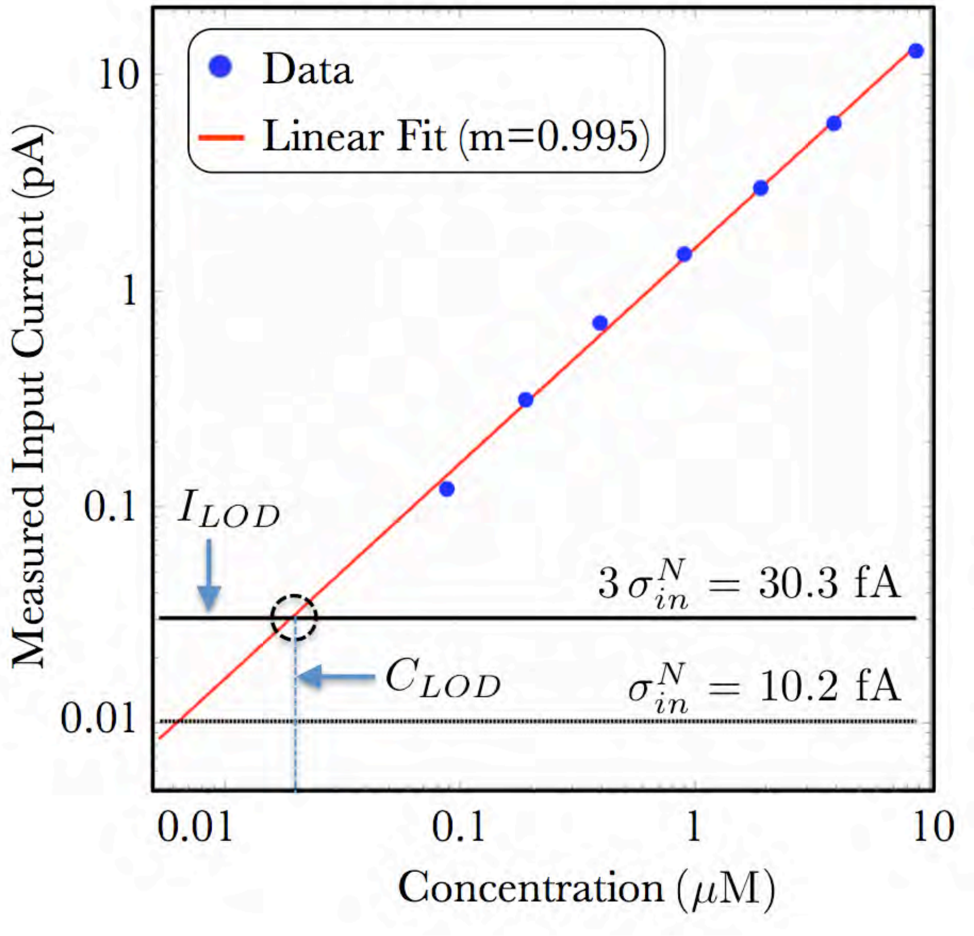

Figure 8.15: Log-log plot of sensitivity. Also shown is the input current variance, and I_{LOD}.

8.4.4 Detection of Blood

Heparinized pig's blood is procured via the Harvard Medical School through Farm to Pharm LLC. Intravenous fluorescein is simulated by adding a volume 0.107 mL of 1 mM fluorescein to 6.13 mL of blood, to give a simulated blood fluorescein concentration of $C_{iv} = 17.15\ \mu$M. This is the expected concentration in the blood 5.78 hours after intravenous injection (Eq. (2.1)), and is 1.78 hours longer than our specified T^0_{LOD}.

We follow the same experimental procedure as the pictured in Fig. 8.13, beginning with a beaker filled with V = 100 mL of deionized water. At time $t = 0$, we introduce 1 mL of the blood/fluorescein mixture into the beaker, leading to a 1% dilution, with concentration $C = 170$ nM. This corresponds to the same dilution that would be experienced by 10 mL of blood in 1 L of stomach contents.

A time trace of the measurement is shown in Fig. 8.16

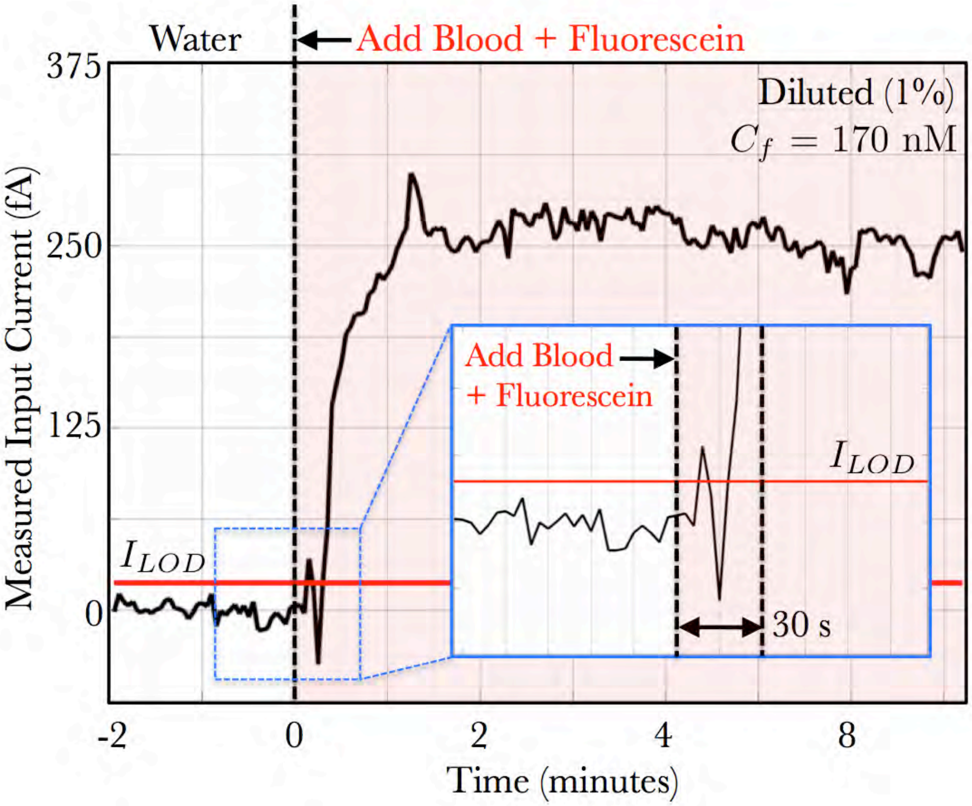

Figure 8.16: Time trace of adding blood/fluorescein mixture

The concentration of blood/fluorescein mixture in the beaker reaches equilibrium after $\approx$ 2 minutes. The measured average current after equilibrium is 252.1 fA, and using the fluorometer sensitivity of 1.48 fA/nM, this corresponds to a measured concentration 170.3 nM, which is in agreement with the added concentration of fluorescein. If the detection threshold is set at $I_{LOD} = 30.6$ fA, the detection would be triggered 3 measurement periods (9 seconds) after blood is injected as seen in Fig. 8.16(inset). This shows a successful detection of blood with fluorescein tracer, in water, simulating 10 mL of blood introduced instantaneously into the stomach with 1 L of contents, at a time t= 5.78 hours after intravenous injection.

8.5 Discussion and Conclusion

In this chapter we have characterized the performance of the detection optics, measured the electronic noise of the fluorometer, and characterized the sensitivity of the fluorometer. We have found that the measured electronic input referred current noise variance $\sigma_{in}^{N}(exp) = 10.2$ fA is in good agreement with the predicted $\sigma_{in}^{N}(th) =$ 10 fA.

Using the theoretical calculations in Section 5.4.4, and correcting for the measured transmission properties of the miniature cut filters, we predicted a fluorometer sensitivity $I_S = 3.09$ fA/nM, and we measured it to be $I_S = 1.48$ fA/nM, a factor of 2.1 difference. We believe this is because we used different fluorometer's in this chapter, one to characterize the optics, and another to detect fluorescein. At the time of fabrication of the latter fluorometer, we observed a small amount of epoxy leaking into the pinholes, potentially distorting the optical signal.

Finally, we have found a concentration limit of detection $C_{LOD} = 20.7$ nM, which is ~ 20 times better than the target $C_{LOD}^{0} = 410$ nM from our device specification. This corresponds to a concentration of fluorescein that is equivalent to to the concentration that would be reached in the stomach if 10 mL of blood were introduced into 1 L of stomach contents after a time $t = 10$ hours. Using the measured data, we project that the device time limit of detection in the stomach should be

$$t_{LOD} = 10 \text{ hours} \tag{8.18}$$

Chapter 9

Conclusion

9.1 Thesis Summary

In this thesis, have discussed how to a use a fluorescent tracer dye as an indicator for GI bleeding, and outlined the design parameters and background theory for the construction of an appropriate miniature fluorometer (Chapter 2). Next, we presented the background theory for the detection electronics and signal processing necessary to detect low level optical signals, and hence, low concentrations of dye (Chapter 3). We completed the device background with a discussion of the requirements of a lab-in-a-pill hardware platform, including software, power requirements, and wireless connectivity performance in the human body (Chapter 4). Next, we delineated the exact design of a miniature fluorophotometer to detect GI bleeding, based on the background presented in Chapters 1 - 2 (Chapter 5), and then designed the entire lab-in-a-pill hardware platform and packaging (Chapter 6). Finally, we detailed the construction of the device (Chapter 7), and evaluated its sensitivity to detecting blood with a tracer dye (Chapter 8).

9.2 Comparison with Initial Specification

Specification Type	Initial Specification	Constructed Device
Fluorescent Tracer	FDA approved	Fluorescein, FDA approved
Concentration LOD (C_{LOD})	410 nM Fluorescein	20 nM Fluorescein
Time LOD (T_{LOD})	$\geq$ 4 hours	10 hours
Wireless Communication	Transmit through body	Zigbee, used for BSN
Battery Life	$\geq$ 4 hours	2.3 days
Size	11 mm × 27 mm	11 mm × 27 mm
Cost	As low as possible	Single device parts: $110

Table 9.1: Comparison with initial specification

9.3 Future Outlook

We have demonstrated a proof-of-concept device for the detection of blood with a fluorescent tracer. Future work includes the following:

- Test the devices *in vivo* in a porcine upper gastrointestinal bleed model. We have tested prior devices based on the same Zigbee platform for RF signal quality, when implanted in live pigs and found the wireless link to work sufficiently well. The capsular biosensor presented in this thesis, however have not been evaluated yet in this context. Future work includes evaluating the detection of real bleeding in a porcine model, and optimizing radio frequency performance.

- Reformat the fluorometer optics for operation in stomach acid (pH ~ 1). Stomach acid tends to alter the fluorescence properties of fluorescein [53]. However, we believe that a shift in the excitation wavelength will sufficiently compensate for this change.

- Coat the device capsule in a biocompatible material. We have found that the Delrin plastic used in this thesis, is corroded after exposure to stomach acid for a period $\sim$ 2 - 3 days. We propose coating the device with Parylene-C [54] to provide biocompatibility.

- Construct the device is mass quantities. We believe this can drive down the cost of the device to $\sim$ \$10 / device.

- Further miniaturization. The long term goal of this project has been to create a GI bleeding detector that can be inserted endoscopically into a patient through the working channel of an endoscope, which has a 2.8 mm diameter [55]. This entails significant further development as it requires a factor of $\sim$ 4 reduction in diameter. The device presented in this thesis serves a first step towards an endoscopically implantable wireless sensor, and we believe it possible to stay within the capability of currently available off-the-shelf components to design such a device.

Bibliography

[1] M E van Leerdam, E M Vreeburg, E A Rauws, A A Geraedts, J G Tijssen, J B Reitsma, and G N Tytgat. Acute upper gi bleeding: did anything change? time trend analysis of incidence and outcome of acute upper gi bleeding between 1993/1994 and 2000. *Am J Gastroenterol*, 98(7):1494–1499, Jul 2003.

[2] F Fein, A Weber, S Koch, N Festou, A C Dupont-Gossard, J P Cervoni, E Monnet, M Bardou, and F Carbonnel. The prognosis of patients having received optimal therapy for nonvariceal upper gastrointestinal bleeding might be worse in daily practice than in randomized clinical trials. *Eur J Gastroenterol Hepatol*, 22(3):361–367, Mar 2010.

[3] D A Gilbert, F E Silverstein, and F J Tedesco. National asge survey on upper gastrointestinal bleeding: complications of endoscopy. *Dig Dis Sci*, 26(7 Suppl):–59, Jul 1981.

[4] R T Yavorski, R K Wong, C Maydonovitch, L S Battin, A Furnia, and D E Amundson. Analysis of 3,294 cases of upper gastrointestinal bleeding in military medical facilities. *Am J Gastroenterol*, 90(4):568–573, Apr 1995.

[5] M E van Leerdam. Epidemiology of acute upper gastrointestinal bleeding. *Best Pract Res Clin Gastroenterol*, 22(2):209–224, 2008.

[6] I M Gralnek, A N Barkun, and M Bardou. Management of acute bleeding from a peptic ulcer. *N Engl J Med*, 359(9):928–937, Aug 2008.

[7] S A Hearnshaw, R F Logan, D Lowe, S P Travis, M F Murphy, and K R Palmer. Use of endoscopy for management of acute upper gastrointestinal bleeding in the uk: results of a nationwide audit. *Gut*, 59(8):1022–1029, Aug 2010.

[8] N J Liu, C S Lee, J H Tang, H T Cheng, Y Y Chu, K F Sung, C H Lin, Y K Tsou, J M Lien, P C Chen, C T Chiu, and C L Cheng. Outcomes of bleeding peptic ulcers: a prospective study. *J Gastroenterol Hepatol*, 23(8 Pt 2):340–347, Aug 2008.

[9] K Bambha, W R Kim, R Pedersen, J P Bida, W K Kremers, and P S Kamath. Predictors of early re-bleeding and mortality after acute variceal haemorrhage in patients with cirrhosis. *Gut*, 57(6):814–820, Jun 2008.

[10] P W Chiu, E K Ng, F K Cheung, F K Chan, W K Leung, J C Wu, V W Wong, M Y Yung, K Tsoi, J Y Lau, J J Sung, and S S Chung. Predicting mortality in patients with bleeding peptic ulcers after therapeutic endoscopy. *Clin Gastroenterol Hepatol*, 7(3):311–316, Mar 2009.

[11] S W Lee, T Y Lee, and C S Chang. Independent factors associated with recurrent bleeding in cirrhotic patients with esophageal variceal hemorrhage. *Dig Dis Sci*, 54(5):1128–1134, May 2009.

[12] T O Kovacs. Management of upper gastrointestinal bleeding. *Curr Gastroenterol Rep*, 10(6):535–542, Dec 2008.

[13] A Languasco, L Agustin, N Cazap, C Nicolas, S Marciano, M Sebastian, M Huber, H Marina, A Novillo, N Abel, F Poletta, P Fernando, M Milberg, M Matias, D Riveros, and R Dardo. Hemoglobin concentration variations over time in general medical inpatients. *J Hosp Med*, 5(5):283–288, May-Jun 2010.

[14] J DePriest. Low incidence of hemodynamic instability in patients with gastrointestinal hemorrhage. *South Med J*, 89(4):386–390, Apr 1996.

[15] F K Cheung and J Y Lau. Management of massive peptic ulcer bleeding. *Gastroenterol Clin North Am*, 38(2):231–243, Jun 2009.

[16] O Korostynska, K Arshak, E Gill, and A Arshak. Sensors journal, ieee; review paper: Materials and techniques for in vivo ph monitoring. 8(1):20–28, 2007.

[17] Guang-Zhong Yang. *Book; Body Sensor Networks*. Springer, 2006.

[18] Mehmet Yuce, Peng Ng, and Jamil Khan. Journal of medical systems; monitoring of physiological parameters from multiple patients using wireless sensor network. 32(5):433–441, 2008.

[19] US Depratment of Transportation. Hemorrhage and shock.

[20] C Hassan, A Zullo, S Winn, and S Morini. Endoscopy; cost-effectiveness of capsule endoscopy in screening for colorectal cancer. 40(5):414–421, 2008.

[21] Christopher Laing, Terrence Tobias, David Rosenblum, Wade Banker, Lee Tseng, and Stephen Tamarkin. Radiographics; acute gastrointestinal bleeding: Emerging role of multidetector ct angiography and review of current imaging techniques. 27(4):1055–1070, 2007.

[22] S. Schostek. Device for hemmorrhage detection. Patent.

[23] M Prinz, A Carracedo, WR Mayr, N Morling, TJ Parsons, A Sajantila, R Scheithauer, H Schmitter, and PM and Schneider. Forensic science international. genetics; dna commission of the international society for forensic genetics (isfg): recommendations regarding the role of forensic genetics for disaster victim identification (dvi). 1(1):3–12, 2007.

[24] Ieee transactions on mobile computing; tree-based data broadcast in ieee 802.15.4 and zigbee networks. 5(11):1561–1574, 2006.

[25] M Camilleri, L J Colemont, S F Phillips, M L Brown, G M Thomforde, N Chapman, and A R Zinsmeister. Human gastric emptying and colonic filling of solids characterized by a new method. *Am J Physiol*, 257(2 Pt 1):284–290, Aug 1989.

[26] D Grotte, V Mattox, and R Brubaker. Fluorescent, physiological and pharmacokinetic properties of fluorescein glucuronide. *Exp Eye Res*, 40(1):23–33, Jan 1985.

[27] L E Tan, W Orilla, P M Hughes, S Tsai, J A Burke, and C G Wilson. Effects of vitreous liquefaction on the intravitreal distribution of sodium fluorescein, fluorescein dextran, and fluorescent microparticles. *Invest Ophthalmol Vis Sci*, 52(2):1111–1118, Feb 2011.

[28] L Novak, P Neuzil, J Pipper, Y Zhang, and S Lee. An integrated fluorescence detection system for lab-on-a-chip applications. *Lab Chip*, 7(1):27–29, Jan 2007.

[29] T Erdogan. Optical filters for wavelength selection in fluorescence instrumentation. *Curr Protoc Cytom*, Chapter 2, Apr 2011.

[30] X Baillard, A Gauguet, S Bize, P Lemonde, P Laurent, A Clairon, and P Rosenbusch. Optics communications; interference-filter-stabilized external-cavity diode lasers. 266(2):609–613, 2006.

[31] M Born and E Wolf. *Principles of Optics*. CambridgeUniversity Press, 1998, 1998.

[32] Jerald G. Graeme. *Photodiode Amplifiers: Op Amp Solutions*. Jan 1996.

[33] Charles Kittel. *Introduction to Solid State Physics*. John Wiley and Sons, 8th edition edition, 2005.

[34] Paul Horowitz and Winfield Hill. *The Art of Electronics*. Jan 2001.

[35] Advanced Photonix, Inc. *Datasheet: Photodiode (PDB-C122)*.

[36] John H. Moore, Christopher C. Davis, Michael A. Coplan, and Sandra C Greer. *Building scientific apparatus*. Cambridge University Press, Cambridge, UK, 4th ed edition, 2009.

[37] Shlomo Engelberg. *Random Signals and Noise: A Mathematical Introduction*. Jan 2007.

[38] H Nyquist. Thermal agitation of electric charge in conductors. *Phys Rev*, 32(1):110–113, Jan 1928.

[39] Alan V. Oppenheim, Ronald W. Schafer, and John R Buck. *Discrete-Time Signal Processing*. Prentice Hall, Upper Saddle River, N.J., 2nd ed edition, 1999.

[40] Tia Gao, Tammara Massey, Leo Selavo, David Crawford, Bor-rong Chen, Konrad Lorincz, Victor Shnayder, and Matt Welsh. Ieee transactions on biomedical circuits and systems; the advanced health and disaster aid network: A light-weight wireless medical system for triage. 2007.

[41] Matt Welsch. Harvard code blue project.

[42] P Valdastri. Transmission power requirements for novel zigbee implants in the gastrointestinal tract. *IEEE Transactions in Biomedical Engineering*, 55(6):1705, June 2008.

[43] Robert Collin. *Foundations for Microwave Engineering*. Wiley-IEEE Press, 2 edition, 2000.

[44] Ember, Inc. *Datasheet: Ember SoC (EM250)*.

[45] T Desmettre, J M Devoisselle, and S Mordon. Fluorescence properties and metabolic features of indocyanine green (icg) as related to angiography. *Surv Ophthalmol*, 45(1):15–27, Jul-Aug 2000.

[46] F Reyes, M Noelck, C Valentino, L Grasso-Lebeau, and J Lang. Complications of methylene blue dye in breast surgery: case reports and review of the literature. *J Cancer*, 2:20–25, 2010.

[47] Suzanne Fery-Forgues and Dominique Lavabre. Journal of chemical education; are fluorescence quantum yields so tricky to measure? a demonstration using familiar stationery products. 76(9):1260, 1999.

[48] William Ganong. *Review of Medical Physiology (LANGE Basic Science)*. McGraw-Hill Medical, 2003.

[49] P Valdastri, C Quaglia, E Susilo, A Menciassi, P Dario, CN Ho, G Anhoeck, and MO Schurr. Endoscopy; wireless therapeutic endoscopic capsule: in vivo experiment. 40(12):979–982, 2008.

[50] JM Tarascon and M Armand. Nature; issues and challenges facing rechargeable lithium batteries. 414(6861):359–367, 2001.

[51] Robert Collin. *Foundations for Microwave Engineering.* Wiley-IEEE Press, 2 edition, 2000.

[52] Reltek, Inc. *Datasheet: BONDiT.*

[53] Harvery Diehl and Richard Markuszewski. Studies on fluorescein - vii: The fluoresence of fluorescein as a function of ph. *Talanta*, 36(3):416–418, 1989.

[54] Tan and Craighead. Materials; surface engineering and patterning using parylene for biological applications. 3(3):1803–1832, 2010.

[55] Olympus. Gi type h180j endoscope.

Appendix A

Device Bill of Materials

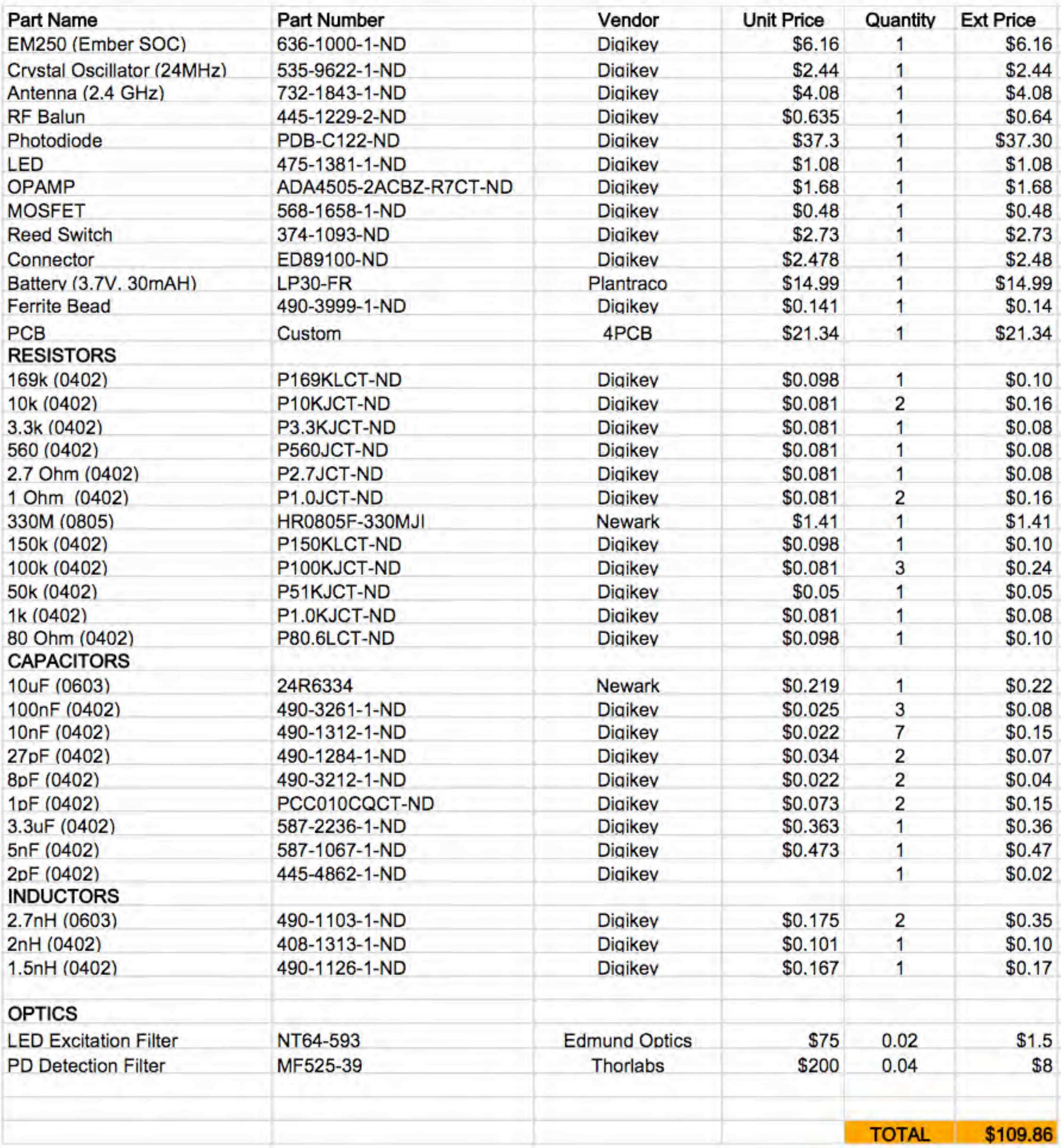

Part Name	Part Number	Vendor	Unit Price	Quantity	Ext Price
EM250 (Ember SOC)	636-1000-1-ND	Digikey	$6.16	1	$6.16
Crystal Oscillator (24MHz)	535-9622-1-ND	Digikey	$2.44	1	$2.44
Antenna (2.4 GHz)	732-1843-1-ND	Digikey	$4.08	1	$4.08
RF Balun	445-1229-2-ND	Digikey	$0.635	1	$0.64
Photodiode	PDB-C122-ND	Digikey	$37.3	1	$37.30
LED	475-1381-1-ND	Digikey	$1.08	1	$1.08
OPAMP	ADA4505-2ACBZ-R7CT-ND	Digikey	$1.68	1	$1.68
MOSFET	568-1658-1-ND	Digikey	$0.48	1	$0.48
Reed Switch	374-1093-ND	Digikey	$2.73	1	$2.73
Connector	ED89100-ND	Digikey	$2.478	1	$2.48
Battery (3.7V, 30mAH)	LP30-FR	Plantraco	$14.99	1	$14.99
Ferrite Bead	490-3999-1-ND	Digikey	$0.141	1	$0.14
PCB	Custom	4PCB	$21.34	1	$21.34
RESISTORS					
169k (0402)	P169KLCT-ND	Digikey	$0.098	1	$0.10
10k (0402)	P10KJCT-ND	Digikey	$0.081	2	$0.16
3.3k (0402)	P3.3KJCT-ND	Digikey	$0.081	1	$0.08
560 (0402)	P560JCT-ND	Digikey	$0.081	1	$0.08
2.7 Ohm (0402)	P2.7JCT-ND	Digikey	$0.081	1	$0.08
1 Ohm (0402)	P1.0JCT-ND	Digikey	$0.081	2	$0.16
330M (0805)	HR0805F-330MJI	Newark	$1.41	1	$1.41
150k (0402)	P150KLCT-ND	Digikey	$0.098	1	$0.10
100k (0402)	P100KJCT-ND	Digikey	$0.081	3	$0.24
50k (0402)	P51KJCT-ND	Digikey	$0.05	1	$0.05
1k (0402)	P1.0KJCT-ND	Digikey	$0.081	1	$0.08
80 Ohm (0402)	P80.6LCT-ND	Digikey	$0.098	1	$0.10
CAPACITORS					
10uF (0603)	24R6334	Newark	$0.219	1	$0.22
100nF (0402)	490-3261-1-ND	Digikey	$0.025	3	$0.08
10nF (0402)	490-1312-1-ND	Digikey	$0.022	7	$0.15
27pF (0402)	490-1284-1-ND	Digikey	$0.034	2	$0.07
8pF (0402)	490-3212-1-ND	Digikey	$0.022	2	$0.04
1pF (0402)	PCC010CQCT-ND	Digikey	$0.073	2	$0.15
3.3uF (0402)	587-2236-1-ND	Digikey	$0.363	1	$0.36
5nF (0402)	587-1067-1-ND	Digikey	$0.473	1	$0.47
2pF (0402)	445-4862-1-ND	Digikey		1	$0.02
INDUCTORS					
2.7nH (0603)	490-1103-1-ND	Digikey	$0.175	2	$0.35
2nH (0402)	408-1313-1-ND	Digikey	$0.101	1	$0.10
1.5nH (0402)	490-1126-1-ND	Digikey	$0.167	1	$0.17
OPTICS					
LED Excitation Filter	NT64-593	Edmund Optics	$75	0.02	$1.5
PD Detection Filter	MF525-39	Thorlabs	$200	0.04	$8
				TOTAL	**$109.86**

Figure A.1: Bill of Materials